

# **The Evolutionary Impact of Supermassive Black Holes on their Host Galaxies**



**MACQUARIE**  
University  
SYDNEY • AUSTRALIA

**Michael James Cowley**

Department of Physics and Astronomy  
Macquarie University

This dissertation is submitted for the degree of  
*Doctor of Philosophy*

April 2018



This work is dedicated to the memory of Anna Cowley.





## Declaration

I hereby declare that, except where specific reference is made to the work of others, the contents of this dissertation are original and have not been submitted in whole or in part for consideration for any other degree or qualification in this, or any other University. This dissertation is the result of my own work and includes nothing which is the outcome of work done in collaboration, except where specifically indicated in the text. Portions of the work presented here have been, or are due to be, published in the following papers:

Cowley, M. J., Spitler, L. R., Tran, K-V. H., et al., 2016, “**ZFOURGE catalogue of AGN candidates: an enhancement of 160  $\mu\text{m}$ -derived star formation rates in active galaxies to  $z = 3.2$** ”, MNRAS, 457, 629–41

Cowley, M. J., Spitler, L. R., Quadri, R. F., et al., 2017, “**Decoupled black hole accretion and quenching: the relationship between BHAR, SFR, and quenching in Milky Way and Andromeda-mass progenitors since  $z = 2.5$** ”, MNRAS, 473, 3710-3716

Cowley, M. J., Spitler, L. R., Mullaney, J. R., et al., 2017, “**A Two Band Approach to Isolate the AGN Contribution to Observed SEDs**”, In Preparation

In addition to the above, I have also contributed to the following papers during the period of my candidature:

Cowley, M. J. and Hughes. S. W., 2017, “**Modelling the dynamics of a hypothetical Planet X by way of gravitational N-body simulator**”, Eur. J. Phys, 38, 025602

Alcorn, L. Y., Tran, K-V. H., Glazebrook, K., et al., 2017, “**ZFIRE: 3D modeling of rotation, dispersion, and angular momentum of star-Forming galaxies at  $z \sim 2$** ”, ApJ, submitted

da Cunha, E., Hopkins, A. M., Colless, M., et al., 2017, “**The Taipan Galaxy Survey: Scientific Goals and Observing Strategy**”, PASA, 34, 47

Forrest, B., Tran, K-V. H., Broussard, A., et al., 2017, “**Discovery of extreme [OIII]+H $\beta$  emitting galaxies tracing an overdensity at  $z \sim 3.5$  in CDF-South**”, ApJL, 838, L12

Nanayakkara, T., Glazebrook, K., Kacprzak, G. G., et al., 2017 “**ZFIRE: Using H $\alpha$  equivalent widths to investigate the In Situ initial mass function at  $z \sim 2$** ”, MNRAS, 468, 3071-3108

Straatman, C. M. S., et al., Glazebrook, K., Kacprzak, G. G., et al., 2017 “**ZFIRE: The evolution of the stellar mass Tully-Fisher relation to redshift  $2.0 < z < 2.5$  with MOS-FIRE**”, ApJ, 839, 57

Hughes. S. W. and Cowley, M. J., 2017, “**Teaching the Doppler effect in astrophysics**”, Eur. J. Phys, 38, 025603

Allen, R. J., Kacprzak, G. G., Glazebrook, K., et al., 2017, “**The size evolution of star-forming galaxies since  $z \sim 7$  using ZFOURGE**”, ApJL, 834, L11

Tran, K-V. H., Alcorn, L. Y., Kacprzak, G. G., et al., 2017, “**ZFIRE: similar stellar growth in H $\alpha$ -emitting cluster and field galaxies at  $z \sim 2$** ”, ApJ, 834, 101

Straatman, C. M. S., Spitler, L. R., Quadri, R. F., et al., 2016, “**The Fourstar Galaxy Evolution Survey (ZFOURGE): ultraviolet to far-infrared catalogs, medium-bandwidth photometric redshifts with improved accuracy, stellar masses, and confirmation of quiescent galaxies to  $z \sim 3.5$** ”, ApJ, 830, 51

Nanayakkara, T., Glazebrook, K., Kacprzak, G. G., et al., 2016, “**ZFIRE: a Keck / MOS-FIRE spectroscopic survey of galaxies in rich environments at  $z \sim 2$** ”, ApJ, 828, 21

Hung, C-L., Casey, C. M., Chiang, Y-K., et al., 2016, “**Large-scale structure around a  $z = 2.1$  cluster**”, ApJ, 826, 130

Kacprzak, G. G., van de Voort, F., Glazebrook, K., et al., 2016, “**Cold-mode accretion: driving the fundamental mass-metallicity relation at  $z \sim 2$** ”, ApJ, 826, L11

- 
- Allen, R. J., Kacprzak, G. G., Glazebrook, K., et al., 2016, “**Differences in the structural properties and star-formation rates of field and cluster galaxies at  $z \sim 1$** ”, ApJ, 826, 60
- Alcorn, L. Y., Tran, K-V. H., Kacprzak, G. G., et al., 2016, “**ZFIRE: the kinematics of star-forming galaxies as a function of environment at  $z \sim 2$** ”, ApJL, 825, L2
- Kewley, L.J., Yuan, T., Nanayakkara, T., Kacprzak G G, et al., 2016, “**Z-FIRE: ISM properties of the  $z = 2.095$  COSMOS cluster**”, ApJ, 819, 100
- Forrest, B., Tran, K-V. H., Tomczak, A. R., et al., 2016, “**UV to IR luminosities and dust attenuation determined from  $\sim 4000$  K-selected galaxies at  $1 < z < 3$  in the ZFOURGE survey**”, ApJ, 818, L26
- Tomczak, A. R., Quadri, R. F., Tran, K-V. H., et al., 2016, “**The SFR- $M^*$  relation and empirical star-formation histories from ZFOURGE at  $0.5 < z < 4$** ”, ApJ, 817, 118
- Rees, G. A., Spitler, L. R., Norris, R. P., Cowley, M. J., et al., 2016, “**Radio galaxies in ZFOURGE/NMBS: no difference in the properties of massive galaxies with and without radio-AGN out to  $z = 2.25$** ”, MNRAS, 455, 2731–44
- Hughes, S. W., Cowley, M. J., Powell, S., and Carroll, J., 2016, “**The atmospheric extinction of light**” Eur. J. Phys., 37, 015601
- Kawinwanichakij. L., Quadri, R. F., Papovich, C., et al., 2016, “**Satellite quenching and galactic conformity at  $0.3 < z < 2.5$** ”, ApJ, 817, 9
- Hughes, S. W., Powell, S., Carroll, J., and Cowley, M., 2015, “**Parallax in the park**”, Eur. J. Phys., 36, 065030
- Straatman, C. M. S., Labbé, I., Spitler, L. R., Glazebrook K, Tomczak A, Allen R, Brammer G B, Cowley M, Dokkum P V, Kacprzak G G, Kawinwanichakij L, Mehrrens N, Nanayakkara T, Papovich C, Persson et al., 2015, “**The sizes of massive quiescent and star-forming galaxies at  $z \sim 4$  with ZFOURGE and CANDELS**”, ApJL, 808, L29

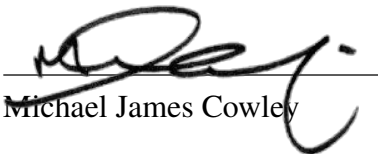
Allen, R. J., Kacprzak, G. G., Spitler, L. R., et al., 2015, “**The differential size growth of field and cluster galaxies at  $z = 2.1$  using the ZFOURGE survey**”, ApJ, 806, 3

Papovich, C., Labbé, I., Quadri, R., et al., 2015, “**ZFOURGE/CANDELS: on the evolution of  $M^*$  galaxy progenitors from  $z = 3$  to 0.5**”, ApJ, 803, 26

Kacprzak, G. G., Yuan, T., Nanayakkara, T., et al., 2015, “**The absence of an environmental dependence in the mass–metallicity relation at  $z = 2$** ”, ApJL, 802, L26

Kawinwanichakij, L., Papovich, C., Quadri, R. F., et al., 2014, “**The distribution of satellites around massive galaxies at  $1 < z < 3$  in ZFOURGE/CANDELS: dependence on star formation activity**”, ApJ, 792, 103

Cowley, M. J., and Hughes, S. W., 2014, “**Characterization of transiting exoplanets by way of differential photometry**”, Phys. Educ., 49, 293–8



---

Michael James Cowley

## Acknowledgements

First, I thank Lee Spitler, my supervisor, for encouragement, support and the many opportunities, which inspired me to become a better student and researcher. Lee's supervising style was my perfect match, granting me the ability to explore my ideas while having access to his wealth of knowledge and expertise to guide me in the right direction. I extend the same thanks to my co-supervisors, Richard McDermid and Andrew Hopkins.

I would also like to thank my collaborators on the ZFOURGE, ZFIRE, and TAIPAN surveys. This includes, but is not limited to, Kim-Vy Tran, Ryan Quadri, Adam Tomczak, Ivo Labbe, Karl Glazebrook, Glenn Kacprzak, Caroline Straatman, Casey Papovich, Lisa Kewley, Tiantian Yuan, and Pieter van Dokkum. I also extend my thanks to Leo, Rebecca, Ben, Themiya, Glen, and Dilyar, the students of these groups. Their assistance contributed not only to work presented here but also a wealth of other research I had the privilege to participate in over the past few years.

Acknowledgement is also due to Macquarie University and the Australian Astronomical Observatory. The scholarships and funding they provided enabled this research and the many opportunities for me to collaborate with world-class researchers both domestically and internationally. While it is not possible to name them all here, I am also grateful for the unending knowledge, advice, and guidance of the individuals within these research groups. A special acknowledgement is also extended to these institution's supportive administrative teams.

Finally, I am grateful to my family, whose unconditional love, patience, and continual support of my academic endeavours enabled me to complete this work. To my wife, Cherrie, for her unbelievable patience. To her parents, Ron and Katie, for their enthusiasm. To my father and sister, Peter and Bridget, for their encouragement. To my mother, Anna, for everything.



## Abstract

By exploiting the ultra-deep,  $K_s$ -band imaging of the FourStar Galaxy Evolution Survey (ZFOURGE), we investigate the evolutionary impact of supermassive black holes (SMBHs) on their host galaxies. We advance this line of research by applying new analyses to a more substantial number of sources, with higher quality photometric redshifts, over a broader redshift range, and down to deeper mass-limits than most studies before it. We begin by supplementing the ZFOURGE galaxy catalogues with data in radio, X-ray, and infrared wavebands to catalogue AGN host galaxies across a broad redshift range of  $z = 0.2 - 3.2$ . We then use these catalogues to construct a mass-complete ( $\log(M_*/M_\odot) \geq 9.75$ ), luminosity limited sample of AGN to compare their rest-frame  $U - V$  versus  $V - J$  ( $UVJ$ ) colours and specific star formation rates (sSFRs) to a mass-matched control sample of inactive (non-AGN) galaxies. Our  $UVJ$  diagnostics reveal that the AGN tend to be hosted in a lower fraction of quiescent galaxies and a higher fraction of dusty galaxies than the control sample. Using 160  $\mu\text{m}$  *Herschel* PACS data, we find the mean sSFRs of AGN hosts to be elevated by  $0.34 \pm 0.07$  dex with respect to the control sample across all redshifts. This offset is primarily driven by infrared-selected AGN, where the mean sSFR is found to be elevated by as much as a factor of  $\sim 5$ . The remaining population, comprised predominantly of X-ray AGN hosts, is found mostly consistent with inactive galaxies, exhibiting only a marginal elevation. To probe the elevated star formation (SF) found in our AGN samples, we turn our attention to infrared-selected AGN and apply techniques to separate the AGN and SF components of each galaxy's spectral energy distribution (SED). We use this approach to estimate the black hole accretion rate (BHAR) and star formation rate (SFR) for Milky Way (MW) and Andromeda (M31)-mass progenitors from  $z = 0.2 - 2.5$ . Our motivation here is to minimise the effects of AGN contamination and selection-bias as we track the evolution of the SF-AGN connection of these sources from high to low redshift. Specifically, we track the evolution of their quenching rate via  $UVJ$  diagnostics, and their relative black hole-galaxy growth (i.e. their BHAR/SFR ratio). We find as the progenitors evolve, their BHAR/SFR ratio does not track the rate at which progenitors quench. Furthermore, the logarithm of the BHAR/SFR ratio of MW-mass progenitors evolves with a slope of  $0.64 \pm 0.11$ , while M31-mass progenitors are  $0.39 \pm 0.08$ . These results contrast with previous studies that find

an almost flat slope when adopting X-ray/AGN-selected or mass-limited samples and is likely due to their use of a broad mixture of galaxies with different evolutionary histories. Our use of progenitor-matched samples highlights the potential importance of carefully selecting progenitors when searching for evolutionary relationships between SMBHs and their host galaxies. Finally, we present a new technique to isolate the AGN contribution to the observed SED using only two photometric bands. Such an approach lends itself to studies where abundant photometric data may be lacking. While our approach is not without its limitations, we show it can reproduce underlying trends known to exist in AGN samples. Specifically, we reproduce the SF-AGN correlation found in infrared-selected AGN. However, similar to the previous chapter, we highlight where selection-bias may be driving these results. Overall, this thesis adds significant evidence to the suggestion that correlations observed between SMBHs and their host galaxies may be driven by selection effects, while also casting doubts over the idea that the suppression of star formation is predominantly driven by the negative feedback of luminous AGN over most of cosmic time.



# Table of contents

<b>List of figures</b>	<b>xvii</b>
<b>List of tables</b>	<b>xix</b>
<b>List of acronyms</b>	<b>xxiii</b>
<b>1 Introduction</b>	<b>1</b>
1.1 Overview . . . . .	1
1.2 Star Formation and the Evolution of Galaxies . . . . .	1
1.2.1 Measuring Star Formation . . . . .	2
1.3 Supermassive Black Holes . . . . .	3
1.3.1 Active Galactic Nuclei . . . . .	4
1.3.2 AGN Structure and the Unified Model . . . . .	5
1.4 The Relationship Between SMBHs and Their Hosts . . . . .	10
1.4.1 Gas Inflows & Outflows . . . . .	11
1.4.2 Correlation Between SFR and AGN Activity . . . . .	13
1.5 Observational Surveys and Facilities . . . . .	14
1.5.1 ZFOURGE . . . . .	14
1.5.2 Ancillary Sources . . . . .	15
1.6 Thesis Overview . . . . .	17
<b>2 Selecting AGN in ZFOURGE</b>	<b>19</b>
2.1 Introduction . . . . .	19
2.2 Multi-Wavelength Data . . . . .	20
2.2.1 Radio Data . . . . .	20
2.2.2 X-ray Data . . . . .	20
2.2.3 Far-Infrared Data . . . . .	22
2.3 Multi-Wavelength AGN Selection . . . . .	24
2.3.1 Host Galaxy Parameters . . . . .	24

2.3.2	Reliability of AGN Photometric Redshifts . . . . .	25
2.3.3	Radio AGN Selection . . . . .	26
2.3.4	X-ray AGN Selection . . . . .	28
2.3.5	Infrared AGN Selection . . . . .	31
2.4	Summary . . . . .	33
<b>3</b>	<b>An Enhancement of Star Formation in AGN Hosts</b>	<b>35</b>
3.1	Introduction . . . . .	35
3.2	Mass-Limited Sample . . . . .	38
3.2.1	Redshift, Mass and Luminosity Cuts . . . . .	38
3.2.2	Control Sample of Inactive Galaxies . . . . .	39
3.3	Results . . . . .	40
3.3.1	Comparison of Rest-frame Colours . . . . .	40
3.3.2	Comparison of Star Formation Activity . . . . .	42
3.3.3	AGN Contamination . . . . .	46
3.4	Discussion . . . . .	46
3.5	Summary . . . . .	49
<b>4</b>	<b>Decoupled Black Hole Accretion and Quenching</b>	<b>51</b>
4.1	Introduction . . . . .	51
4.2	Data Sets . . . . .	52
4.3	Data Analysis . . . . .	53
4.3.1	Progenitor Selection . . . . .	53
4.3.2	Black Hole Accretion Rates . . . . .	55
4.3.3	SED Decomposition of $L_{\text{IR}}$ . . . . .	55
4.3.4	$L_{\text{AGN}}$ from X-ray Stacking . . . . .	60
4.4	Results . . . . .	60
4.4.1	Evolution of Star Formation and Black Hole Accretion . . . . .	60
4.5	Discussion . . . . .	65
<b>5</b>	<b>A Two Band Approach to Isolate the AGN Contribution to Observed SEDs</b>	<b>67</b>
5.1	Introduction . . . . .	67
5.2	Data Sets and Sample Selection . . . . .	68
5.3	Methodology . . . . .	68
5.3.1	Results . . . . .	71
5.4	Discussion and Summary . . . . .	72
5.5	Summary and Future Work . . . . .	73

---

<b>6</b>	<b>Conclusions and Future Work</b>	<b>75</b>
6.1	An Enhancement of Star Formation in AGN Hosts . . . . .	75
6.2	Decoupled Black Hole Accretion and Quenching . . . . .	76
6.3	A Two Band Approach to Isolate the AGN Contribution to Observed SEDs	76
6.4	Ongoing and Future Work . . . . .	77
6.4.1	The Impact of Low-Luminosity AGN on their Hosts . . . . .	77
	<b>References</b>	<b>79</b>
	<b>Appendix A Catalogue of AGN Candidates</b>	<b>93</b>



# List of figures

1.1	Dust-obscured & unobscured star-forming galaxy SEDs . . . . .	3
1.2	Schematic of an AGN SED . . . . .	6
1.3	Unified model of an AGN . . . . .	8
1.4	Flow chart of AGN classes . . . . .	9
1.5	Cosmic SFR and BHAR accretion rate density . . . . .	11
2.1	Positional correction of radio sources in ZFOURGE-CDFS . . . . .	21
2.2	Positional correction of radio sources in ZFOURGE-COSMOS . . . . .	21
2.3	Positional correction of radio sources in ZFOURGE-UDS . . . . .	22
2.4	Positional correction of X-ray sources in ZFOURGE-CDFS . . . . .	23
2.5	Positional correction of X-ray sources in ZFOURGE-COSMOS . . . . .	23
2.6	Positional correction of X-ray sources in ZFOURGE-UDS . . . . .	24
2.7	Comparison of photometric and spectroscopic redshifts for AGN hosts . . .	27
2.8	Radio AGN selection . . . . .	29
2.9	X-ray AGN selection . . . . .	30
2.10	Infrared AGN selection . . . . .	32
2.11	AGN host galaxy properties . . . . .	34
3.1	Stellar mass vs redshift in ZFOURGE . . . . .	37
3.2	Redshift, mass, and SFR histograms for AGN hosts . . . . .	39
3.3	UVJ analysis of AGN hosts . . . . .	41
3.4	Mean sSFR vs. mass for AGN hosts . . . . .	43
3.5	mean sSFR vs redshift for AGN hosts . . . . .	44
4.1	Milky Way & Andromeda-mass progenitor selection . . . . .	54
4.2	SED decomposition in ZFOURGE . . . . .	58
4.3	SED decomposition tests . . . . .	59
4.4	BHAR & SFR evolution for progenitors . . . . .	62
4.5	Quenching rate and fraction evolution for progenitors . . . . .	64

4.6	Sersic index for progenitors . . . . .	66
5.1	Average AGN and SFG SED template . . . . .	69
5.2	Simulation of recovered 24 $\mu\text{m}$ and 160 $\mu\text{m}$ Fluxes . . . . .	70
5.3	IR SF luminosity vs IR AGN luminosity . . . . .	71
5.4	CIGALE comparisons to Two Band approach . . . . .	74

# List of tables

3.1	AGN luminosity limits . . . . .	38
3.2	Mean sSFR for AGN hosts by stellar mass . . . . .	45
3.3	Mean sSFR for AGN hosts by AGN class . . . . .	45
4.1	SED decomposition parameters . . . . .	56
5.1	Mean $L_{\text{IR,SF}}$ and SFRs for the data presented in Fig. 5.2 . . . . .	72





# List of acronyms

12MGS	12 $\mu$ m Sample of Seyfert Galaxies
ACIS	Advanced CCD Imaging Spectrometer
AGN	Active Galactic Nuclei
BH	Black Hole
BHAR	Black Hole Accretion Rate
BLR	Broad Line Region
CANDELS	Cosmic Assembly Near Infrared Deep Extragalactic Legacy Survey
CCD	Charge-Coupled Device
CDFS	Chandra Deep Field South
CDM	Cold Dark Matter
COSMOS	Cosmological Evolution Survey
EPIC	European Photon Imaging Cameras
ESA	European Space Agency
FIR	Far Infrared
FWHM	Full Width at Half Maximum
HIFI	Heterodyne Instrument for the Far Infrared
HR	Hardness Ratio
HST	Hubble Space Telescope

IMF	Initial Mass Function
IR	Infrared
IRAC	Infrared Array Camera
M31	Andromeda Galaxy
MEAM	Multi-Epoch Abundance Matching
MIPS	Multi-Band Imaging Photometer for Spitzer
MW	Milky Way Galaxy
NASA	National Aeronautics and Space Administration
NLR	Narrow Line Region
NMAD	Normalised Median Absolute Deviation
NRAO	National Radio Astronomy Observatory
PACS	Photo-detecting Array Camera and Spectrometer
PAH	Polycyclic Aromatic Hydrocarbon
RL	Radio Loud
RQ	Radio Quiet
SED	Spectral Energy Distribution
SFG	Star-Forming Galaxy
SFR	Star Formation Rate
SMBH	Super Massive Black Hole
SPIRE	Spectral and Photometric Imaging Receiver
sSFR	Specific Star Formation Rate
UDS	Ultra Deep Survey
ULIRG	Ultra Luminous Infrared Galaxy
UV	Ultraviolet

VLA            Very Large Array

XMM-Newton X-ray Multi-Mirror Mission

ZFOURGE    Four Star Galaxy Evolution Survey



# Chapter 1

## Introduction

### 1.1 Overview

Located in the centres of most massive galaxies, supermassive black holes (SMBHs) are objects of extreme density up to billions of times more massive than our Sun. When matter falls into these monster black holes, vast amounts of energy is released, evidence of which is sometimes observed on scales far beyond the galaxy itself. It has long been suspected that this energy may be responsible for stopping galaxies from forming new stars, by heating or driving out the supply of star-forming gas – a process typically termed “negative feedback”. While the inclusion of a negative feedback mechanism in galaxy simulations helps regulate star formation to reproduce the properties of galaxies in the local Universe, recent studies have pointed to an opposing possibility, one where the energy flow from the SMBH can compress gas and trigger enhanced star formation – i.e. “positive feedback”. The opposing view of these processes highlights our poor understanding of how energetic outflows from SMBHs impact the star formation of galaxies through cosmic time. While this thesis does not provide a definitive answer to these issues, it attempts to improve our understanding of it by making use of new observational data and analytical techniques that span a significant portion of the history of the Universe. In this Chapter, we provide a brief overview of star formation and galaxy evolution, the growth of SMBHs, and the connection between these two processes.

### 1.2 Star Formation and the Evolution of Galaxies

A key driver of galaxy evolution is star formation, which relies on the cooling of gas in dark matter halos. As this gas cools and flows inwards, its self-gravity eventually dominates over

the gravity of the dark matter allowing it to collapse into small, high-density cores that may form stellar embryos. Cold molecular gas is the critical component here, and its availability is dictated by several processes. For example, accretion from filaments and the merging of gas-rich clouds both serve to enhance the availability of gas (Barnes & Hernquist, 1991; Conselice et al., 2013). However, supernovae explosions, energetic outflows from SMBHs, and star formation itself can expel or heat the gas, which hinders the process (Larson, 1974; Silk & Rees, 1998; Dekel & Silk, 1986). To understand the evolution of galaxies, it is critical to monitor the rates of star formation in a diverse sample of galaxies through cosmic time.

### 1.2.1 Measuring Star Formation

The process of measuring star formation is typically a two-pronged approach, with different indicators allowing for the contributions from both unobscured and obscured stellar light. While there are several multi-wavelength indicators, (see Kennicutt & Evans, 2012) this thesis adopts two for the purpose of measuring a star formation rate (SFR). The first is via ultraviolet (UV) measurements, longward of the Lyman-continuum break. Here, the UV directly traces the photospheric emission of young stars, which makes it one of the most direct tracers of the recent SFR (time-scales of 0-100 Myr; Kennicutt & Evans, 2012). The second indicator makes use of infrared (IR) emission, which is emitted by interstellar dust that has absorbed stellar light. Unlike the UV indicator, which is a direct measure of stellar light, the IR indicator probes stellar light reprocessed by dust and is a time-averaged measurement (time-scales of 10-100 Myr; Kennicutt & Evans, 2012) of star formation. Studies have shown that with increasing redshift, the IR luminosity density of galaxies greatly exceeds the UV luminosity density (approximately an order of magnitude larger at redshifts  $z \sim 1.2$ ; Burgarella et al., 2013). Given that the focus of this thesis is the evolution of galaxies and SMBHs from high-redshift, IR measurements represent a critical component of this study. In Figure 1.1, we illustrate two galaxy spectral energy distribution (SED) examples, an unobscured spiral galaxy (blue) and a dust-obscured starburst (red). The dust obscured starburst is characteristic of star-forming galaxies at high- $z$ . As can be seen, its SED peaks at rest-frame far-IR wavelengths, where the bulk of the emission is from the reprocessed emission of young stars. As a result, observations of this regime are critical to measuring SFRs at high- $z$ . The specifics of how we calculate an SFR, in solar masses ( $M_{\odot}$ ) per year, will be addressed in subsequent chapters.

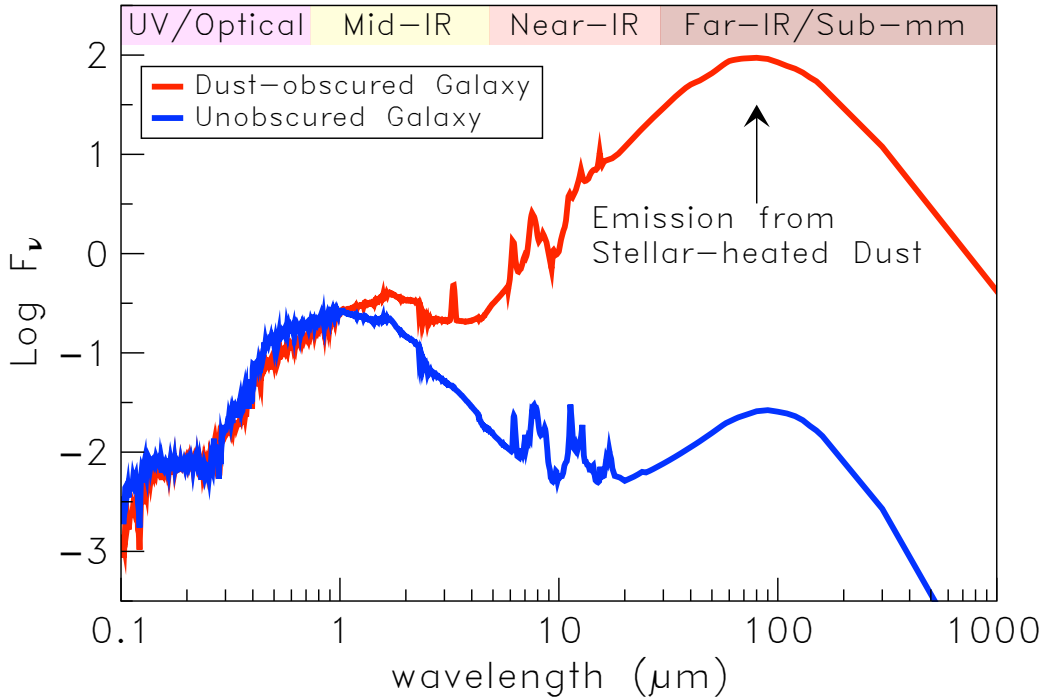


**Fig. 1.1** An example of a dust-obscured (red) and unobscured (blue) star-forming galaxy taken from the SWIRE templates (Polletta et al., 2007). For illustrative purposes, both SEDs have been normalised to 1  $\mu\text{m}$ . The apparent difference between the two is the lack of reprocessed (IR) emission from young stellar populations for the unobscured star-forming galaxy SED.

### 1.3 Supermassive Black Holes

Ranging in mass from  $10^5$  to  $10^{10} M_{\odot}$ , SMBHs are believed to exist at the centre of many, if not all, massive galaxies. While the presence of SMBHs has been inferred in a number of galaxies in the local Universe (see review by Kormendy & Richstone, 1995), their formation and subsequent mass evolution remains a hotly debated topic. Before SMBHs can grow in mass, there must be BH seeds. While there is no scientific consensus on how such seeds form, two popular suggestions are that they originate from the remnants of Pop III stars (i.e. primordial stars; Haiman & Loeb, 2001) or from direct halo gas collapse (Begelman et al., 2006). From here, the seeds undergo mass growth via accretion to become SMBHs. While there are numerous ways this growth can occur (Alexander & Hickox, 2012), a popular scenario is via the large influx of gas during a major galaxy merger. (Bonoli et al., 2014).

Observational evidence for mass accretion onto SMBHs came in the mid 20th century with the study of extremely bright radio sources in association with optical point sources (Schmidt, 1963). Dubbed quasars, which is short for quasi-stellar radio source, these unique objects appeared like stars at optical wavelengths but exhibited emission lines that suggested

their gas temperatures are higher than possible in even the most luminous stars. It has since been determined that these unique emission lines are the product of energetic mass accretion on to a distant galaxy's SMBH. These sources are commonly referred to as active galactic nuclei (AGN). Today, the term "quasar" is commonly used to refer to a luminous subset of AGN.

### 1.3.1 Active Galactic Nuclei

The bulk of emission from an AGN tends to come from a very compact, and typically unresolved central region of a galaxy, less than a few parsec in diameter. Despite this small size, the luminosity of an AGN can significantly exceed that of its entire host galaxy, by as much as a factor of a thousand. As mentioned in Section 1.3, the most commonly accepted reason for this emission is due to the accretion of matter on to an SMBH. In the innermost region, an accretion disk forms from this matter (e.g. cold gas and dust) as it infalls on to an SMBH. Compared to the host galaxy, this disk is very compact and more comparable in size to that of our Solar System (Hawkins, 2006). The rate of infalling matter also dictates the properties of the disc. For example, at higher accretion rates, the disk is geometrically thin yet optically thick (Shakura & Sunyaev, 1973), but at low accretion rates, the opposite is true (Narayan & Yi, 1995; Esin et al., 1996). During the accretion process, the disk is subjected to shear stresses, which causes the material to heat and radiate like a collection of black bodies. The total luminosity from such radiation is calculated by,

$$L = \epsilon c^2 dm/dt \quad (1.1)$$

where  $\epsilon$  is the accretion efficiency,  $dm/dt$  is the mass accretion rate, and  $c$  is the speed of light. The accretion efficiency (often assumed to be  $\epsilon = 0.1$ ) can range from 0.05 – 0.42 (Marconi et al., 2004), depending on the spin of the BH (see Kerr, 1963).

The long-term stability of AGN accretion is dictated by the gravitational force and radiation pressure caused by the AGN. The gravitational force, due to Newtonian gravity, is given by,

$$F_{\text{grav}} = \frac{GMm_p}{r^2} \quad (1.2)$$



where  $G$  is the gravitational constant ( $6.67^{-11} \text{m}^3 \text{s}^{-2} \text{kg}^{-1}$ ),  $r$  is the distance between the two objects,  $M$  is the mass of the central object, and  $m_p$  is the mass of a proton. The radiation force due to Thompson scattering is given by,

$$F_{\text{rad}} = \frac{L\sigma_T}{4\pi cr^2} \quad (1.3)$$

where  $L$  is the luminosity of the object,  $c$  is the speed of light, and  $\sigma_T$  is the Thompson cross section or the effective area of an electron when it is illuminated by radiation. For stability, the AGN requires the gravitational force to be equal or greater than the radiation pressure from the AGN,  $F_{\text{grav}} > F_{\text{rad}}$ . Rearranging for luminosity, we can show,

$$L = \frac{4\pi GMm_p c}{\sigma_T} \simeq 3.2 \times 10^4 \left( \frac{M}{M_\odot} \right) L_\odot \quad (1.4)$$

where  $M_\odot$  and  $L_\odot$  are units of solar mass and solar luminosity, respectively. If the accretion luminosity is greater than this, the pressure due to radiation exceeds the gravitational force and material is blown away from the SMBH, which essentially chokes it of fuel. This luminosity limit is known as the Eddington luminosity and dictates the theoretical maximum accretion rate onto an accreting body under certain idealised circumstances (Begelman, 1979). That said, super-Eddington accretion is possible when relaxing assumptions such as the assumed accretion efficiency and the need for perfect spherical symmetry (Abramowicz et al., 1988).

### AGN Bolometric Luminosity

While the term ‘bolometric’ luminosity is used to describe the energy emitted across the whole electromagnetic spectrum, in this thesis, bolometric luminosity is used to refer to the total accretion luminosity emitted primarily from UV to the far infrared (FIR) or 0.3 – 160  $\mu\text{m}$ . Figure 1.2 illustrates an AGN SED, from radio frequencies to the gamma-ray regime, and the various physical components that make up the total observed SED. Of course, the relative contributions of these components can vary greatly depending on the type of AGN, which is discussed further in the following section.

### 1.3.2 AGN Structure and the Unified Model

In Figure 1.3, we illustrate the primary components for the internal structure of an AGN. At the very centre, the SMBH is surrounded by a sub-parsec scale accretion disk. Encompassing this, from 0.1-10 parsec, a dusty structure known as a torus is shown. While the origin and structure of the dusty torus remains a hotly debated topic (e.g. Nenkova et al., 2002; Elitzur

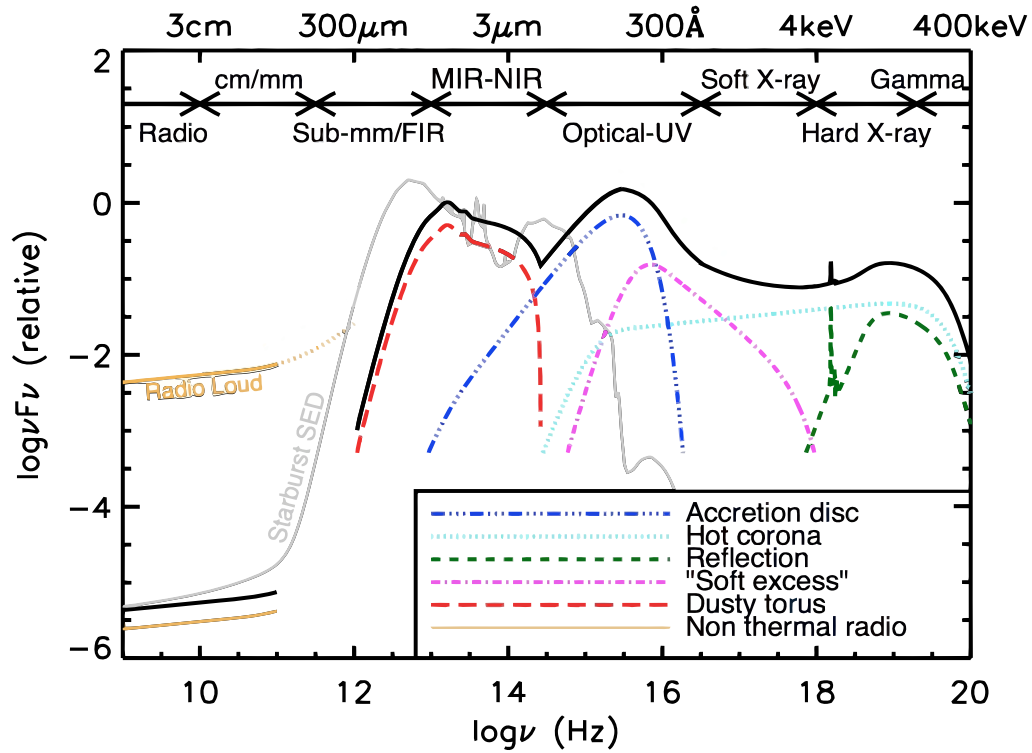


**Fig. 1.2** Schematic representation of an AGN SED (Adapted from Harrison, 2016), from radio frequencies to the gamma-ray regime (black solid line). The different coloured lines represent the emission from individual components that make up the AGN. Also shown is a typical spectrum for a starburst galaxy (M82; light-grey line)

& Ho, 2009; Netzer, 2015), models suggest it may be a natural consequence of accretion disk evolution (Montesinos Armijo & de Freitas Pacheco, 2011). The largest feature depicted is a radio jet, which protruded perpendicular from both sides of the torus. These radio jets consist of collimated charged particles that are accelerated away from the central region and can reach distances of up to a megaparsec (Mpc). These large-scale jets are characteristic of luminous radio galaxies, but smaller scale jets can also be found in radio-quiet AGN as well (Ulvestad & Wilson, 1984).

Figure 1.3 also illustrates the unified model of AGN (Antonucci, 1993; Urry & Padovani, 1995) by way of a semi-circle of observer vantage points. The term “unified model” was first proposed by Rowan-Robinson (1977) and provides relief from a muddled nomenclature resulting from an overwhelming number of different classes of AGN, which are likely the same phenomenon observed from different directions. The zoo of nomenclature (see Padovani et al., 2017) is illustrated in the flowchart of Figure 1.4. This AGN zoo reflects various observational modes or selections that are sensitive to specific configurations of geometry, power, etc. While such naming schemes can prove useful to reflect differences in the underlying physical scenario, broadly speaking, AGN can be split into either Type I or Type II and reside in either a radio loud or radio quiet galaxy.

### Broad Line Region

AGN that exhibit an optical spectra with broad high-ionisation emission lines are classified as Type I. The width of these lines range from  $\Delta v_{\text{FWHM}} \approx 500 \text{ km s}^{-1}$  to  $\Delta v_{\text{FWHM}} \gtrsim 10^4 \text{ km s}^{-1}$ . A Type I classification suggests the observer has a predominantly unobscured view into the very centre of the AGN. It is here, high energy photons from the accretion disk heat the surrounding gas, leading to broad emission line features due to doppler broadening. Known as the broad line region (BLR), this area is between 0.01 pc and 1 pc from the central SMBH and is therefore currently unable to be spatially resolved using current imaging techniques. Therefore, the indirect information provided by the emission lines provides a useful way to study the region.

### Narrow Line Region

Unlike Type I AGN, Type II are obscured from the BLR and instead exhibit narrower emission lines in the range of  $200 \lesssim \Delta v_{\text{FWHM}} \lesssim 900 \text{ km s}^{-1}$ , with a typical value of around  $400 \text{ km s}^{-1}$ . These lines originate from a spatially extended region from the central SMBH, around 100 to 1000 pc away, in the narrow line region (NLR). Although, they are known to extend to as far as 10 kpc or more (Hainline et al., 2013, 2014). Within the NLR, low-density gas is exposed

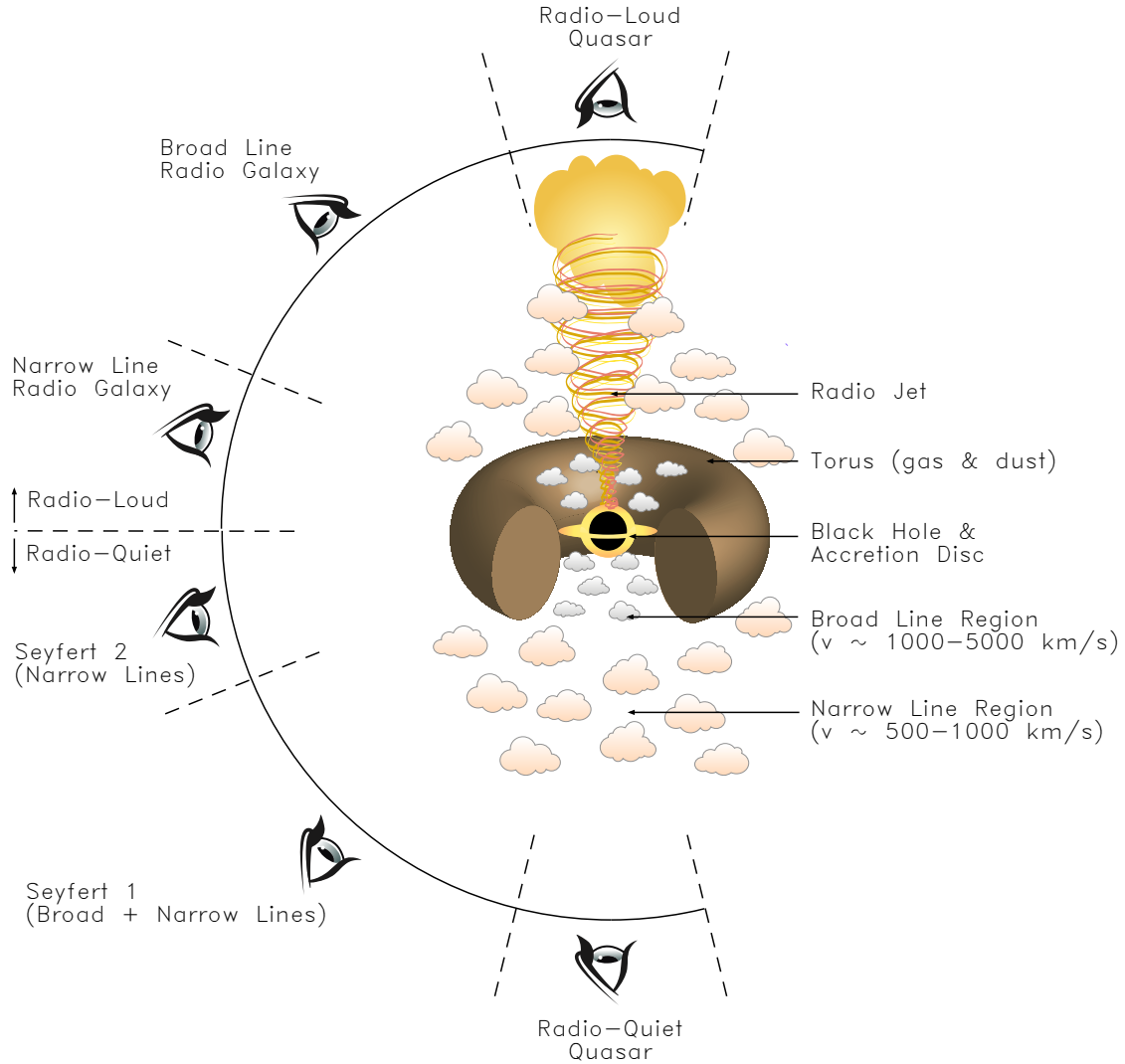


**Fig. 1.3** Schematic diagram to illustrate the structure and components of a typical AGN, according to the Unified Model. The central SMBH is surrounded by an accretion disk, which in turn is surrounded by a dusty torus. Above and below the accretion disk, two distinct emission line regions are present: (1) the broad-line region (BLR) between 0.01 pc and 1 pc from the SMBH and (2) the narrow-line region (NLR) that extends out to 1000 pc. Radio jets may also protrude perpendicularly from the accretion disk. The observed emission from the AGN depends on the inclination angle with respect to the observer. The semi-circle of observer points illustrates this. For example, the obscuration by the torus prevents the BLR from being directly observed, while the emission from the NLR is less dependent on the line of sight.

to lower ionisation than the BLR, which produces comparatively narrower emission lines. Unlike the BLR, the NLR can be spatially resolved in the optical, thus providing critical information to inner workings of an AGN (e.g. Kaiser et al., 2000).

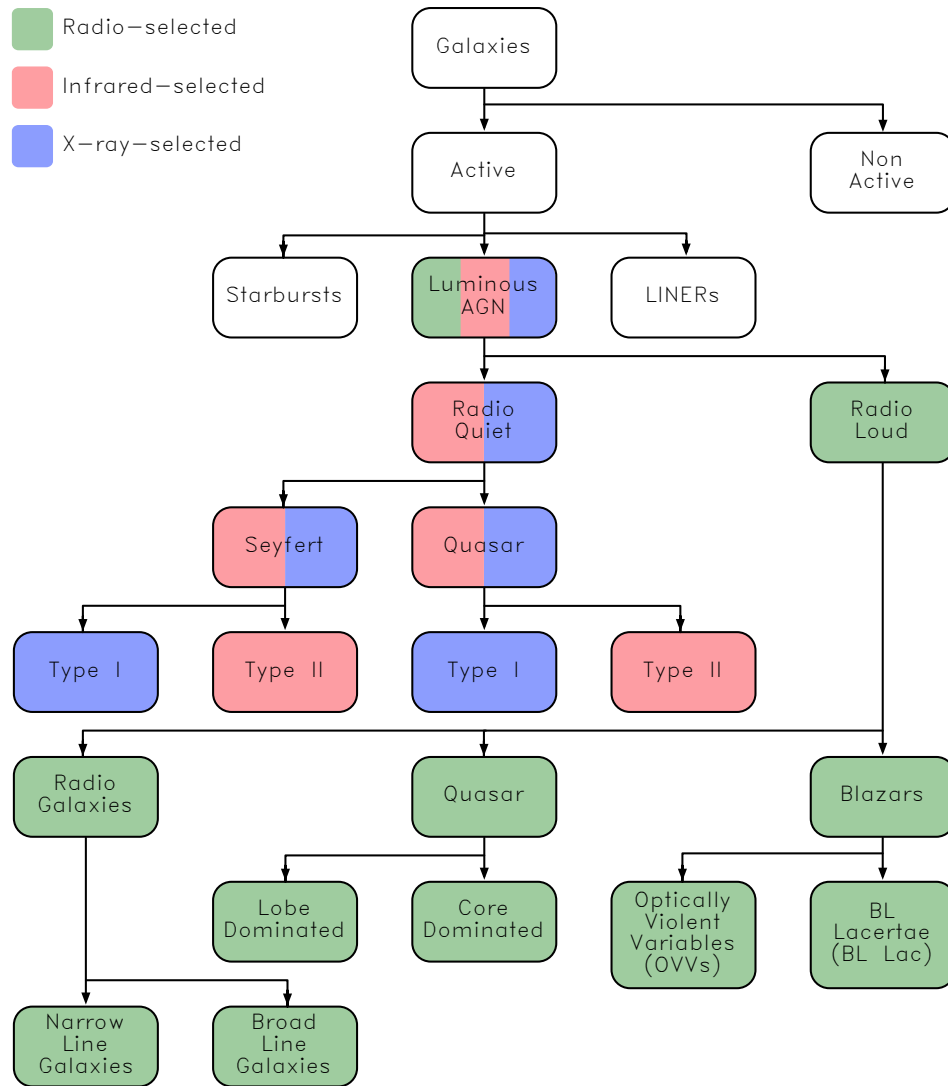


**Fig. 1.4** Flowchart guide to the AGN classes and how each is related to the other. Starting from the top, galaxies can either be active (AGN) or non-active. From there, the AGN are split into their respective subclasses. Chapter 2 details the selection techniques used to identify AGN in this thesis. We adopt three primary selection techniques, which are colour-coded as follows: red blocks are primarily identified using IR-based AGN selection, blue blocks use X-ray-based AGN selection, and green blocks use radio-based AGN selection.

### Dusty Torus

A key component to the unified model is the dusty torus, which extends past the BLR, but inside the NLR (Antonucci & Miller, 1985). With a radius of up to a few hundred pc, the obscuring medium of the torus exhibits gas densities of about  $10^4 - 10^7 \text{ cm}^{-3}$ , velocities of order  $1000 \text{ km s}^{-1}$ , and a large range of column densities from  $N_{\text{H}} \sim 10^{20} - 10^{27} \text{ cm}^{-2}$  (Hopkins et al., 2011). The basic assumption of the unified model is that, depending on the viewing angle of the observer, the obscuring medium of the torus will block the emission from the BLR, resulting in a Type II class AGN. For favourable angles, such as viewing perpendicular to the torus, the BLR is not obscured and allows a view of the NLR, which results in a Type I class AGN.

### Radio Loudness

While the Type I / Type II classification detailed above is primarily an optical-based scheme, radio astronomers have their own unique approach. Again, their classifications are numerous, and the nomenclature is muddled (see Figure 1.4), but broadly speaking, they use a dichotomic approach of radio loud (RL) or radio quiet (RQ) when identifying AGN. As radio emission is produced by both star formation and an AGN, the difference between RL and RQ is based on the ratio of radio to optical flux. A common criterion (Kellermann et al., 1989) is that RL objects exhibit a ratio of  $f_{5\text{GHz}}/f_{4400\text{\AA}}$  in the range of 10-1000, while RQ fall in the range 0.1-1. While there are several variations of this approach (e.g. Kellermann et al., 1989; Ivezić et al., 2002; Rees et al., 2016), studies have argued against such a distinct dichotomy (e.g. Lacy et al., 2001; Cirasuolo et al., 2003). Regardless, those sources that exhibit both a high  $f_{5\text{GHz}}/f_{4400\text{\AA}}$  ratio and visible radio jets are undoubtedly considered an RL AGN.

## 1.4 The Relationship Between SMBHs and Their Hosts

Despite an incredible nine orders of magnitude difference in the physical size between an SMBH and its host galaxy, studies have shown significant connections exist between the two. For example, tight correlations have been found between SMBH mass and various properties of its host galaxy (see Kormendy & Ho 2013 for a recent review), such as its stellar velocity dispersion ( $M_{\text{BH}} - \sigma$ ; Ferrarese & Merritt, 2000; Gebhardt et al., 2000; Tremaine et al., 2002; Gültekin et al., 2009; Graham et al., 2011), spheroidal luminosity ( $M_{\text{BH}} - L_{\text{bulge}}$ ; Kormendy & Richstone, 1995; Graham, 2007; Sani et al., 2011), and bulge mass ( $M_{\text{BH}} - M_{\text{bulge}}$ ; Magorrian et al., 1998; Marconi & Hunt, 2003; Häring & Rix, 2004; Beifiori et al., 2011). Further to this, a broad connection between actively accreting black

holes and star formation has also been shown to exist. As shown in Figure 1.5, the volume average of the BH accretion rate (BHAR) tracks a similar evolutionary path to that of the global density of SFR in galaxies. Both of these observables peaks between  $z = 2 - 2.5$ , before declining towards the present day (Boyle & Terlevich, 1998; Merloni et al., 2004; Marconi et al., 2004; Silverman et al., 2008; Shankar et al., 2008; Madau & Dickinson, 2014). While a simple explanation for these connections is a common fuel supply, star-forming regions can span kiloparsecs, yet an actively accreting SMBH relies on material within a radius of  $\sim 10 - 100\text{pc}$ . As the natural flow of cold gas from one region to another can take as long as an entire AGN phase ( $\geq 10^8$  yrs; Martini, 2004; Hopkins et al., 2005), other mechanisms are required to facilitate the process.

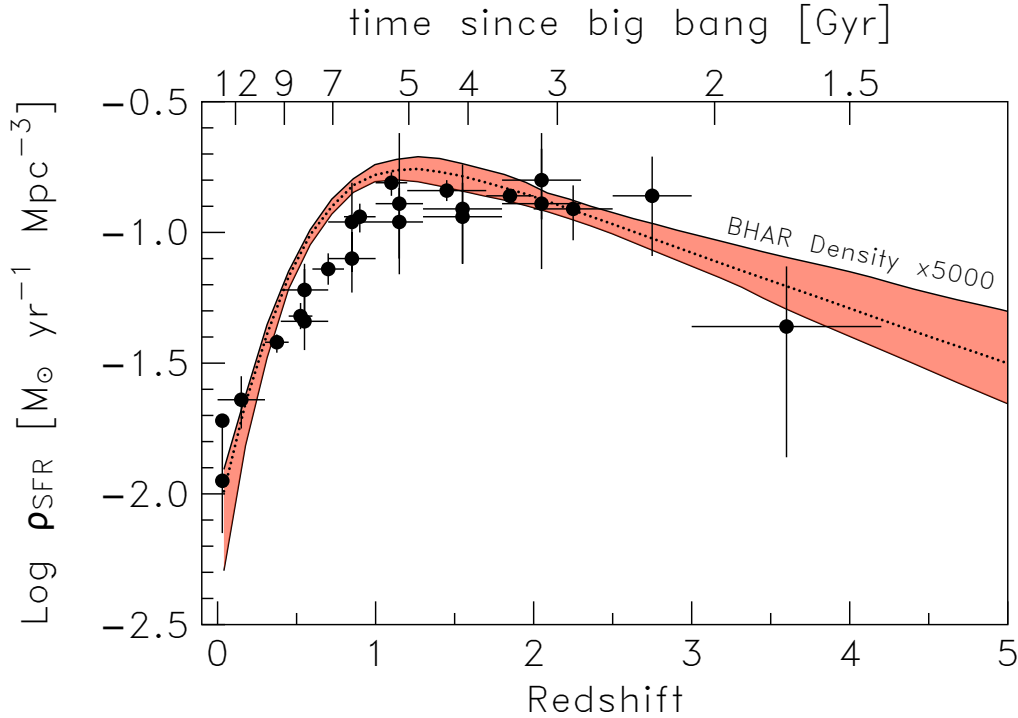


**Fig. 1.5** Comparison of the volume averaged cosmic (IR-derived) SFR density (circles; Madau & Dickinson, 2014) and (X-ray-derived) black hole accretion rate (BHAR) density (dotted line; Aird et al., 2010). The BHAR density is scaled up by a factor of 5000, while the red shading indicates a  $1\sigma$  uncertainty region.

### 1.4.1 Gas Inflows & Outflows

As mentioned in Section 1.4, a joint fuel supply, by way of cold gas, may help regulate both SMBH and galaxy growth. Major mergers are often attributed to this process (Silverman et al., 2011; Satyapal et al., 2014; Ellison et al., 2015), whereby gravitational torques allow

gas inflow to trigger an AGN (Jogee, 2006; Haan et al., 2009; Querejeta et al., 2016). On the condition there remains sufficient undisturbed gas flowing into a galaxy, star formation also occurs during this process (Negroponte & White, 1983; Springel, 2000; Di Matteo et al., 2008; Knapen & James, 2009). Hydro-dynamical simulations support this major merger scenario (Hopkins & Quataert, 2010), while observations of AGN-powered ultraluminous IR galaxies (ULIRGs) show clear signs of past merger events (Clements et al., 1996). The luminous IR emission in these galaxies also points to high SFRs. However, the merger-driven scenario may be limited to the most luminous AGN ( $L_{\text{AGN}} > 10^{12} L_{\odot}$ ; Hasinger, 2008; Kartaltepe et al., 2010; Treister et al., 2012), which are rare at low redshifts.

For moderate luminosity AGN, minor mergers are a known trigger (Shabala et al., 2012), but a more gradual process, known as secular evolution, is favoured. Here, other mechanisms like disk instabilities, galaxy bars, and large-scale gravitational torques can cause gas inflow. Despite being a slower process, secular evolution can still trigger AGN activity and enhance star formation (Kormendy & Kennicutt, 2004; García-Burillo et al., 2005; Simoes Lopes et al., 2007; Hopkins & Quataert, 2010).

During the AGN accretion process, the gas flowing onto an SMBH produces ionising photons, which lead to the power-law spectrum observed in AGN (see Figure 1.2). When accretion reaches its Eddington limit, radiation pressure can launch galactic-scale winds, which can heat or remove large amounts of cold gas from the central region (Harwit, 1962; Chiao & Wickramasinghe, 1972; Murray et al., 2005, 2011; Krumholz & Thompson, 2013). After this phase, the SMBH is starved of its fuel supply and is less radiatively efficient ( $\lambda_{\text{EDD}} \lesssim 10^{-2}$ ). This leads to the release of mechanical energy in the form of non-thermal radio jets, which can inject energy at kiloparsec scales into the surrounding medium of the host (e.g. Hopkins et al., 2008, 2011).

AGN outflows, commonly referred to as “negative feedback” can help explain the observed correlations between an SMBH and its host. Indeed, the energy released by an actively accreting SMBH into the surrounding gas content can lead to such correlations. If the SMBH is of sufficient mass, these outflows will result in residual gas ejection, which regulates star formation. Theoretical simulations commonly invoke this process to regulate SMBH and stellar mass accretion to reproduce the observed galaxy mass function and avoid the overproduction of massive galaxies in cosmological models (e.g. Ciotti & Ostriker, 1997; Silk & Rees, 1998; Di Matteo et al., 2005; Croton et al., 2006; Menci et al., 2008; King, 2010; Zubovas & King, 2012; Fabian, 2012; Faucher-Giguère & Quataert, 2012; Zubovas & King, 2012; Costa et al., 2014; King & Pounds, 2015; Richardson et al., 2016).

While supernovae feedback is another process known to deplete cold gas and regulate star formation, it scales linearly with SFR, meaning its efficiency decreases in massive galaxies



(Dekel & Silk, 1986). Negative feedback from AGN outflows is a more effective interaction and has been observed in elliptical galaxies at the centres of local clusters, which contain X-ray cavities filled with relativistic gas (e.g. Fabian et al., 2006; Forman et al., 2007). Often referred to as ‘bubbles’, these cavities are believed to be inflated by radio jets from RL AGN. The kinetic power from the central region of such clusters can be more than  $10^{45}$  ergs  $\text{s}^{-1}$ , which is sufficient to heat cooling flows in the intracluster medium (e.g. Böhringer et al., 2002).

Further evidence of negative feedback comes from RQ AGN (i.e. radiatively efficient AGN), which tend to be hosted by “transitional” galaxies that exhibit colours between red early-type and blue late-type galaxies (e.g. Silverman et al., 2008). These AGN generate high energy photons, which can ionise neutral atoms and heat the gas through photoionisation heating. Such heating can significantly suppress cold gas and thus star formation in low mass halos. In the case of galaxies that contain significant amounts of dust, the radiative energy from an AGN is efficiently channelled into the surrounding gas. While this energy is absorbed by dust grains and re-emitted in the IR, radiation pressure can generate momentum-driven winds, which can remove the surrounding cold gas (e.g. Murray et al., 2005).

Despite some evidence of AGN outflows exerting negative feedback on star formation in their host, recent studies also point to the possibility of positive feedback, whereby enhanced pressure from AGN outflows accelerate molecular cloud formation and thus star formation. (e.g. Silk, 2005; Elbaz et al., 2009; Zinn et al., 2013). Direct observational evidence of such feedback has been observed in both Centaurus A (Rejkuba et al., 2002; Crockett et al., 2012) and Minkowski’s Object (Croft et al., 2006; Lacy et al., 2017).

### 1.4.2 Correlation Between SFR and AGN Activity

In the above, we have seen that negative feedback from an AGN can help explain SMBH-galaxy correlations, such as the  $M_{\text{BH}} - \sigma$  relation, and help reproduce the observed galaxy mass function. However, we also saw AGN outflows can result in positive feedback and the enhancement of star formation. To help make progress, studies have investigated AGN at higher redshifts in order to monitor whether the feedback processes were different in the progenitors of the local galaxy population (e.g. Lutz et al., 2010; Shao et al., 2010; Harrison et al., 2012; Mullaney et al., 2012b; Santini et al., 2012; Rosario et al., 2013; Lanzuisi et al., 2015; Stanley et al., 2015). If positive feedback does indeed enhance star formation, the expectation is these results will return a correlation between the SFR and AGN luminosity of these samples. However, current findings are contradictory, with studies finding either a positive correlation (e.g. Lutz et al., 2010; Rovilos et al., 2012; Santini et al., 2012), negative correlation (e.g. Page et al., 2012; Barger et al., 2015), or even no correlation between the

mean SFR and AGN luminosity of active galaxies (e.g. Harrison et al., 2012; Rosario et al., 2012; Azadi et al., 2015; Stanley et al., 2015). While the origin of these contradictory results remains debated, it is likely a variety of limitations contribute, including the possibility of small sample sizes, limited redshift coverage, AGN contamination in estimating SFRs, and various other factors associated with sample selection.

This thesis attempts to overcome these limitations by expanding on the above works by: (1) compiling a statistically robust sample of evolving galaxies, from the peak time of activity ( $z \sim 2.5$ ) towards the present; (2) selecting AGN using the latest multi-wavelength selection techniques; (3) deriving SFRs free from AGN contamination using FIR photometry and SED decomposition techniques; (4) and placing the results in the context of redshift and stellar mass dependencies.

## 1.5 Observational Surveys and Facilities

The work in this thesis is based on observational data from various sources. As such, it is critical to understand the capabilities and limitations of the observational facilities from which this data was sourced. In the following sections, a brief review of the various surveys and facilities used is presented.

### 1.5.1 ZFOURGE

The FourStar Galaxy Evolution Survey or ZFOURGE covers three  $11' \times 11'$  pointings in the CDFS (*Chandra* Deep Field South; Giacconi et al., 2002), COSMOS (Cosmological Evolution Survey; Scoville et al., 2007) and UDS (Ultra Deep Survey; Lawrence et al., 2007) legacy fields. ZFOURGE uniquely employs deep near-IR imaging taken with five medium-band filters on the FourStar imager (Persson et al., 2013) mounted on the 6.5m Magellan Baade telescope. The imaging reaches  $5\sigma$  point-source limiting depths of  $\sim 26$  AB mag in  $J_1, J_2, J_3$  and  $\sim 25$  AB mag in  $H_s, H_1, K_s$  (Spitler et al., 2012). For galaxies at redshifts  $z = 1.5 - 4$ , these filters bracket the rest-frame  $4000\text{\AA}$ /Balmer breaks, resulting in well-constrained photometric redshifts within  $\sigma(z)/(1+z) \approx 1 - 2\%$  (e.g. Kawanwanichakij et al., 2014; Straatman et al., 2016). ZFOURGE is supplemented with existing data from CANDELS HST/WFC3/F160W (Grogin et al., 2011; Koekemoer et al., 2011; Skelton et al., 2014) and *Spitzer*/IRAC, as well as other ground-based imaging, to generate multi-wavelength catalogues spanning  $0.3 - 8 \mu\text{m}$ . Fluxes at wavelengths of the Infrared Array Camera (IRAC; Fazio et al., 2004),  $3.6, 4.5, 6.8,$  and  $8.0 \mu\text{m}$  are measured using the deblending approach

described in Labbé et al. (2006). For further details on the acquisition, data reduction, and bands used to construct the ZFOURGE catalogues, see Straatman et al. (2016).

### **Magellan/FourStar**

The Magellan telescopes are a set of twin 6.5m telescopes located 60m apart on the Cerro Manqui peak at the Las Campanas Observatory in Chile. Built and operated by a consortium of institutions led by the Carnegie Institution for Science, the telescopes experienced first light approximately two years apart, with Magellan Baade on the 15th of September 2000 and Magellan Clay on the 7th of September 2002. While the telescopes are equipped with an array of instruments, this thesis makes use of data from the wide field near-infrared camera, FourStar. Fitted to the Magellan Baade in 2009, FourStar is a 1.0-2.5  $\mu\text{m}$  near-IR camera built by Carnegie Observatories and the Instrument Development Group. (Persson et al., 2013). The instrument is equipped with four arrays that produce a 10.9 arcminute square field of view. The combination of outstanding seeing at the Las Campanas with the sensitivity, image quality and field of view of FourStar, allows us to select galaxies by their stellar mass and trace the evolution of rest-frame visible light to very early epochs.

### **Spitzer**

NASA's Spitzer Space Telescope (Werner et al., 2004) is a cryogenically cooled IR space telescope, launched into a heliocentric orbit on the 25th of August 2003 from Cape Canaveral aboard a Delta II 7920H rocket. The *Spitzer's* primary mirror is an 85cm, f/12, which is cooled to  $-268^\circ\text{C}$ . Fitted with a number of instruments to perform photometry, spectroscopy, and spectrophotometry, *Spitzer's* Infrared Array Camera (IRAC; Fazio et al., 2004) and Multiband Imaging Photometer for *Spitzer* (MIPS; Rieke et al., 2004) are the focus in this thesis. IRAC is a four-channel camera, which provides simultaneous 5.2 arcminute square images at 3.6, 4.5, 5.8, and 8  $\mu\text{m}$ . Complementary to IRAC, MIPS operates at longer wavelengths towards the far-IR. Specifically, MIPS makes use of three detector arrays at 24, 70, and 160  $\mu\text{m}$ . The field of view for MIPS varies from 5 x 5 arcminutes at its shortest wavelength to about 0.5 x 5 arcmin at its longest. In this thesis, *Spitzer* data are used to identify AGN hosted galaxies out to high- $z$  (see Section 2.3.5).

## **1.5.2 Ancillary Sources**

As mentioned in Section 1.3.1, emission from an AGN spans a vast range of photon energy, which makes multi-wavelength data critical to adequately identify and study them and their

hosts over a broad redshift range. To supplement the optical and IR data of ZFOURGE, we make use of additional far-IR, X-ray, and radio data from the following facilities.

### **Herschel**

The Herschel Space Observatory (Pilbratt et al., 2010) is an ESA-administered space telescope sensitive to the far-IR and sub-mm (55–672  $\mu\text{m}$ ), which was launched on May 14th, 2009 from the Guiana Space Centre via an Ariane 5 rocket towards the second Lagrangian point. At more than four times the size of any previous IR space-based telescope, *Herschel*'s primary mirror is 3.5m in diameter, which allows it to collect almost 20 times more light than its predecessors. Though no longer operational, during its mission, *Herschel* utilised three detectors: the Photodetecting Array Camera and Spectrometer (PACS; Poglitsch et al., 2010), the Spectral and Photometric Imaging Receiver (SPIRE; Griffin et al., 2010), and the Heterodyne Instrument for the Far Infrared (HIFI; de Graauw et al., 2010). For this thesis, we make use of PACS photometry. In photometry mode, the PACS imager was able to simultaneously observe in two bands, 60–85  $\mu\text{m}$  (PACS Blue,  $\lambda_{\text{mean}} \sim 70 \mu\text{m}$ ) or 85–130  $\mu\text{m}$  (PACS Green,  $\lambda_{\text{mean}} \sim 100 \mu\text{m}$ ) and 130–210  $\mu\text{m}$  (PACS red,  $\lambda_{\text{mean}} \sim 160 \mu\text{m}$ ) with a detection limit of a few millijanskies and a field of view of  $\sim 1.75' \times 3.5'$ . In this thesis, PACS data are used to study the properties of AGN hosted galaxies out to high- $z$  (see Section 2.2.3).

### **Chandra**

NASA's Chandra X-ray Observatory (Weisskopf et al., 2000) is an X-ray space telescope, which was launched into a geocentric orbit on July 23rd, 1999 from the Kennedy Space Center on board the Space Shuttle Columbia. Using the Advanced Charge-Coupled device (CCD) Imaging Spectrometer (ACIS; Garmire et al., 2003), *Chandra* operates in the photon energy range of 0.2–10 keV, taking images with its ten CCD chips at 0.5 arcsec with a 30 arcmin field of view. In this thesis, ACIS data are used to both identify and study AGN hosted galaxies out to high- $z$  (see Section 2.2.2).

### **XMM-Newton**

The X-ray Multi-Mirror Mission or *XMM-Newton* (Jansen et al., 2001) is an ESA administered X-ray space telescope, which was launched into a geocentric orbit on the 10th of December 1999 from the Guiana Space Centre via an Ariane 5G rocket. The primary instruments on the *XMM-Newton*, providing both imaging and spectroscopy, are the three European Photon Imaging Cameras (EPIC; Turner et al., 2001). While the *XMM-Newton* operates over a slightly larger photon energy range (0.15 to 15 keV) to *Chandra*, it does

so with a more coarser angular resolution of about six arcsec. Like *Chandra*, we use data from the *XMM-Newton* to both identify and study AGN hosted galaxies out to high- $z$  (see Section 2.2.2).

### Very Large Array

The Very Large Array (VLA) is a 27-element interferometric array, which is located in central New Mexico on the Plains of San Agustin and operated by the National Radio Astronomy Observatory (NRAO)<sup>1</sup>. The first antenna was constructed in September 1975, and the complex was inaugurated in 1980. Each of the 27 antennae, which are placed in a Y-shaped configuration, are 25 m in diameter. The antennas are outfitted with receivers for seven fixed observing wavelengths centred near 90, 20, 6, 3.6, 2.0, 1.3, and 0.7 cm. In this thesis, we use data from observations performed at a frequency of 1.4 GHz (21 cm) to identify RL AGN hosted galaxies out to high- $z$  (see Section 2.2.2).

## 1.6 Thesis Overview

This thesis aims to investigate the nature of the connection between AGN and their hosts across a broad redshift range, including the peak of AGN and SF activity. The ZFOURGE catalogues grant access to high-quality photometric redshifts, deep  $K_s$ -band selected galaxies (i.e. high- $z$  mass selection), and multi-wavelength AGN selection techniques, which places this work in a unique position to advance our knowledge. The results will be presented in three chapters, with each being relatively independent, yet closely related. This thesis strives to overcome the limitations faced by previous studies, most notably, the challenge of accurately separating the AGN and SF components of each galaxy. This challenge is emphasised throughout this thesis, with each chapter adopting a unique approach in an attempt to test its effectiveness. The chapters included in this thesis are:

- **Chapter 2 - Selecting AGN in ZFOURGE**

This chapter focuses on methods for selecting AGN in the ZFOURGE catalogues. As variations in luminosity, morphology, orientation and dust obscuration make constructing a thorough and unbiased sample of AGN a formidable task, we apply a multi-wavelength, multi-technique approach to best overcome the challenge. By coupling this approach with the highly accurate photometric redshifts of ZFOURGE, we produce one of the most complete

---

<sup>1</sup>The National Radio Astronomy Observatory is a facility of the National Science Foundation operated under cooperative agreement by Associated Universities, Inc.

and high-quality multi-wavelength AGN catalogues across the redshift range  $z = 0.2 - 3.2$ . These sources are used throughout the remainder of the thesis.

- **Chapter 3 - An Enhancement of Star Formation in AGN Hosts**

In this chapter, the impact of AGN activity on star formation is investigated by comparing 225 AGN host galaxies across  $z = 0.2 - 3.2$  to a sample of mass-matched inactive (non-AGN) sources. To overcome various selection biases found in previous works, we limit selection to a stellar-mass cut of  $\log(M_*/M_\odot) \geq 9.75$  with varying AGN luminosity limits based on the thresholds of their respective wavebands (i.e.  $L_{1.4\text{GHz}}$ ,  $L_X$  and  $L_{\text{IR}}$ ). Careful consideration of AGN contamination is also taken when performing the analysis.

- **Chapter 4 - Decoupled Black Hole Accretion and Quenching**

In this chapter, the SMBH-galaxy connection is investigated by tracking the mean BHAR and mean SFR of a sample of galaxies out to  $z = 2.5$ . While such studies are prevalent, they are often limited to AGN-selected or mass-limited samples, which contain a broad mixture of galaxies with different evolutionary histories. To address this, we use the ZFOURGE catalogues to construct two independent samples based on the mass-progenitors of the present-day Milky Way and Andromeda galaxy.

- **Chapter 5 - A Two Band Approach to Isolate the AGN Contribution to Observed SEDs**

In this Chapter, an approach to isolate the AGN contribution to the observed SED using only two wave bands is presented. Such an approach lends itself to studies where abundant photometric data may be lacking. While the approach is not without its limitations, we show it can reproduce underlying trends known to exist in active galaxy samples.

- **Chapter 6 - Conclusions and Future work**

In this chapter, a summary of all work in this thesis is presented, as well as their key results. An overview of current and future studies, based on the methods and results of this thesis, is also presented. This includes a section covering interim work selecting optically-identified AGN in the ZFIRE survey, which has contributed to several recent studies and has laid the groundwork for future investigations into the evolutionary impact of supermassive black holes on their host galaxies.

The work in this thesis is based on an AB magnitude system, a Chabrier (2003) IMF, and assumes a  $\Lambda$ CDM cosmology with  $H_0 = 70 \text{ km s}^{-1} \text{ Mpc}^{-1}$ ,  $\Omega_M = 0.3$ ,  $\Omega_\Lambda = 0.7$ .

# Chapter 2

## Selecting AGN in ZFOURGE

Portions of this chapter and chapter 3 are based on a single paper, which appears in *Monthly Notices of the Royal Astronomical Society*, 2016, Volume 457, 629-641. The co-authors are L. Spitler, K-V. Tran, G. Rees, I. Labbé, R. Allen, G. Brammer, K. Glazebrook, A. Hopkins, S. Juneau, G. Kacprzak, J. Mullaney, T. Nanayakkara, C. Papovich, R. Quadri, C. Straatman, A. Tomczak, and P. van Dokkum. L. Spitler, K-V. Tran, and I. Labbé supervised this work and provided guidance with respect to the methodology and scientific interpretation, G. Rees provided guidance with respect to the methodology of radio data analysis, and the remaining co-authors provided discussion and feedback towards the final manuscript. The candidate's contribution to the work presented in this paper is 95%.

### 2.1 Introduction

The diverse and complex interactions between an AGN and its host galaxy make constructing a thorough and unbiased sample a formidable task. Variations in luminosity, morphology, orientation and dust obscuration dictate the need for a multi-wavelength, multi-technique approach. For example, while optical and X-ray selection techniques are both highly efficient, they break down when AGN hosts are heavily obscured by large amounts of gas and dust (e.g. Lacy et al., 2006; Eckart et al., 2009). On the other hand, radio and IR selection techniques are relatively immune to dust extinction, but galaxies with copious amounts of star formation can contaminate a sample (e.g. Condon et al., 2002; Donley et al., 2005). In this chapter, we describe our approach to minimise such bias by constructing a robust AGN sample from multi-wavelength data of ZFOURGE. We restrict the sample to sources over  $z = 0.2 - 3.2$  with clean photometric detections in the ZFOURGE catalogues (e.g. near star

and low-signal-to-noise flags). Further details of the ZFOURGE quality control flags are presented in Straatman et al. (2016).

## 2.2 Multi-Wavelength Data

### 2.2.1 Radio Data

Following Rees et al. (2016), we cross-match ZFOURGE with published radio imaging at 1.4 GHz based on overlapping data from the VLA. We use the VLA 1.4 GHz Survey of the Extended *Chandra* Deep Field South: Second Data Release of Miller et al. (2013) for the ZFOURGE-CDFS field, the VLA-COSMOS Survey IV Deep Data and Joint catalogue of Schinnerer et al. (2010) for the ZFOURGE-COSMOS field, and the Subaru/XMM-Newton Deep Field-I 100  $\mu$ Jy catalogue of Simpson et al. (2006) for the ZFOURGE-UDS field. The minimum root-mean-square (RMS) sensitivity and resolution for each survey is 6  $\mu$ Jy/beam at  $2.8''$  by  $1.6''$ , 10  $\mu$ Jy/beam at  $1.5''$  by  $1.4''$ , and 100  $\mu$ Jy/beam at  $5.0''$  by  $4.0''$ , respectively. Figures 2.1 to 2.3 display the radio sources that match with  $K_s$ -band counterparts. Given the different approaches to astrometric calibration between the catalogues, we checked for systematic positional errors in each field by calculating the median offset in each direction between the sources. This offset is displayed in the top-right of Figures 2.1 to 2.3. The radio sources were shifted by this amount before being rematched to their  $K_s$ -band counterparts within a  $1''$  radius. Of the 286 radio sources that overlap with the ZFOURGE fields, 264 were cross-matched with a  $K_s$ -band counterpart. We visually inspect the remaining 22 sources and find 2 in the ZFOURGE-COSMOS field were missed due to confusion from complex extended structures (i.e. radio jets), with their recorded position offset from the galaxy core. The remaining 20 sources are considered candidate IR faint radio sources (IRFS; Norris et al., 2006), with a visual inspection yielding no identifiable counterparts in the  $K_s$ -band images. Considering this, a total of 266 radio counterparts are found in the ZFOURGE  $K_s$ -band images ( $\sim 92\%$  of all overlapping radio sources), with 119 in CDFS, 116 in COSMOS, and 31 in UDS.

### 2.2.2 X-ray Data

We cross-match ZFOURGE with published X-ray sources based on overlapping data from the *Chandra* and *XMM-Newton* space observatories. We use the *Chandra* Deep Field-South Survey: 4 Ms Source catalogue of Xue et al. (2011) for the ZFOURGE-CDFS field (X11 henceforth), the *Chandra* COSMOS Survey I. Overview and Point Source catalogue of Elvis



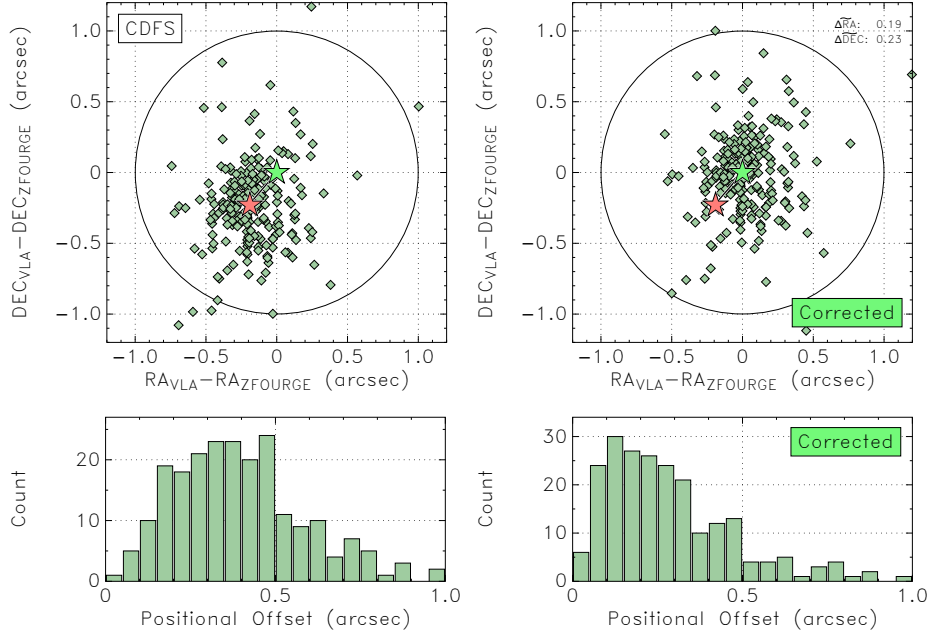


**Fig. 2.1** Positional offsets (in arcsecs) given by VLA minus ZFOURGE in CDFS. The top-left and bottom-left panels show the positional offsets on the sky and the histogram of separation for the sources before correction, respectively. The top-right and bottom-right panels show the same, after positional correction. In the top panel, the annotations list the median RA and DEC offsets, while the red star and green stars show the non-corrected and corrected median offsets, respectively. The cross-matching of sources was conducted post-correction.

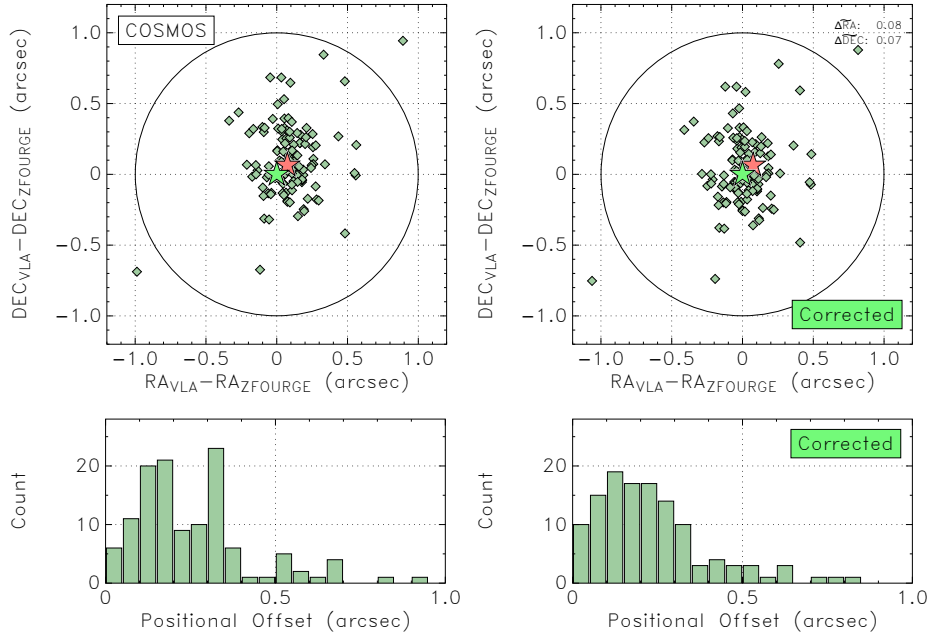


**Fig. 2.2** Positional offsets (in arcsecs) given by VLA minus ZFOURGE in COSMOS (see caption of Figure 2.1).

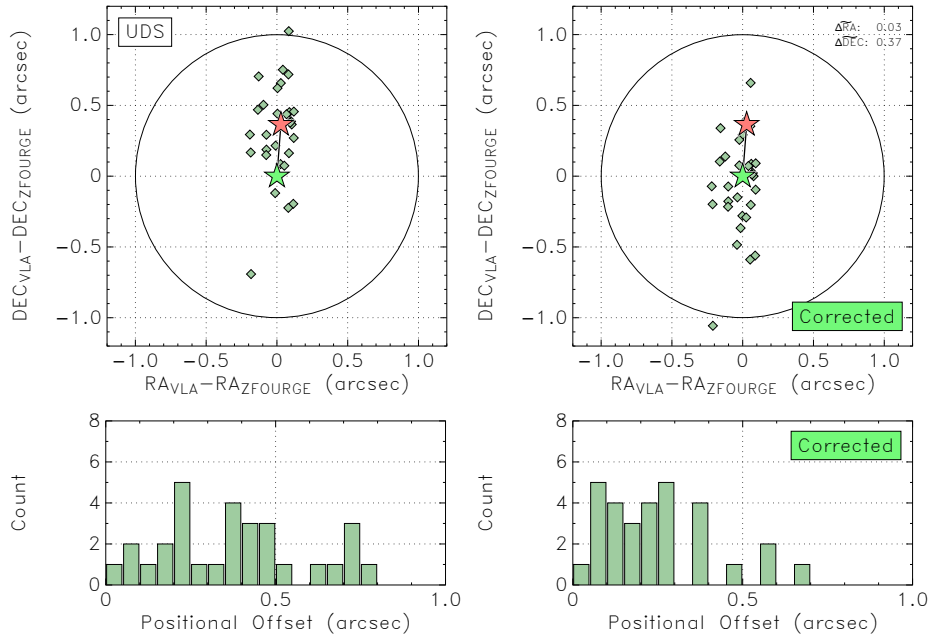


**Fig. 2.3** Positional offsets (in arcsecs) given by VLA minus ZFOURGE in UDS (see caption of Figure 2.1).

et al. (2009) for the ZFOURGE-COSMOS field (E09 henceforth), and the *Subaru/XMM-Newton* Deep Survey III. X-Ray Data of Ueda et al. (2008) for the ZFOURGE-UDS field (U08 henceforth). The on-axis limiting flux in the soft (low energy) and hard (high energy) bands for each survey is  $9.1 \times 10^{-18}$  and  $5.5 \times 10^{-17}$  erg cm $^{-2}$  s $^{-1}$ ,  $1.9 \times 10^{-16}$  and  $7.3 \times 10^{-16}$  erg cm $^{-2}$  s $^{-1}$ , and  $6.0 \times 10^{-16}$  and  $3.0 \times 10^{-15}$  erg cm $^{-2}$  s $^{-1}$ , respectively. Upon correcting for systematic position offsets in each field (see Figures 2.4 to 2.6), X-ray sources are cross-matched within a radius of  $4''$  of their  $K_s$ -band counterparts. Of the 683 X-ray sources that overlap with the ZFOURGE fields, 545 ( $\sim 80\%$ ) are found within  $1''$  of a  $K_s$ -band counterpart. A further 47 sources ( $\sim 7\%$ ) at  $>1''$  are added after a visual inspection of both the X-ray and  $K_s$ -band imaging confirmed no confusion from multiple sources within the matching radius. The remaining 91 sources yield no further matches with no visible counterparts identifiable. Considering this, a total of 592 X-ray counterparts are found in the ZFOURGE  $K_s$ -band images ( $\sim 87\%$  of all overlapping X-ray sources), with 422 in CDFS, 93 in COSMOS, and 77 in UDS.

### 2.2.3 Far-Infrared Data

We make use of overlapping *Spitzer*/MIPS and *Herschel*/PACS FIR imaging. The data used in this study are from 24 and 160  $\mu$ m photometry. We use imaging from the GOODS *Spitzer*

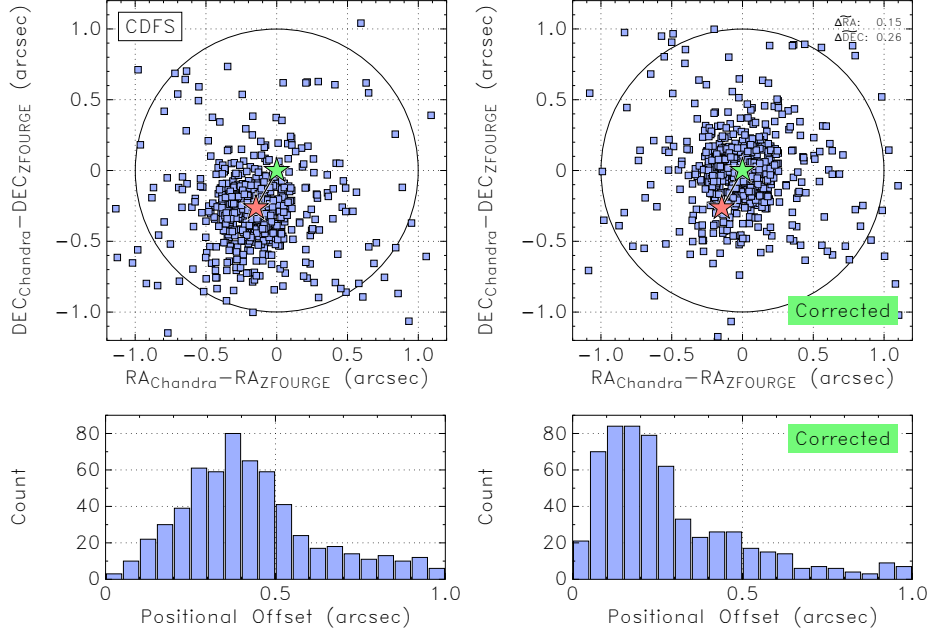


**Fig. 2.4** Positional offsets (in arcsecs) given by Chandra minus ZFOURGE in CDFS. The top-left and bottom-left panels show the positional offsets on the sky and the histogram of separation for the sources before correction, respectively. The top-right and bottom-right panels show the same, after positional correction. In the top panel, the annotations list the median RA and DEC offsets, while the red star and green stars show the non-corrected and corrected median offsets, respectively. The cross-matching of sources was conducted post-correction.

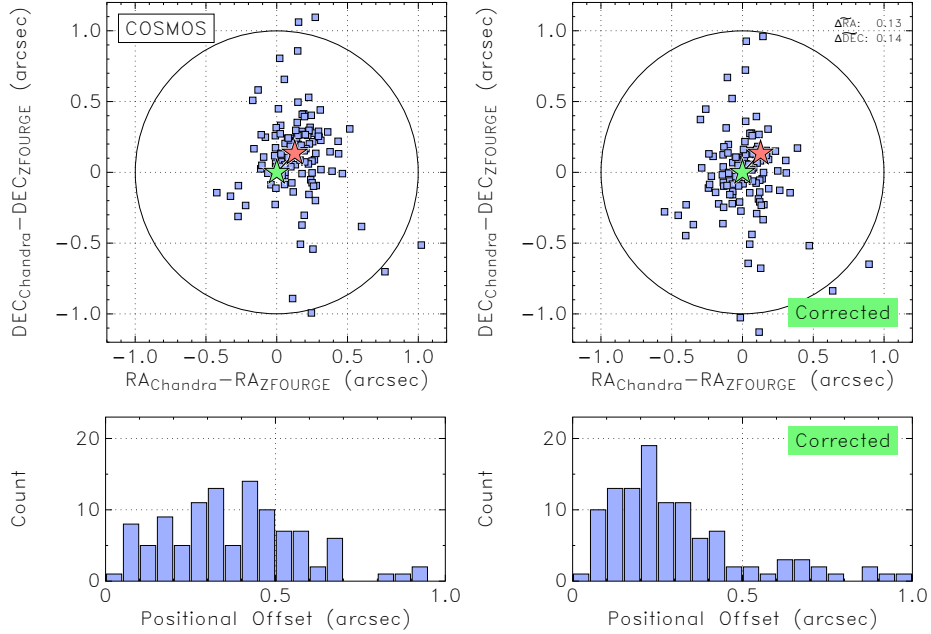


**Fig. 2.5** Positional offsets (in arcsecs) given by Chandra minus ZFOURGE in COSMOS (see caption of Figure 2.4).

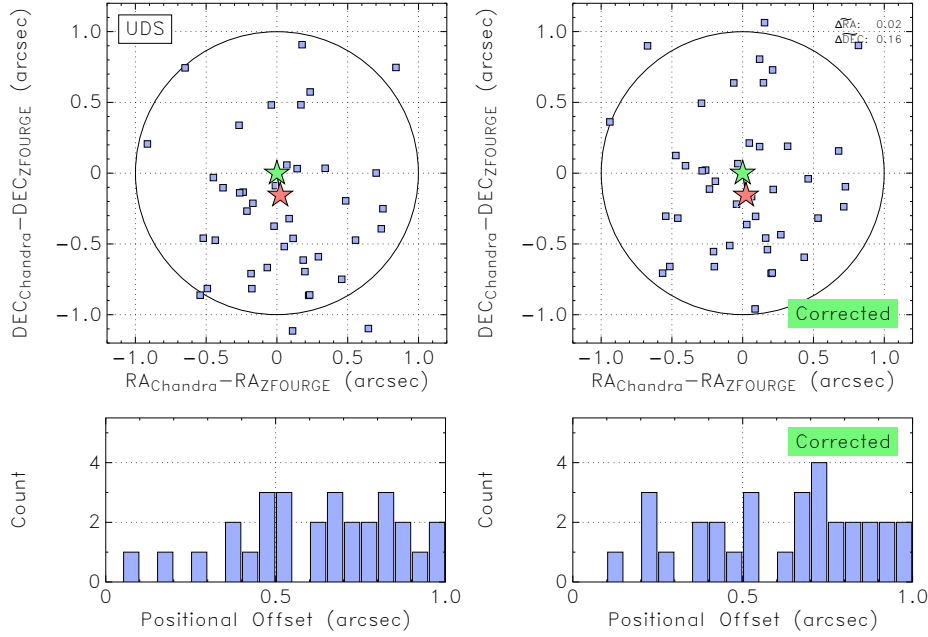


**Fig. 2.6** Positional offsets (in arcsecs) given by XMM-Newton minus ZFOURGE in UDS (see caption of Figure 2.4).

Legacy program (PI: M. Dickinson) and GOODS-H (Elbaz et al., 2011) for the ZFOURGE-CDFS field, S-COSMOS Spitzer Legacy program (PI: D. Sanders) and CANDELS-H (Inami et al. 2017, in prep) for the ZFOURGE-COSMOS field, and SpUDS *Spitzer* Legacy program (PI: J. Dunlop) and CANDELS-H for the ZFOURGE-UDS field. The median  $1\sigma$  flux uncertainties for each survey is  $\sim 10 \mu\text{Jy}$  in COSMOS and UDS, and  $3.9 \mu\text{Jy}$  in CDFS. Photometry from this data is produced using Multi-Resolution Object PHotometry oN Galaxy Observations (MOPHONGO) code written by I. Labbé (for further details, see Labbé et al., 2006; Fumagalli et al., 2014; Whitaker et al., 2014).

## 2.3 Multi-Wavelength AGN Selection

### 2.3.1 Host Galaxy Parameters

To reliably select AGN from our galaxy catalogues, we first need to determine several basic parameters, including the redshift, stellar mass, and star formation rate of each host galaxy. The photometric redshifts of galaxies in ZFOURGE are calculated using the public SED-fitting code, EAZY (Brammer et al., 2008). EAZY uses a default set of 5 templates generated from the PÉGASE library (Fioc & Rocca-Volmerange, 1997), plus an additional dust-reddened template from Maraston (2005). Linear combinations of these templates are fit

to the observed  $0.3 - 8 \mu\text{m}$  photometry for estimating redshifts. Stellar masses are calculated by fitting Bruzual & Charlot (2003) stellar population synthesis models using FAST (Kriek et al., 2009), assuming solar metallicity, a Calzetti et al. (2000) dust extinction law (with  $A_V = 0 - 4$ ), a Chabrier (2003) initial mass function (IMF) and exponentially declining star formation histories of the form  $\text{SFR}(t) \propto e^{-t/\tau}$ , where  $t$  is the time since the onset of star formation and  $\tau$  (varied over  $\log[\tau/\text{yr}] = 7 - 11$ ) modulates the declining function. SFRs are calculated by considering both the rest-frame UV emission from massive unobscured stars and the re-radiated IR emission from dust obscured stars. The combined UV and IR luminosities ( $L_{\text{UV}}$  and  $L_{\text{IR}}$ ) are then converted to SFRs ( $\Psi$ ) using the calibration from Bell et al. (2005), scaled to a Chabrier (2003) IMF:

$$\Psi_{\text{IR+UV}}[M_{\odot} \text{ yr}^{-1}] = 1.09 \times 10^{-10} (3.3L_{\text{UV}} + L_{\text{IR}}) \quad (2.1)$$

where  $L_{\text{UV}} = \nu L_{\nu, 2800}$  is an estimate of the integrated  $1216\text{-}3000 \text{ \AA}$  rest-frame UV luminosity, derived from EAZY, and  $L_{\text{IR}}$  is the bolometric  $8 - 1000 \mu\text{m}$  IR luminosity calculated from a luminosity-independent conversion (Wuyts et al., 2008, 2011) using PACS  $160 \mu\text{m}$  fluxes.

### 2.3.2 Reliability of AGN Photometric Redshifts

AGN emission is known to complicate the computation of photometric redshifts (e.g. MacDonald & Bernstein, 2010), which can ultimately impact the derivation of galaxy properties. To test the accuracy of our AGN sample, we compare the sample's photometric redshifts from ZFOURGE to a secure sample of publicly available spectroscopic redshifts sourced from the compilation of the 3D-HST (Skelton et al., 2014) and ZFIRE (Nanayakkara et al., 2016) surveys. We use the Normalised Median Absolute Deviation (NMAD) to calculate scatter:

$$\sigma_{\text{NMAD}} = 1.48 \times \text{median} \left( \frac{|\Delta z - \text{median}(\Delta z)|}{1 + z_{\text{spec}}} \right) \quad (2.2)$$

where  $\Delta z = z_{\text{phot}} - z_{\text{spec}}$ . From the 500 AGN hosts identified in ZFOURGE, we find 136 cross-matches with reliable spectroscopic redshifts. Figure 2.7 shows a relatively small number of AGN hosts with photometric redshifts very different from the spectroscopic value. These outliers (defined here to have  $|\Delta z| / (1 + z_{\text{spec}}) > 0.15$ ) make up 7.40% of our sample and are subsequently removed from the sample. Assuming the remainder of the AGN population has a similar outlier fraction, there is potential for an additional 27 AGN in our sample to have unreliable redshifts. Indeed, we visually inspect the SEDs of those AGN lacking a spectroscopic counterpart and manually eject 14 (3.85%) with questionable

fits. Following this, the accuracy of photometric redshifts for our AGN hosts is found to be  $\sigma_{\text{NMAD}} = 0.023$ , which is only slightly higher than the general ZFOURGE population ( $\sigma_{\text{NMAD}} = 0.018$ ; Tomczak et al. 2014).

The strong correspondence between the photometric and spectroscopic redshifts in ZFOURGE is attributed to the efficient way the ZFOURGE medium-band filters trace the 4000 Å/Balmer breaks, which is driven by stellar light. Despite this, it remains possible that rest-frame optical AGN emission can increase the uncertainty of the photometric redshifts. For obscured (i.e. Type-2) AGN, several studies have demonstrated contamination to host galaxy properties is negligible (Silverman et al., 2009; Schawinski et al., 2010; Xue et al., 2010). However, the AGN population in this work may also contain luminous, unobscured (i.e. Type-1) AGN, which may impact SED fits. To quantify how many of these might be in our sample, we search for objects (at all redshifts) with rest-frame  $UVJ$  colours  $\pm 0.5$  mag around a SWIRE Type-1 QSO template (Polletta et al., 2007). We find 23 sources ( $\sim 4\%$  of the parent AGN population) with these colours. A visual inspection of their SEDs reveals a sound fit to photometry, resulting in a photometric redshift with low fitting error. Given this, we retain these sources in the parent AGN population.

### 2.3.3 Radio AGN Selection

The accretion of material onto a supermassive black hole is known to produce nuclear radio emission, collimated into relativistic jets that propagate perpendicular to the plane of the accretion disc. While the detection of such radio-emitting jets unmistakably implies the presence of AGN, high brightness temperatures implied by very-long-baseline interferometry (VLBI) detections are also indicative of an AGN. However, if the radio detections are at redshifts beyond the observable jet structure or there is no VLBI detection, it is not possible to determine whether the radio emission comes from AGN or star formation. To overcome this limitation, we use the Radio-AGN Activity Index of Rees et al. (2016). Briefly, this takes advantage of the tight correlation observed between a galaxy’s radio (synchrotron) and IR (thermal) emissions (Helou et al., 1985), which Morić et al. (2010) found holds for a diverse range of galaxies over a broad redshift. The exception was radio AGN, which presented a discernible offset from the correlation. The Radio-AGN Activity Index, which operates in  $SFR$  space, exploits this offset by assuming  $SFR_{\text{RADIO}} = SFR_{\text{IR+UV}}$  if 100% of the radio emission originates from star formation. Sources with excess  $SFR_{\text{RADIO}}$  are considered dominated by AGN activity:

$$SFR_{\text{RADIO}}/SFR_{\text{IR+UV}} = \text{Radio AGN Activity Index} > 3 \quad (2.3)$$

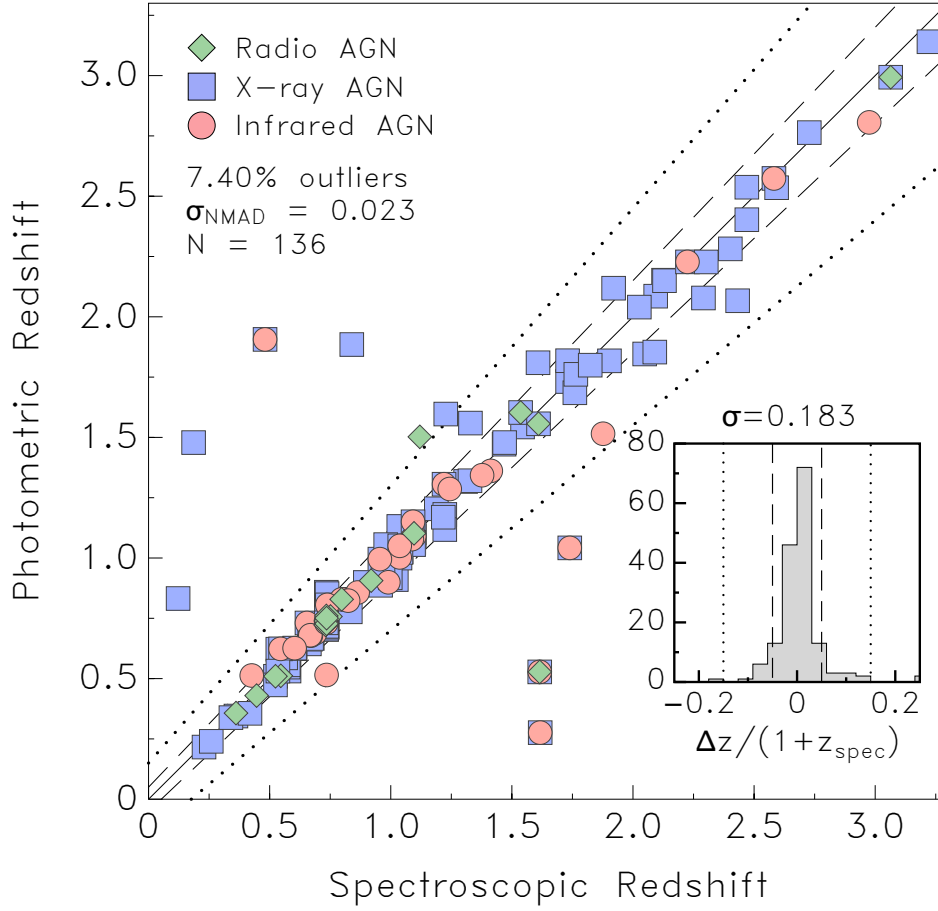


**Fig. 2.7** Comparison of photometric and spectroscopic redshifts for our radio (green diamonds), X-ray (blue squares) and IR (red circles) AGN hosts. The solid line is the  $z_{\text{phot}} = z_{\text{spec}}$  relation, the dashed lines are  $z_{\text{phot}} = 0.05 \pm (1 + z_{\text{spec}})$  and the dotted lines are  $z_{\text{phot}} = 0.15 \pm (1 + z_{\text{spec}})$ . AGN Hosts outside of the dotted lines are defined as outliers.

The inclusion of UV emission accounts for the possibility of radio star-forming galaxies with low dust, which would otherwise produce an excess in  $SFR_{\text{RAD}}$  and be misclassified as radio AGN. To calculate radio SFRs, we first make use of the cross-matched photometric redshifts from ZFOURGE and apply radio  $K$ -corrections to estimate rest-frame radio luminosities using:

$$L_{\text{RADIO}}[\text{W Hz}^{-1}] = 4\pi d_l^2 (1+z)^{-(\alpha+1)} f_{\text{RADIO}} \quad (2.4)$$

where  $d_l$  is the luminosity distance in cm,  $f_{\text{RAD}}$  is the observed radio flux in  $\text{W m}^{-2} \text{Hz}^{-1}$ , and  $\alpha$  is the radio spectral index<sup>1</sup>, which we fix to  $\alpha = -0.3$  as found in the Wuyts et al. (2008) average star-forming SED template. While this spectral index is flatter than the standard  $\alpha = -0.7$ , it is adopted to ensure consistency with the Wuyts et al. (2008) SED template, which is also used to derive IR SFRs. The difference between the two index values is one less source identified as a radio AGN under  $\alpha = -0.7$ .

Using the rest-frame radio luminosities, radio SFRs are then calculated using the calibration from Bell (2003), scaled to a Chabrier (2003) IMF:

$$\Psi_{\text{RADIO}}[M_{\odot} \text{ yr}^{-1}] = 3.18 \times 10^{-22} L_{\text{RADIO}} \quad (2.5)$$

As shown in Figure 2.8, the Radio-AGN Activity Index leads to the identification of 67 radio sources dominated by AGN activity in ZFOURGE, with 20 in CDFS, 32 in COSMOS, and 15 in UDS.

### 2.3.4 X-ray AGN Selection

Radio surveys pioneered the way for identifying AGN (e.g. Baade & Minkowski, 1954; Schmidt, 1963; Schmidt & Matthews, 1964) before it was realised that optical data, such as colours (e.g. Koo & Kron, 1988) and emission lines (e.g. Osmer & Hewett, 1991), could be used for selection. However, stellar contamination limits their use to low redshifts (e.g. Richards et al., 2001). The launch of *Chandra* and *XMM-Newton* heralded in a new era of sensitive, deep X-ray surveys, offering an effective alternative to select AGN over a broad redshift range. These surveys have found that X-ray emission from sources at high Galactic latitudes is predominantly AGN (e.g. Watson et al., 2001) and routinely outshine the highest star-forming galaxies ( $\sim 10^{42} \text{ erg s}^{-1}$ ; e.g. Moran et al., 1999; Lira et al., 2002). While this provides an excellent discriminator for AGN selection, heavy obscuration by dense

<sup>1</sup>The radio spectral index,  $\alpha$  is defined from  $S_{\nu} \propto \nu^{\alpha}$ , where  $S$  is the measured flux density and  $\nu$  is the observer's frame frequency



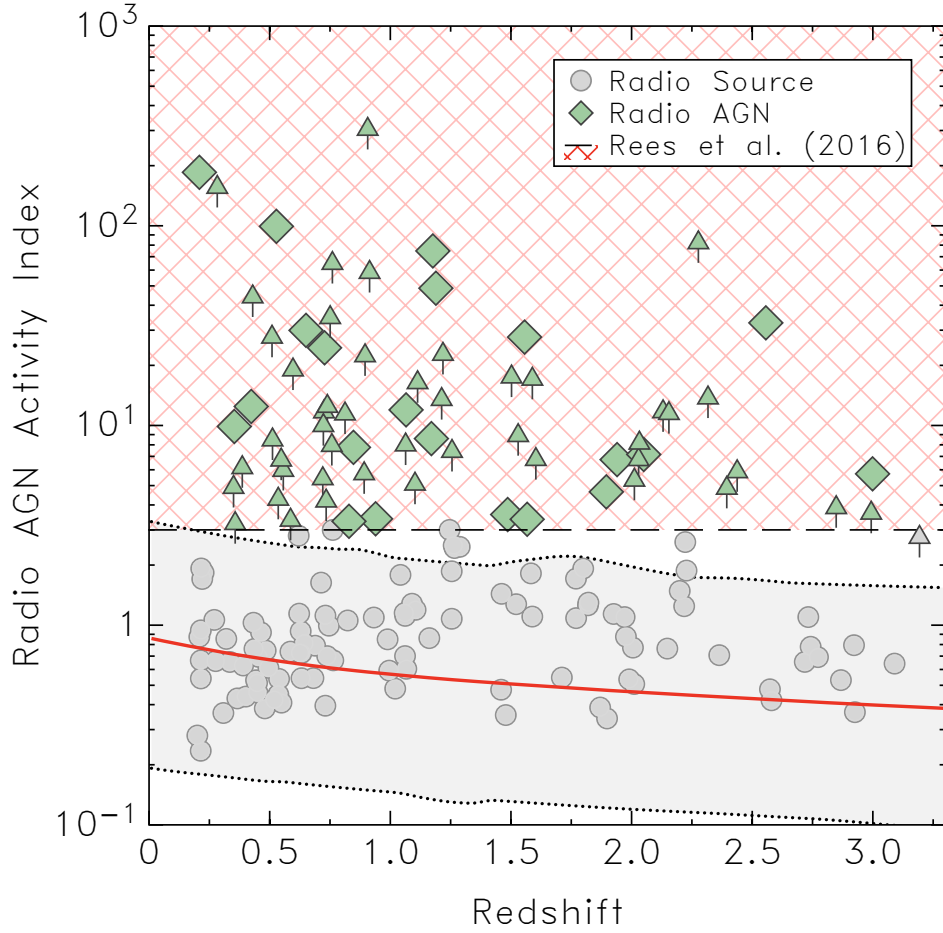


**Fig. 2.8** The Radio AGN Activity Index (see equation 4.1) for all radio sources in ZFOURGE. The evolution of the Wuyts et al. (2008) average star-forming SED template, calculated from  $160\ \mu\text{m}$  fluxes, is shown by the red line. The grey shaded region represents the  $3\sigma$   $0.39\ \text{dex}$  scatter found in the local radio-FIR correlation (Morić et al., 2010). Rees et al. (2016) adopt a conservative cut above this region ( $SFR_{\text{RAD}}/SFR_{\text{IR+UV}} > 3$ ; crosshatched region) to select radio AGN (green diamonds). Sources that lack a reliable ( $> 3\sigma$ )  $160\ \mu\text{m}$  detection are given  $3\sigma$  limits (arrows).

circumnuclear gas can prove problematic. One way to account for this is by examining the hardness ratio (HR) of a source, which is defined as the normalised difference of counts in the soft and hard X-ray bands,  $(\text{hard} - \text{soft})/(\text{hard} + \text{soft})$ . The HR allows an estimate of absorption in the X-ray band, where obscured AGN are expected to exhibit a harder spectrum than unobscured AGN due to the absorption of soft X-rays by obscuring gas (Szokoly et al., 2004). Considering this, we select X-ray AGN using both the X-ray luminosity and HR of a source.

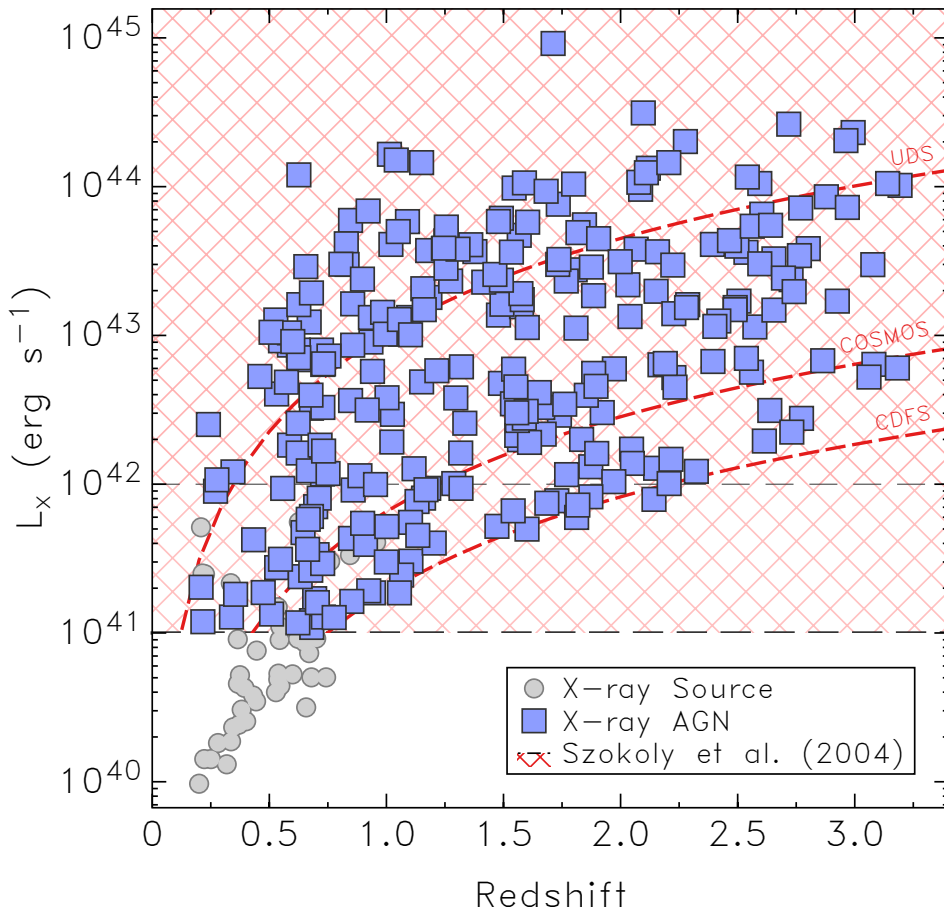


**Fig. 2.9** X-ray rest-frame luminosity as a function of redshift for all X-ray sources in ZFOURGE. All sources above  $10^{42} \text{ ergs s}^{-1}$  (upper crosshatched region; Szokoly et al. 2004) are identified as AGN (blue squares), while only sources with a HR  $> -0.2$  down to  $10^{41} \text{ ergs s}^{-1}$  (lower crosshatched region; Szokoly et al. 2004) are identified as AGN. The approximate luminosity limits for each field are indicated by the red dashed curves.

We first start with the cross-matched photometric redshifts from ZFOURGE and apply X-ray  $K$ -corrections to estimate rest-frame luminosities using:

$$L_X[\text{erg s}^{-1}] = 4\pi d_l^2 (1+z)^{\Gamma-2} f_x \quad (2.6)$$

where  $d_l$  is the luminosity distance in cm,  $f_x$  is the observed X-ray flux in  $\text{erg cm}^{-2} \text{s}^{-1}$ , and  $\Gamma$  is the photon index of the X-ray spectrum, which was fixed to a typical galaxy photon index<sup>2</sup> of  $\Gamma = 1.4$ . For sources in the X11 catalogue, the intrinsic flux is derived from counts in the 0.5-8 keV full band, while for the E09 and U08 catalogues it is derived from the sum of the counts in the relevant bands over 0.5-10 keV. We adjusted flux values calculated in the E09 and U08 catalogues to align with the full bandpass values of the X11 catalogues (0.5-10  $\rightarrow$  0.5-8 keV) assuming a power-law model of  $\Gamma = 1.4$  (i.e. E09 and U08 fluxes are multiplied by a factor of 0.95). We then use the selection technique of Szokoly et al. (2004) to select X-ray AGN:

$$\begin{aligned} L_X &\geq 10^{41} \text{erg s}^{-1} \text{ \& HR} > -0.2 \\ L_X &\geq 10^{42} \text{erg s}^{-1} \text{ \& HR} \leq -0.2 \end{aligned} \quad (2.7)$$

The luminosity threshold is lower for sources with a stronger HR on account of substantial absorption. In the absence of a HR measurement, we only select sources with  $L_x \geq 10^{42} \text{erg s}^{-1}$ . As shown in Figure 2.9, this approach leads to the identification of 270 X-ray sources dominated by AGN activity in ZFOURGE, with 187 in CDFS, 57 in COSMOS, and 26 in UDS.

### 2.3.5 Infrared AGN Selection

Despite the efficiency of AGN selection in X-ray surveys, an imbalance in the cosmic X-ray background budget suggests an additional population of heavily obscured AGN are being missed (Comastri et al., 1995; Gilli et al., 2001, 2007). IR observations offer an effective way to identify these AGN by virtue of dust radiating the reprocessed nuclear emission in the mid-IR regime (Sanders et al., 1988, 1989). Such emission is evident by the changing shape of a galaxy's SED, where an increase in AGN activity also leads to a dilution in the strength of Polycyclic Aromatic Hydrocarbon (PAH) emissions features formed by ultraviolet excitation typical in star-forming regions (Brandl et al., 2006). The mid-IR is then dominated by the thermal continuum (e.g. Neugebauer et al., 1979; Heisler & De Robertis, 1999).

<sup>2</sup>The photon index,  $\Gamma$  is related to the number of photons as a function of energy  $\mathcal{E}$ ,  $dN(\mathcal{E})/d\mathcal{E} \propto \mathcal{E}^{-\Gamma}$

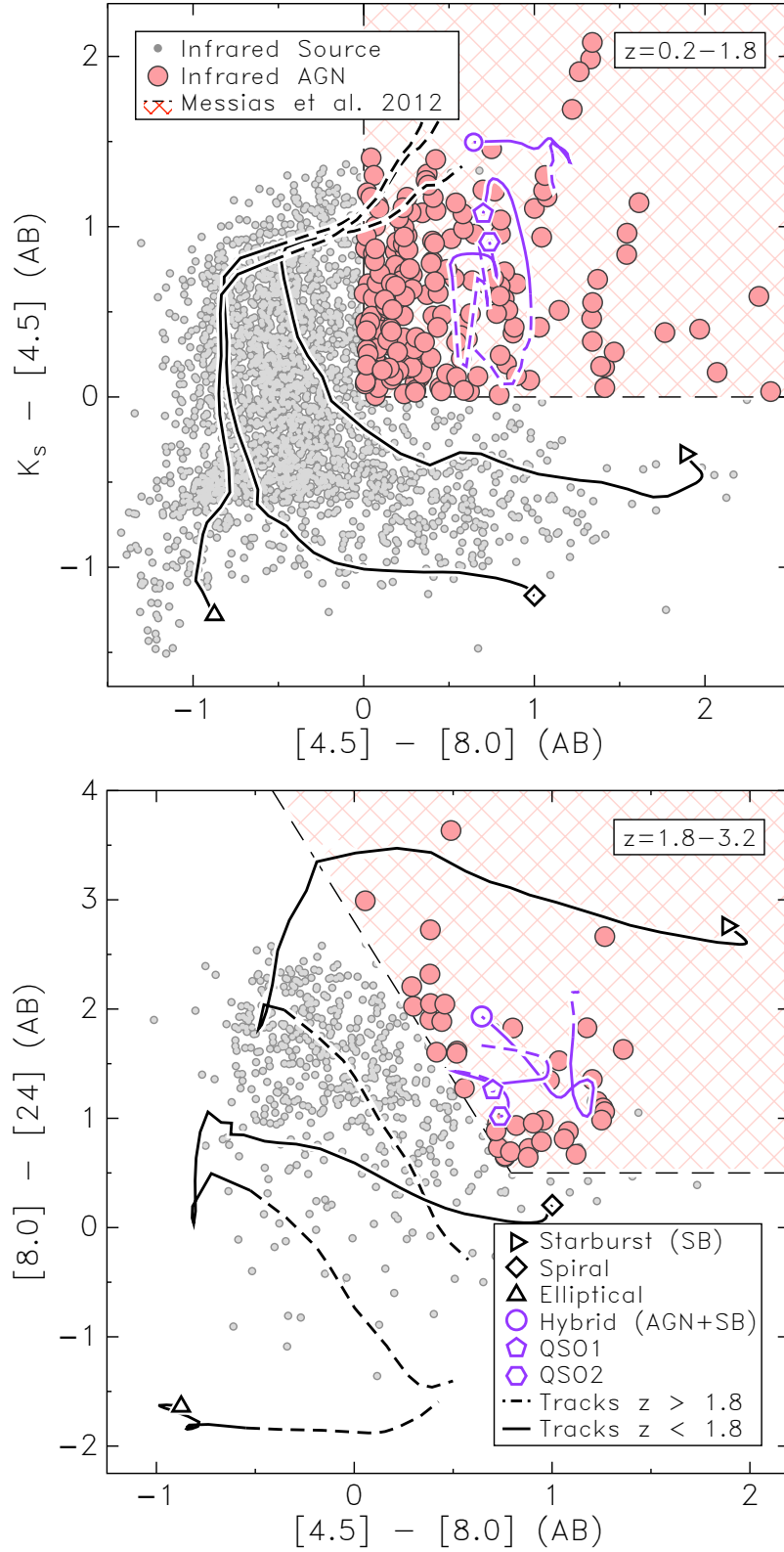


**Fig. 2.10** The Messias et al. (2012) KI (top) and KIM (bottom) infrared colour-colour space for all IR sources within ZFOURGE. Sources that fall within the cross-hatched regions are considered AGN dominated (red circles). Overplotted are the redshift-dependent spectral tracks for a selection of active (hybrid, QSO1 and QSO2) and inactive (starburst, spiral and elliptical) galaxies from the Swire Templates (Polletta et al., 2007). The dashed portion of the tracks represents  $z = 0 - 1.8$  and the solid portion  $z = 1.8 - 4$ .

A number of IRAC colour-colour diagnostics have been designed to select AGN by taking advantage of this process (e.g. Lacy et al., 2006; Stern et al., 2005; Donley et al., 2012). The choice of diagnostic depends on the science being conducted as each has a particular level of completeness and reliability, with one often dominating in favour of the other (e.g. Barmby et al., 2006; Donley et al., 2007; Messias et al., 2012). Unfortunately, with increasing redshift, the IRAC bands begin to probe shorter rest-frame wavelengths and eventually trace the 1.6  $\mu\text{m}$  stellar bump of a galaxy's SED, which can mimic the AGN thermal continuum. As a result, diagnostics limited to IRAC colours become ineffective at  $z \gtrsim 2.5$  and rapidly introduce contaminants into the selection. Messias et al. (2012) investigated this and found by extending the use of IRAC to additional wavebands, they could reliably select AGN over a broader redshift range. Specifically, the authors proposed two colour diagnostics,  $K_s + \text{IRAC}$  at lower redshifts ( $z = 0 - 2.5$ ) and  $\text{IRAC} + 24 \mu\text{m}$  at higher redshifts ( $z = 1 - 4$ ). We adopt these diagnostics, with the added condition sources have a  $5\sigma$  detection limit in all relevant bands to reduce scatter, and select IR AGN based on the following constraints:

$$z < 1.8 \begin{cases} K_s - [4.5] > 0 \\ [4.5] - [8.0] > 0 \end{cases} \quad (2.8)$$

$$z > 1.8 \begin{cases} [8.0] - [24] > 2.9 \times ([4.5] - [8.0]) + 2.8 \\ [8.0] - [24] > 0.5 \end{cases} \quad (2.9)$$

As shown in Figure 2.10, this approach leads to the identification of 234 IR sources dominated by AGN activity in ZFOURGE, with 66 in CDFS, 50 in COSMOS, and 118 in UDS.

## 2.4 Summary

We illustrate the relative size and overlap between the AGN samples in Figure 2.11 (top panel). Overlap arises from the complex and broad emission of AGN spectra and emphasises that our samples are not wholly independent and not simply relegated to either a radio, X-ray or IR selection bin. Despite this, the relative size of the overlap is comparable to previous studies that have performed multi-wavelength AGN selection (Hickox et al., 2009; Juneau et al., 2013). Like these studies, we find the overlap between radio and X-ray, and radio and IR AGN are low, while the overlap between IR and X-ray AGN hosts is significantly

larger. Of the 500 AGN identified, 54 are found to overlap in one or more wavebands, with 5 identified in all three. We summarise the columns of the complete AGN dataset in Table A.1, which provides all host galaxy parameters used to select AGN in ZFOURGE. This dataset acts as a complementary catalogue to the primary ZFOURGE catalogues and is used throughout the remainder of this work.

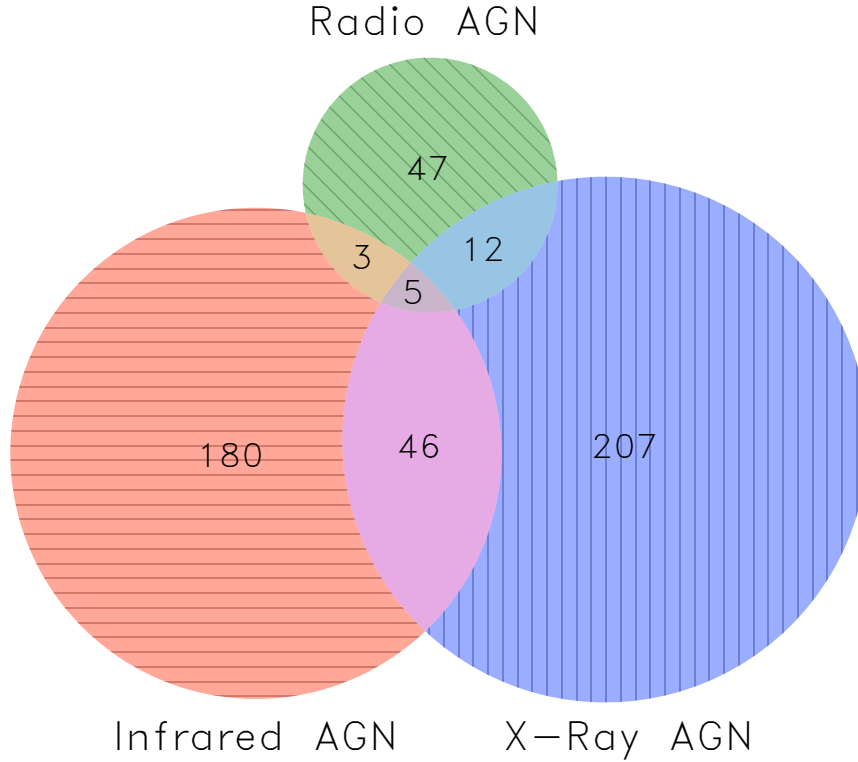


**Fig. 2.11** Venn diagram displaying the relative number of AGN identified in radio (green), X-ray (blue) and IR (red) wavebands. The overlapping regions between samples correspond to the relative numbers selected in multiple wavebands. Note that these numbers correspond to the complete AGN candidate catalogue detailed in Section 2.3.

# Chapter 3

## An Enhancement of Star Formation in AGN Hosts

Portions of this chapter and chapter 2 are based on a single paper, which appears in *Monthly Notices of the Royal Astronomical Society*, 2016, Volume 457, 629-641. The co-authors are L. Spitler, K-V. Tran, G. Rees, I. Labbé, R. Allen, G. Brammer, K. Glazebrook, A. Hopkins, S. Juneau, G. Kacprzak, J. Mullaney, T. Nanayakkara, C. Papovich, R. Quadri, C. Straatman, A. Tomczak, and P. van Dokkum. L. Spitler, K-V. Tran, and I. Labbé supervised this work and provided guidance with respect to the methodology and scientific interpretation, G. Rees provided guidance with respect to the methodology of radio data analysis, and the remaining co-authors provided discussion and feedback towards the final manuscript. The candidate's contribution to the work presented in this paper is 95%.

### 3.1 Introduction

There is mounting evidence demonstrating that SMBHs play a fundamental role in the formation and evolution of galaxies over cosmic time. Previous work has found the mass of a SMBH is tightly correlated with various properties of its host's hot spheroidal bulge, including its luminosity (e.g. Kormendy & Richstone, 1995; Graham, 2007; Sani et al., 2011) mass (e.g. Magorrian et al., 1998; Marconi & Hunt, 2003; Beifiori et al., 2011) and velocity dispersion (e.g. Gebhardt et al., 2000; Gültekin et al., 2009; Graham et al., 2011). During periods of rapid accretion, the galactic nuclei of these systems can also release an immense amount of energy into the surrounding environment of the host galaxy (e.g. Kormendy & Richstone, 1995; Magorrian et al., 1998). As a result, theoretical simulations commonly invoke feedback from these AGN outflows to regulate the star formation activity of galaxies

(e.g. Ciotti & Ostriker, 1997; Silk & Rees, 1998; Croton et al., 2006). The inclusion of a negative feedback mechanism helps resolve the overproduction of massive galaxies in simulations by heating or driving out gas to suppress star formation. While observational evidence supports negative feedback via AGN-driven outflows (e.g. Nesvadba et al., 2006; Feruglio et al., 2010; Fischer et al., 2010), recent studies also point to the possibility of AGN producing positive feedback, whereby AGN outflows trigger star formation by compressing cold, dense gas. (e.g. Silk & Norman, 2009; Elbaz et al., 2009; Zinn et al., 2013).

To reconcile these contradictory outcomes, the complex interplay between AGN activity and star formation must be examined. Early studies, which tried to achieve this, relied on optical spectra to select AGN from large parent samples of galaxies. The main drawback of this approach was the restriction of low redshifts ( $z < 0.3$ ; Ho, 2005; Kim et al., 2006; Salim et al., 2007). With cosmic AGN activity peaking at a similar epoch to cosmic star formation ( $z \sim 2$ ), these studies potentially miss a key phase of AGN evolution.

More recent studies have pushed to higher redshifts by taking advantage of X-ray emission, which is an effective probe of AGN activity. Upon comparing X-ray AGN hosts to mass-matched reference galaxies, these studies yield results suggesting only minor or no difference in star formation activity between the two samples (Xue et al., 2010; Santini et al., 2012; Mullaney et al., 2012a; Rosario et al., 2014). However, by relying on X-ray selected AGN, these studies may also miss a key phase when AGN are hosted in dust-rich, X-ray obscured galaxies (Sanders et al., 1988). For the work presented here, we expand on these studies by investigating the empirical connection between AGN activity and star formation by selecting and analysing a diverse sample of AGN across a broad range of obscuration levels over  $z = 0.2 - 3.2$ . Our parent sample is the deep  $K_s$ -band imaging of ZFOURGE (Straatman et al., 2016), which not only grants us access to all galaxy types, but also allows us to probe to lower stellar masses and higher redshifts.

As detailed in Chapter 2, AGN are selected by cross-matching the  $K_s$ -band imaging of ZFOURGE to radio, X-ray and IR datasets to allow the use of standard AGN selection techniques. We make use of rest-frame  $U - V$  versus  $V - J$  ( $UVJ$ ) colours from the ZFOURGE catalogues to distinguish quiescent galaxies from star-forming galaxies. To gauge star formation activity, we employ deep FIR data (160  $\mu\text{m}$ ) from the *Herschel Space Observatory*. Our principal aim is to compare AGN hosts with a mass-matched sample of inactive galaxies, before discussing the implications of our results for understanding the connection between star formation and AGN activity, as well as the impact AGN has on galaxy evolution.



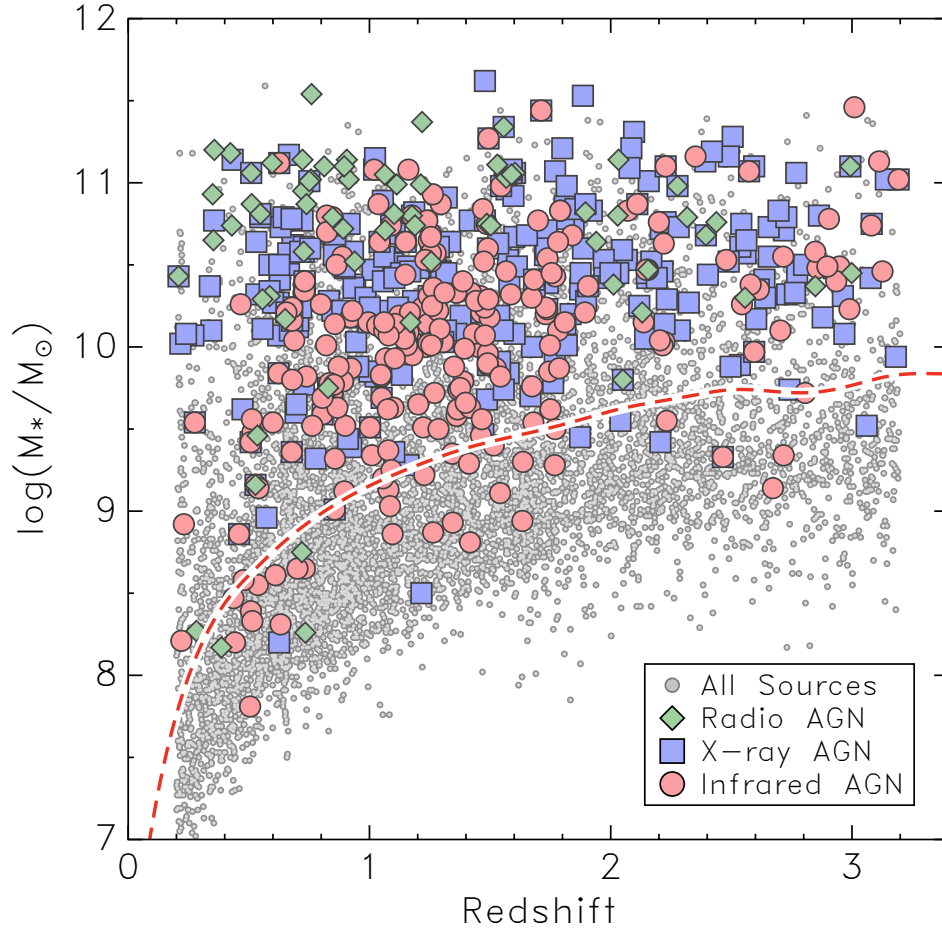


**Fig. 3.1** Stellar mass as a function of redshift for our radio (green diamonds), X-ray (blue squares) and IR (red circles) AGN hosts, along with the parent sample from ZFOURGE (grey circles). The red dotted line in the stellar mass plot represents the 80% mass-completeness limit in ZFOURGE. For clarity, only  $1/3^{\text{rd}}$  of the parent sample is plotted.

## 3.2 Mass-Limited Sample

In this section, we extract AGN hosts from the catalogue of candidates selected in Chapter 2 with the goal of constructing a mass-matched, inactive sample of galaxies (control sample) to compare star formation activity between AGN hosts and inactive galaxies. Selection is based on redshift, stellar mass and luminosity limits, with the goal of minimising bias on host galaxy properties. Given the shallow X-ray and radio data used to select AGN hosts in ZFOURGE-UDS, this field will be excluded from the comparative analysis.

### 3.2.1 Redshift, Mass and Luminosity Cuts

To overcome the potential bias associated with  $K_s$ -band selected galaxies, we limit our sample of AGN hosts to a stellar-mass cut of  $\log(M_*/M_\odot) \geq 9.75$ , which sits above the 80% completeness limit of ZFOURGE (Papovich et al., 2015), as shown in Figure 3.1 (top-left panel). We apply further restrictions by splitting the AGN sample into three redshift bins of  $z = [0.2 - 0.8]$ ,  $[0.8 - 1.8]$ ,  $[1.8 - 3.2]$ , each with varying luminosity limits based on the luminosity thresholds of their respective wavebands (i.e.  $L_{1.4\text{GHz}}$ ,  $L_X$  and  $L_{\text{IR}}$ ). These limits are summarised in Table 3.1, and while they reduce AGN numbers and restrict comparison across redshifts, they minimise potential luminosity biases by ensuring a consistent luminosity-completeness within each redshift bin.

**Table 3.1** Luminosity limits of mass-limited AGN sample

Waveband	$L_{1.4\text{GHz}}$ (W Hz <sup>-1</sup> )	$L_X$ (erg s <sup>-1</sup> )	$L_{\text{IR}}^1$ (erg s <sup>-1</sup> )	$z_{\text{min}}$	$z_{\text{max}}$	$N_{\text{AGN}}^2$
Radio	$1.0 \times 10^{23}$	-	-	0.2	0.8	10
	$6.0 \times 10^{23}$	-	-	0.8	1.8	11
	$1.9 \times 10^{24}$	-	-	1.8	3.2	5
X-ray	-	$4.0 \times 10^{41}$	-	0.2	0.8	31
	-	$2.0 \times 10^{42}$	-	0.8	1.8	60
	-	$7.0 \times 10^{42}$	-	1.8	3.2	50
Infrared	-	-	$6.0 \times 10^{27}$	0.2	0.8	7
	-	-	$3.0 \times 10^{28}$	0.8	1.8	39
	-	-	$1.0 \times 10^{27}$	1.8	3.2	22

<sup>1</sup>  $L_{\text{IR}} = L_{8\mu\text{m}}$  at  $z = 0.2 - 1.8$  and  $L_{24\mu\text{m}}$  at  $z = 1.8 - 3.2$

<sup>2</sup> Number of AGN hosts within the specified limits

### 3.2.2 Control Sample of Inactive Galaxies

Tight correlations exist between the physical properties of galaxies and their stellar mass (e.g. Tremonti et al., 2004, mass-metallicity and Noeske et al., 2007, mass-star formation rate). This makes constructing a mass-matched control sample of inactive galaxies an essential component for our comparative analysis. Without this consideration, even a mass-limited sample would be dominated by galaxies just above the mass threshold, potentially biasing any comparison. We construct our mass-matched control sample by binning inactive galaxies into narrow mass intervals of  $\Delta M_* = 0.2$  dex.

For each AGN host, we randomly select an inactive galaxy from the same redshift bin ( $z = [0.2 - 0.8]$ ,  $[0.8 - 1.8]$  or  $[1.8 - 3.2]$ ) and of similar mass, within  $\Delta M_*$ . For example, a  $z = 0.74$  radio AGN host with  $\log(M_*/M_\odot) = 10.87$  has 112 inactive analogues from which to draw from. We then record a value for various physical properties of the selected control inactive galaxy (i.e. rest-frame colour, stellar mass and star formation rate) and repeat for the next AGN host until we have a control sample with the same number of galaxies as the AGN sample being considered. We generate 100 such independent control samples, which we use to compute a final mean control value for each physical property. The distribution of various physical properties for the mass-limited sample of AGN and control sample of inactive galaxies is shown in Figure 3.2.

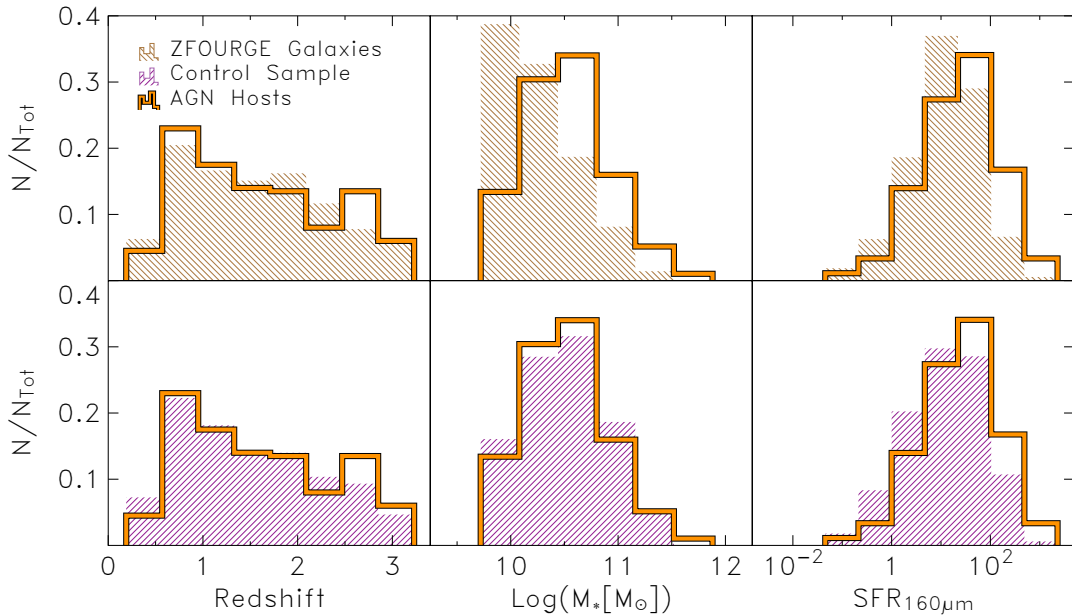


**Fig. 3.2** The redshift (left), stellar mass (middle) and SFR (right, limited to positive fluxes) distributions for the parent population of galaxies (top row, hatched), control sample of inactive galaxies (bottom row, hatched), and luminosity limited AGN hosts (solid orange line) in ZFOURGE.

### 3.3 Results

#### 3.3.1 Comparison of Rest-frame Colours

Examining the rest-frame  $UVJ$  colours of galaxies has become a common approach to distinguish a quiescent population from a star-forming one, including those exhibiting heavy extinction (e.g. Labbé et al., 2005; Wuyts et al., 2007; Williams et al., 2009). Referring to the top panel in Figure 3.3, quiescent galaxies occupy the upper left region, delimited by the vertices  $(V - J, U - V) = (-\infty, 1.3), (0.85, 1.3), (1.6, 1.95), (1.6, +\infty)$ , while the vertical dashed-line ( $V - J = 1.2$ ) separates non-dusty (lower left) from dusty star-forming galaxies (Spitler et al., 2014).

Within this figure, we examine the  $UVJ$  colour space of our mass-limited AGN hosts and control sample of inactive galaxies. In the lowest redshift bin ( $z = 0.2 - 0.8$ ), we find the  $UVJ$  colours of each subsample of AGN, identified in radio, X-ray or IR, to be consistent with a distinct galaxy population. IR AGN are found exclusively in star-forming galaxies, radio AGN in quiescent galaxies, and X-ray AGN in both quiescent ( $29.0\% \pm 8.2\%$ ) and star-forming hosts. However, at higher redshifts ( $z > 0.8$ ), the trend weakens and the distribution of  $UVJ$  colours scatter to the point where AGN are predominantly found in the colour space of star-forming hosts (radio AGN;  $57.1\% \pm 13.2\%$ , X-ray AGN;  $79.0\% \pm 4.1\%$ , IR AGN;  $91.2\% \pm 3.8\%$ ), mirroring the behaviour of the control sample of galaxies.

When comparing the distribution of  $UVJ$  colours between AGN hosts and the control sample, the two are found to be qualitatively similar at all redshifts, with slight differences in the peak of their distributions. To accentuate these differences and examine their impact, we compare the quiescent fraction ( $f_q = N_q / (N_q + N_{sf})$ ) and dusty star-former fraction ( $f_{dusty} = N_{sf(dusty)} / N_{sf(all)}$ ) of both samples in Figure 3.3 (lower panels). While low numbers in the radio AGN population hinder the ability to produce statistically significant results, offsets are observed between the IR and X-ray AGN hosts and their respective control samples. For both populations over all redshifts, the dusty fraction is found to be slightly elevated over the control samples, while the quiescent fraction is lower.

Together, all panels in Figure 3.3 reveal no significant differences between the  $UVJ$  colours of our AGN and control samples, with the exception that the AGN hosts tend to be dustier and hosted in a lower fraction of quiescent galaxies. In the following section, we explore these results in further detail by quantitatively gauging the difference in star formation activity between both samples.

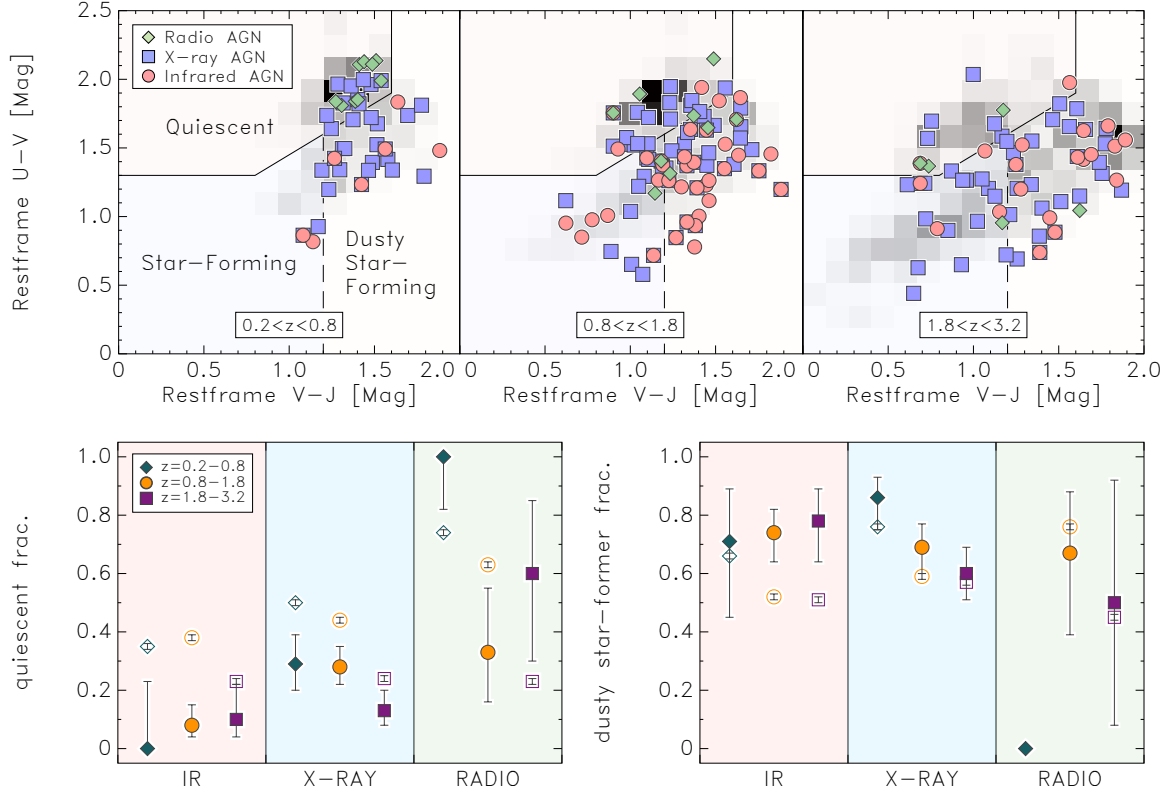


**Fig. 3.3** (Top) The rest-frame  $UVJ$  colour classification of galaxies in bins of redshift ( $z = 0.2 - 0.8$ ; left,  $z = 0.8 - 1.8$ ; middle and  $z = 1.8 - 3.2$ ; right). The points represent the mass-limited ( $\log(M_*/M_\odot) \geq 9.75$ ) AGN hosts selected via radio (green diamonds), X-ray (blue squares) and IR (red circles) techniques. A representation of the control sample is shown by the grey-scale density plot in each panel. The solid line divides the population into quiescent and star-forming hosts, while the dashed line further divides the star-forming population into dusty and non-dusty galaxies. (Lower-left) The quiescent fraction ( $N_q/(N_q + N_{sf})$ ) and (lower-right) dusty star-former fraction ( $N_{sf(dusty)}/N_{sf(all)}$ ) for the mass-limited AGN hosts (closed markers) and the control sample (open markers) at  $z = 0.2 - 0.8$  (diamond markers),  $z = 0.8 - 1.8$  (circle markers) and  $z = 1.8 - 3.2$  (square markers). Values are derived from the  $UVJ$  colour classification. Vertical error bars indicate the  $1\sigma$  Clopper-Pearson confidence intervals. Unless shown, error bars are smaller than the plotting symbols for the control sample.

### 3.3.2 Comparison of Star Formation Activity

We now focus on the star formation activity in our mass-limited AGN hosts and how they compare to the control sample of inactive galaxies. We use specific star formation rate (sSFR) as a measure of the relative strength of star formation activity, which is a galaxy's SFR normalised by the mass of its stars ( $\Psi_{\text{IR+UV}}/M_*$ ). In Figure 3.4, we show the mean sSFR against stellar mass for our AGN hosts and control sample in bins of redshift. The mean sSFR is found to decrease with increasing stellar mass for all sources, with slight offsets observed between the AGN hosts and control sample. AGN hosts exhibit an elevation over the control sample, with an average logarithmic offset (linear average of the difference between the logarithmic sSFRs) for the combined mass bins of  $0.26 \pm 0.14$  dex at  $z = 0.2 - 0.8$ ,  $0.37 \pm 0.10$  dex at  $z = 0.8 - 1.8$ , and  $0.38 \pm 0.10$  dex at  $z = 1.8 - 3.2$  (see Table 3.2 for more details).

To better understand the source of this offset, we split the AGN population by detection technique (i.e. radio, X-ray and infrared). In Figure 3.5, the mean sSFR of each subsample of AGN hosts, along with their respective control sample is shown. It can be seen that each subsample exhibits an elevated level of sSFR over their control samples, with the exception of low redshift radio AGN hosts. For each subsample, the elevation is found to increase with redshift. This elevation is found to be consistently high and significant for IR AGN ( $0.48 \pm 0.21$  dex;  $z = 0.2 - 0.8$ ,  $0.50 \pm 0.12$  dex;  $z = 0.8 - 1.8$ ,  $0.72 \pm 0.13$  dex;  $z = 1.8 - 3.2$ ), but lower and insignificant for X-ray AGN ( $0.15 \pm 0.13$  dex;  $z = 0.2 - 0.8$ ,  $0.21 \pm 0.13$  dex;  $z = 0.8 - 1.8$ ,  $0.25 \pm 0.16$  dex;  $z = 1.8 - 3.2$ ). While high redshift radio AGN hosts ( $z > 0.8$ ) also present an elevated sSFR over the control sample, low number statistics impact its significance ( $-0.53 \pm 0.20$  dex;  $z = 0.2 - 0.8$ ,  $0.57 \pm 0.20$  dex;  $z = 0.8 - 1.8$ ,  $0.55 \pm 0.32$  dex;  $z = 1.8 - 3.2$  (see Table 3.3 for more details).

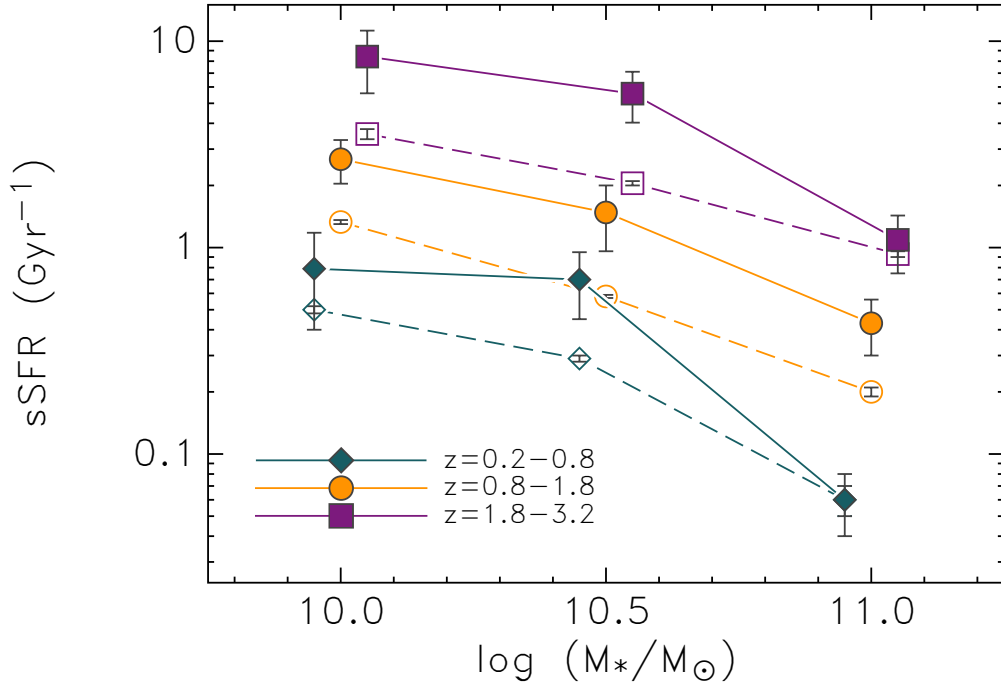


**Fig. 3.4** The mean specific star formation rate ( $\text{SFR}/M_*$ ) as a function of stellar mass for the mass-limited ( $\log(M_*/M_\odot) \geq 9.75$ ) AGN hosts (solid lines) and the control sample (dashed lines) at  $z = 0.2 - 0.8$  (diamond markers),  $z = 0.8 - 1.8$  (circle markers) and  $z = 1.8 - 3.2$  (square markers). Error bars indicate the 68% confidence intervals evaluated from a bootstrap analysis. Unless shown, error bars are smaller than the plotting symbols for the control sample. The stellar mass of markers are offset for better visibility. With the exception of the highest mass bins at low and high redshifts, AGN hosts show an elevated level of star formation activity with respect to the control sample of inactive galaxies.

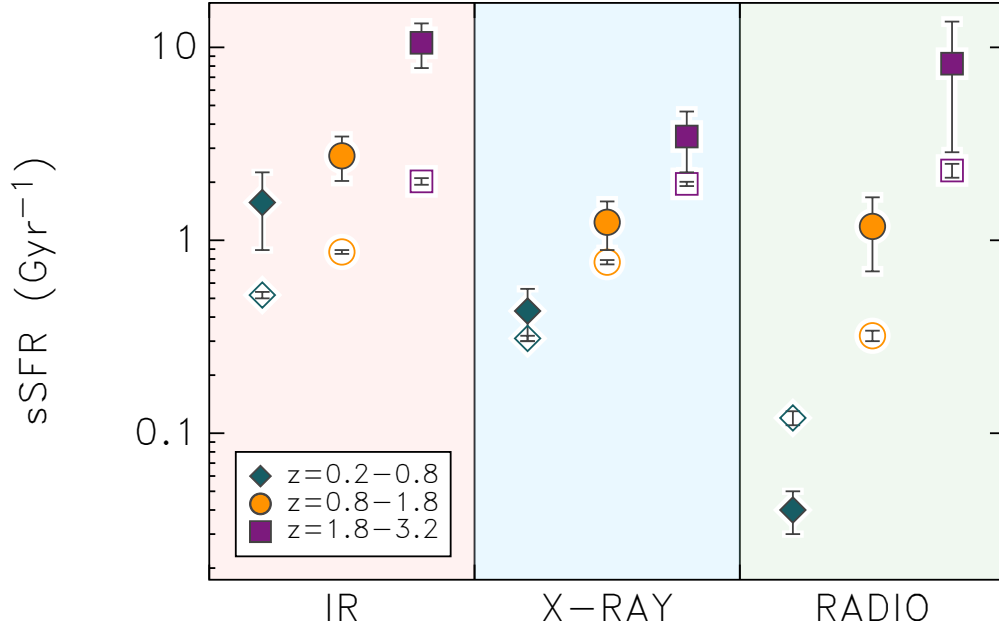


**Fig. 3.5** The mean specific star formation rate, split by AGN class (IR, X-ray and radio) for the mass-limited ( $\log(M_*/M_\odot) \geq 9.75$ ) AGN hosts (closed markers) and the control sample (open markers) at  $z = 0.2 - 0.8$  (diamond markers),  $z = 0.8 - 1.8$  (circle markers) and  $z = 1.8 - 3.2$  (square markers). Error bars indicate the 68% confidence intervals evaluated from a bootstrap analysis. Unless shown, error bars are smaller than the plotting symbols for the control sample. With the exception of low redshift Radio AGN, all AGN hosts show an elevated level of star formation activity, at all redshifts, with respect to their control sample of inactive galaxies.



**Table 3.2** Mean sSFR ( $\text{Gyr}^{-1}$ ) values by redshift bin (rows) for AGN hosts and the control in bins of stellar mass (cols)

Redshift	AGN Hosts				Control Sample			
	$10^{9.75-10.25} M_{\odot}$	$10^{10.25-10.75} M_{\odot}$	$10^{10.75-11.25} M_{\odot}$	$10^{10.75-10.25} M_{\odot}$	$10^{10.25-10.75} M_{\odot}$	$10^{10.75-11.25} M_{\odot}$		
$z = 0.2 - 0.8$	$0.79 \pm 0.39$ $\sigma = 0.19$	$0.70 \pm 0.25$ $\sigma = 0.21$	$0.06 \pm 0.02$ $\sigma = 0.01$	$0.50 \pm 0.02$ $\sigma = 0.11$	$0.29 \pm 0.01$ $\sigma = 0.06$	$0.06 \pm 0.01$ $\sigma = 0.02$		
$z = 0.8 - 1.5$	$2.68 \pm 0.64$ $\sigma = 1.39$	$1.48 \pm 0.52$ $\sigma = 0.60$	$0.43 \pm 0.13$ $\sigma = 0.14$	$1.33 \pm 0.03$ $\sigma = 0.28$	$0.58 \pm 0.01$ $\sigma = 0.09$	$0.20 \pm 0.01$ $\sigma = 0.05$		
$z = 1.5 - 2.5$	$8.42 \pm 2.83$ $\sigma = 2.52$	$5.57 \pm 1.54$ $\sigma = 2.40$	$1.09 \pm 0.34$ $\sigma = 0.49$	$3.55 \pm 0.20$ $\sigma = 1.16$	$2.05 \pm 0.05$ $\sigma = 0.39$	$0.93 \pm 0.03$ $\sigma = 0.19$		

**Notes.** Uncertainties are from a bootstrap analysis. Dispersions around the mean ( $\sigma$ ) on quantities are median absolute deviations (MAD).

**Table 3.3** Mean sSFR ( $\text{Gyr}^{-1}$ ) values by redshift bin (rows) for IR, X-ray and radio AGN hosts and their respective control samples (cols)

Redshift	AGN Hosts				Control Sample			
	IR Active	X-ray Active	Radio Active	IR inactive	X-ray inactive	Radio inactive		
$z = 0.2 - 0.8$	$1.57 \pm 0.68$ $\sigma = 0.19$	$0.43 \pm 0.12$ $\sigma = 0.14$	$0.04 \pm 0.01$ $\sigma = 0.01$	$0.52 \pm 0.02$ $\sigma = 0.16$	$0.31 \pm 0.01$ $\sigma = 0.05$	$0.12 \pm 0.01$ $\sigma = 0.05$		
$z = 0.8 - 1.5$	$2.74 \pm 0.64$ $\sigma = 1.18$	$1.24 \pm 0.34$ $\sigma = 0.40$	$1.18 \pm 0.49$ $\sigma = 0.39$	$0.87 \pm 0.02$ $\sigma = 0.15$	$0.77 \pm 0.02$ $\sigma = 0.10$	$0.32 \pm 0.01$ $\sigma = 0.10$		
$z = 1.5 - 2.5$	$10.56 \pm 2.75$ $\sigma = 3.15$	$3.45 \pm 1.20$ $\sigma = 1.04$	$8.23 \pm 5.37$ $\sigma = 2.48$	$2.02 \pm 0.08$ $\sigma = 0.52$	$1.96 \pm 0.05$ $\sigma = 0.36$	$2.30 \pm 0.19$ $\sigma = 1.02$		

**Notes.** Uncertainties are from a bootstrap analysis. Dispersions around the mean ( $\sigma$ ) on quantities are median absolute deviations (MAD).

### 3.3.3 AGN Contamination

We acknowledge potential contamination from AGN and adopt various tests to check for the effects on derived galaxy properties when presenting our results. The first is our SFRs, which are derived from a combination of UV and IR luminosities and may contain a mixed contribution of light from stars and AGN. We first examine the impact to the UV by removing the UV contribution to the SFRs of the AGN sample and recalculating our results. We find the offsets increase an average of 0.01 dex in each redshift bin, suggesting there is negligible impact from AGN contamination in the UV regime. If we assume contamination to the IR regime wholly explains the elevation of star formation activity observed in our AGN sample, the contribution from AGN emission would need to be in excess of  $\sim 25\%$ . However, the FIR regime is thought to be mostly immune to the effects of AGN (e.g. Netzer et al., 2007; Mullaney et al., 2012a), which is the primary motivation for employing PACs-based SFRs.

The other potential impact is AGN contamination to stellar masses. Ciesla et al. (2015) inspected this by omitting an AGN component while performing SED fitting on a range of Type-I, intermediate type, and Type-II AGN and comparing the measured stellar mass to the true value. Their results showed contamination from a Type-I AGN can lead to an overestimation in mass by as much as 150%. The contamination from intermediate and Type-II, believed to dominate the sample in this study, was overestimated by  $\sim 50\%$ . We examine the most extreme of these cases (150% overestimation) and how it impacts our results. We first reduce the mass of our AGN population and then re-sample our mass-matched control sample of inactive galaxies. We find the total average logarithmic offset in SFR between active and inactive galaxies to decrease from  $0.34 \pm 0.07$  dex to  $0.25 \pm 0.07$  dex. Since the masses of AGN hosts are only ever overestimated by the SED fits, any sSFR discrepancy is considered to be a minor effect, if this systematic is present.

## 3.4 Discussion

While numerous studies have examined the difference between star formation activity in AGN hosts and inactive galaxies, their results tend to be conflicting. Earlier studies, which were often limited to low redshifts, low sample sizes, and no control or crudely matched comparison samples, predominantly found suppressed star formation activity in AGN hosts (e.g. Ho, 2005; Kim et al., 2006; Salim et al., 2007). However, with improved selection techniques and deeper observations, recent findings have found their star formation activity is more similar or even elevated over inactive galaxies (Xue et al., 2010; Mullaney et al., 2012a; Juneau et al., 2013). By implementing multiple AGN selection techniques and pushing to higher redshifts with deep multi-wavelength data, the present work supports the latter.

Predominantly, we find that AGN hosts exhibit a slight elevation in star formation activity over inactive galaxies. This elevation is consistent across all redshifts, but less pronounced at high stellar mass. The exception to this elevation is low redshift, radio AGN. As seen in Figure 3.3, this population is found to be exclusively hosted by quenched galaxies, which exhibit a lower level of star formation activity than their mass-matched, inactive counterparts (see Table 3.3). For early studies, limited to low redshifts, this was well established (e.g. Matthews et al., 1964), and possibly led to an early perception that AGN are associated with quenched, elliptical galaxies. Unlike infrared and high redshift ( $z > 0.8$ ) radio AGN hosts, which exhibit a strong elevation in star formation over their respective control samples, we find the offset for galaxies hosting X-ray AGN to be only marginal. Recent studies, while different in their approach, tend to find similar results. For example, in Bongiorno et al. (2013), the authors found their sample of type-II AGN to have, on average, the same or slightly lower SFRs than inactive galaxies of the same mass and redshift. Mullaney et al. (2015) find the same, but compare their AGN sample to a main-sequence of star-forming galaxies. While we find slightly higher star formation in X-ray AGN hosts, this can possibly be explained away by our different approach and selection effects (i.e., our star formation estimates, mass, luminosity and redshift cuts). That being said, the overarching theme is consistent between all of these recent studies - the star formation activity of X-ray AGN hosts is mostly consistent with normal galaxies.

While the elevated levels of star formation in X-ray AGN are at best marginal, the offset between IR AGN and the control sample is explicit. The mean sSFR for IR AGN hosts is found to be as much as  $\sim 5$  times higher, suggesting there exists a stronger link between IR AGN and its host, than in other types of AGN. Such an analysis has not been accomplished before at high-redshifts due to the concerns of reliable AGN selection and potential AGN contamination in SFR estimates. We attempt to mitigate against these by employing the latest IR AGN selection techniques and  $160\mu\text{m}$  derived SFRs, which are believed to be predominantly free from AGN activity. With that said, we acknowledge a 100% reliable and contaminant-free sample remains impossible.

*UVJ* diagnostics reveal that different AGN types (i.e. radio, X-ray or IR) are hosted by galaxies with different stellar properties at low redshift. This is consistent with studies that have examined the evolution of multi-wavelength AGN, where they're found to evolve with galaxies in the sequence of dusty IR AGN  $\rightarrow$  unobscured X-ray AGN  $\rightarrow$  early-type galaxy with intermittent radio AGN (Hopkins et al., 2006; Hickox et al., 2009; Goulding et al., 2014). This scenario is also supported by Figure 3.5, where our IR AGN exhibit a star formation level consistent with young galaxies, radio AGN with quenched galaxies, and X-ray AGN straddling between the two. However, we find this trend weakens at higher redshifts ( $z \gtrsim 0.8$ ),

where all AGN are predominantly found to reside in star-forming galaxies, including our high-redshift radio AGN population. This being said, we remind the reader that a comparison between redshifts is inconclusive given the different luminosity depths used during AGN selection. Despite this, our result is supported by the recent findings of Rees et al. (2016) who find the majority of radio AGN at  $z > 1.5$  are hosted by star-forming galaxies. Such results contradict the before-mentioned perception that AGN hosts are traditionally viewed as quenched, elliptical galaxies.

As found in Figure 3.3, the *UVJ* colours also reveal AGN hosts tend to be dustier than the control sample of galaxies. Similar to the offsets in star formation, this is primarily driven by IR AGN, while for X-ray AGN the difference is marginal. These findings further support the scenario of an evolutionary sequence of dusty IR AGN  $\rightarrow$  unobscured X-ray AGN, where copious amounts of gas and dust can fuel both a period of high star formation and AGN before it begins to exhaust, star formation slows, and X-rays from the AGN can shine through. Previous studies, which have examined star formation activity in AGN hosts, commonly invoke a major merger scenario to interpret the finding of elevated star formation over inactive galaxies (Santini et al., 2012; Rosario et al., 2012; Juneau et al., 2013). In such a scenario, gas is driven to the central regions of merging galaxies, fuelling both a period of starburst and AGN activity. Merger-driven elevations of star formation activity have also been postulated to occur in ULIRGs and high- $z$  submillimeter galaxies (Pope et al., 2013).

Another possible explanation is that positive feedback from AGN activity triggers a flash of star formation, which could lead to the elevated sSFRs seen in our AGN sample. Some studies have shown observationally that AGN activity enhances star formation in both radiatively efficient (e.g. Santini et al., 2012) and inefficient AGN (e.g. Karouzos et al., 2014) and is commonly explained by gravitationally collapsed cold gas resulting from AGN outflows, such as jets and accretion disk winds. Invoking this scenario would address the elevation of star formation activity seen in our radio, X-ray and IR AGN hosts, but also leave the door open for the eventual quenching of star formation from AGN negative feedback – as seen in low redshift radio AGN hosts.

While star formation suppression is still required to reduce the over-predicted abundance of massive galaxies in models, we see no direct evidence radiatively efficient AGN contributes to this suppression. Indeed, findings from recent simulations suggest that while AGN in isolated star-forming galaxies can remove substantial amounts of gas, this does not translate to a rapid quenching of star formation (Gabor & Bournaud, 2014; Roos et al., 2015). Despite our inability to isolate a cause, the fact our AGN population exhibits a similar to slightly elevated level of star formation activity over most of cosmic time – and not a suppressed

one – calls into question the significance of AGN quenching as a major mechanism for moderating galaxy growth.

## 3.5 Summary

In this chapter, we have utilised high-quality ground-based imaging from ZFOURGE in combination with ancillary data to select radio, X-ray and IR AGN hosts out to high redshifts ( $z = 0.2 - 3.2$ ). The deep imaging of ZFOURGE further provides us with host galaxy properties, including rest-frame colours, low stellar masses and accurate photometric redshifts. We maximise completeness by limiting our sample by mass, luminosity and redshift before conducting a detailed analysis of the rest-frame  $UVJ$  colours and star formation activity of AGN hosts. We also create a control sample of mass-matched, inactive galaxies to isolate the impact of AGN activity on star formation. As discussed in Section 3.3.3, one of the uncertainties in this study (and all such studies) is conceivably the impact of AGN emission in the measurement of host galaxy properties. We assumed this impact is negligible, but it is difficult to test this assumption more rigorously. Our main findings are as follows:

1. Radio, X-ray and IR-selected AGN hosts exhibit rest-frame  $UVJ$  colours consistent with distinct galaxy populations. IR AGN tend to favour star-forming galaxies, radio AGN favour quiescent galaxies, and X-ray AGN straddle between the two. However, this distinction becomes blurred at higher redshifts ( $z \gtrsim 1.8$ ), where all AGN favour star-forming hosts.
2. The  $UVJ$  diagnostics also reveal AGN have a higher dusty star-former fraction ( $N_{\text{dusty}}/N_{\text{sf}}$ ) and lower quiescent fraction ( $N_{\text{q}}/(N_{\text{q}} + N_{\text{sf}})$ ) when compared to the control sample of inactive galaxies.
3. The star formation activity (mean sSFR) of all AGN hosts tends to be elevated over inactive galaxies (average logarithmic offsets of  $0.26 \pm 0.14$  dex at  $z = 0.2 - 0.8$ ,  $0.37 \pm 0.10$  dex at  $z = 0.8 - 1.8$ , and  $0.38 \pm 0.10$  dex at  $z = 1.8 - 3.2$ ).
4. The star formation activity (mean sSFR) of the split sample of radio, X-ray and IR AGN hosts is predominantly elevated over their respective control sample of inactive galaxies. IR AGN hosts exhibit an explicit and consistent  $\sim 0.57$  dex elevation, X-ray AGN hosts a marginal  $\sim 0.21$  dex elevation, while radio AGN hosts flip from a lower mean sSFR ( $-0.53 \pm 0.20$  dex;  $z = 0.2 - 0.8$ ) to higher level ( $0.55 \pm 0.32$  dex;  $z = 1.8 - 3.2$ ) at high redshift.

5. One possibility for the elevated star formation is that these AGN hosts are mergers where cold gas fuels both a period of starburst and AGN activity. Though not explored here, this scenario may be tested by comparing the morphologies determined from the existing HST imaging of these fields.

# Chapter 4

## Decoupled Black Hole Accretion and Quenching

Portions of this chapter are based on a single paper, which appears in *Monthly Notices of the Royal Astronomical Society*, 2017, Volume 473, 3710-3716. The co-authors are L. Spitler, R. Quadri, A. Goulding, C. Papovich, K-V. Tran, I. Labbé, L. Acorn, R. Allen, B. Forrest, K. Glazebrook, G. Kacprzak, G. Morrison, T. Nanayakkara, C. Straatman, and A. Tomczak. L. Spitler and R. Quadri supervised this work and provided guidance with respect to the methodology and scientific interpretation. A. Goulding provided guidance and assistance with respect to the X-ray analysis. The remaining co-authors provided discussion and feedback towards the final manuscript. The candidate's contribution to the work presented in this paper is 95%.

### 4.1 Introduction

The Milky Way (MW) and Andromeda (M31) have long provided astronomers with invaluable insight into galaxy evolution (Freeman & Bland-Hawthorn, 2002). With deep new surveys, it is now possible to search for their probable progenitors at high- $z$  and learn about their evolutionary history that led to their present-day properties. For example, Van Dokkum et al. (2013) used data from the 3D-HST (Brammer et al., 2012) and CANDELS (Grogin et al., 2011; Koekemoer et al., 2011) surveys to probe MW-mass progenitors out to  $z = 2.5$ , while Papovich et al. (2015) used data from the ZFOURGE survey (Straatman et al., 2016) to probe MW- and M31-mass progenitors, while pushing to higher redshifts ( $z \sim 3$ ). By investigating the evolution of various physical parameters, including rest-frame colours, morphologies, gas fractions, size, and star formation rates, these studies point to a scenario

in which the progenitors of MW- and M31-mass galaxies gradually transition from gas-rich, star-forming galaxies at high- $z$  to quenched, bulge-dominated galaxies at low- $z$ .

As mentioned in previous chapters, numerous studies have shown there is a close connection between SMBHs and their host galaxies (e.g. Silk & Rees, 1998; Marconi et al., 2004; Croton et al., 2006; Cisternas et al., 2011; Rafferty et al., 2011; Chen et al., 2013; McConnell & Ma, 2013; Dai et al., 2015; Heinis et al., 2016). Close similarities between the cosmic star formation history and the black hole accretion density, as a function of redshift, is further evidence of this kind of connection (e.g. Madau et al., 1998; Hasinger et al., 2005; Madau & Dickinson, 2014). These works have investigated the SMBH-galaxy connection by simultaneously measuring the AGN accretion rate and the host star formation rate individually or by averaging over a well defined AGN sample. However, what can be learned from these works is limited due to progenitor bias (e.g. Van Dokkum & Franx, 2001; Leja et al., 2013). Progenitor bias arises from the assumption that high redshift galaxies are drawn from, and can be directly compared to, the same distribution as low redshift galaxies in galaxy evolution studies. However, the morphologies of galaxies are known to significantly evolve from high to low redshift, thus the effect of progenitor bias is that observations underestimate the true evolution of galaxies. Given this, it is pertinent to ask whether the SMBH-galaxy correlations hold within the framework of evolving MW- and M31-mass progenitors, which may provide greater insight into the processes that drive the transition of star-forming galaxies into quiescent ones.

In this chapter, we investigate the SMBH-galaxy co-evolution of MW- and M31-mass progenitors by tracking their mean BHARs and mean SFRs since  $z = 2.5$ . We place these results in the context of galaxy quenching by comparing the evolution of the BHARs and SFRs to the quenching rate over similar timescales. This work will help provide greater insight into the formation processes of MW- and M31-mass progenitors and to what extent the feedback from SMBH accretion plays in the quenching of galaxies over cosmic time.

## 4.2 Data Sets

In this chapter, the database is identical to that we use in Chapters 2-3, i.e. the galaxies are selected from the ZFOURGE<sup>1</sup> catalogues (Straatman et al., 2016), which has coverage in three  $11' \times 11'$  pointings in the CDFS (Giacconi et al., 2002), COSMOS (Scoville et al., 2007), and UDS (Lawrence et al., 2007) fields. We supplement the ZFOURGE data with existing data from *Spitzer*/IRAC and *Herschel*/PACS to generate multi-wavelength catalogues spanning  $0.3 - 160 \mu\text{m}$ . Photometric redshifts were calculated in EAZY (Brammer et al., 2008)

---

<sup>1</sup><http://zfouge.tamu.edu>



using five templates generated from the PÉGASE library (Fioc & Rocca-Volmerange, 1997), plus three additional dust-reddened templates (Brammer et al., 2008), a passive red galaxy template (Whitaker et al., 2011), and a strong emission line galaxy template (Erb et al., 2010). Stellar masses were calculated by fitting the Bruzual & Charlot (2003) models to FAST (Kriek et al., 2009), assuming solar metallicity, a Calzetti et al. (2000) dust extinction law (with  $A_V = 0 - 4$ ), a Chabrier (2003) initial mass function (IMF) and exponentially declining star formation histories of the form  $\text{SFR}(t) \propto e^{-t/\tau}$ .

To estimate the average BHAR of the MW- and M31-mass progenitors, we measure AGN luminosities using a combination of IR and X-ray observations. We make use of overlapping *Spitzer*/MIPS and *Herschel*/PACS FIR imaging, which is sourced from the GOODS *Spitzer* Legacy program (PI: M. Dickinson) and GOODS-H (Elbaz et al., 2011) for the ZFOURGE-CDFS field, S-COSMOS *Spitzer* Legacy program (PI: D. Sanders) and CANDELS-H (Inami et al. 2017, in prep) for the ZFOURGE-COSMOS field, and SpUDS *Spitzer* Legacy program (PI: J. Dunlop) and CANDELS-H for the ZFOURGE-UDS field. For X-ray observations, we make use of the deepest *Chandra* imaging available, which is sourced from the *Chandra* Deep Field-South Survey: 7 Ms Source catalogs (Luo et al., 2017) for the ZFOURGE-CDFS field, the *Chandra* COSMOS Survey I. Overview and Point Source catalogue (Elvis et al., 2009) for the ZFOURGE-COSMOS field, and the X-UDS *Chandra* Legacy Survey (PI: Hasinger) for the ZFOURGE-UDS field.

## 4.3 Data Analysis

### 4.3.1 Progenitor Selection

To investigate the evolution of MW- and M31-mass galaxies, we select progenitors with present-day stellar masses near those of the MW ( $M_* = 5 \times 10^{10} M_\odot$  at  $z = 0$ ; McMillan, 2011; Van Dokkum et al., 2013; Licquia & Newman, 2015) and M31 ( $M_* = 10^{11} M_\odot$  at  $z = 0$ ; Mutch et al., 2011). Progenitor galaxies were selected using the approach in Papovich et al. (2015), who traced the stellar-mass evolution of present-day MW- and M31-mass galaxies using the multi-epoch abundance matching (MEAM) method of Moster et al. (2013). From this work, Moster et al. (2013) derived the fitting functions for the star formation history and mass accretion history for galaxies of arbitrary present-day stellar mass. Papovich et al. (2015) then integrated the fitting functions with respect to time, accounting for mass losses from stellar evolution, to derive the stellar mass evolution of the present day MW-mass and M31-mass galaxies. The stellar mass of the progenitors is selected within  $\pm 0.25$  dex of the central value of stellar mass in each redshift. This value was motivated by the scatter in

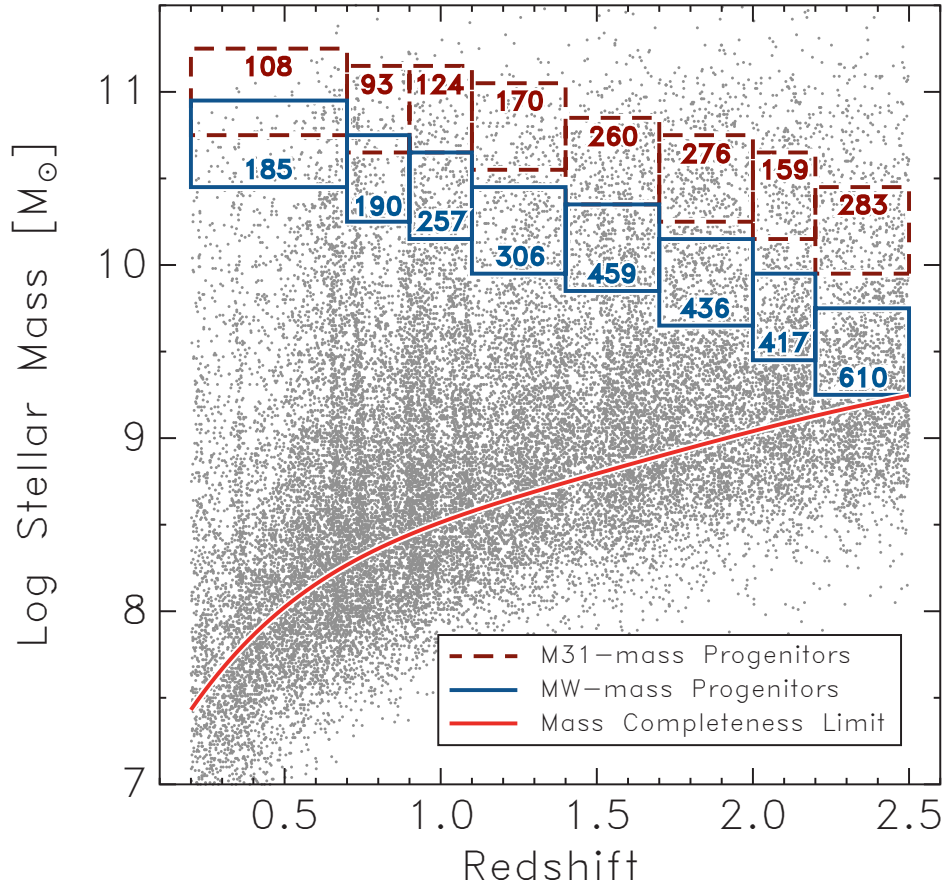


**Fig. 4.1** The stellar-mass evolution of MW-mass (solid blue line boxes) and M31-mass (dashed red line boxes) galaxy progenitors, including counts for each redshift bin. Box sizes are representative of the data points show the stellar masses of all sources in ZFOURGE over  $z = 0.2 - 2.5$ . The red curve shows the 80% stellar mass completeness limit for star-forming and passive galaxies in ZFOURGE (Spitler et al. 2017, in prep).

the stellar mass of the progenitors of present-day galaxies (see Papovich et al., 2015). At higher redshift, the interval in redshift bins increases as a compromise between comoving volume and lookback time spanned by each bin. As shown in Figure 4.1, estimates for the 80% mass completeness limits mean the data from ZFOURGE is unlikely to introduce selection biases in our attempt to track the stellar mass evolution of progenitors to  $z = 2.5$ . We identify 2,860 MW-mass galaxy progenitors and 1,473 M31-mass galaxy progenitors, spanning  $z = 0.2 - 2.5$ .

### 4.3.2 Black Hole Accretion Rates

The luminosity emitted by an AGN is a result of a mass-accretion event (e.g. Alexander & Hickox, 2012) which can be described by  $L_{\text{AGN}} = \varepsilon c^2 dM/dt$ , where  $\varepsilon$  is the accretion efficiency (often estimated to be  $\varepsilon = 0.1$ ; e.g. Marconi et al., 2004). In units of  $M_{\odot}\text{yr}^{-1}$ , the BHAR can be expressed as:

$$\text{BHAR} = 0.15 \frac{0.1}{\varepsilon} \frac{L_{\text{AGN}}}{10^{45} \text{erg s}^{-1}} \quad (4.1)$$

where  $L_{\text{AGN}}$  is the AGN bolometric luminosity. In the following section, we describe the methods used to estimate  $L_{\text{AGN}}$  for all AGN in our sample.

### 4.3.3 SED Decomposition of $L_{\text{IR}}$

We use the multi-component SED fitting code, CIGALE<sup>2</sup> (Code Investigating GALaxy Emission; Burgarella et al., 2005; Noll et al., 2009) to decompose the rest-frame IR luminosity ( $L_{\text{IR}}$ ) of MW- and M31-mass galaxy progenitors into their AGN and star-forming components. By binning these components, we respectively estimate the mean BHARs and SFRs of the progenitors in bins of stellar mass and redshift. In Table 4.1, we list the parameters we use to complete SED fitting and decomposition. CIGALE completes decomposition using a two-step process. First, it creates a library of SED models using the chosen parameters, before identifying the best-fit model to the observed photometry through  $\chi^2$  minimisation. Galaxy parameters and their associated uncertainties are estimated using a Bayesian approach, which derives the probability that each parameter value is representative of a given galaxy (see Burgarella et al., 2005). From these various parameters, we focus on the recovered  $L_{\text{IR}}$ , which consists of contributions from stellar-heated dust (dominated by young stars) and AGN-heated dust ( $L_{\text{AGN}}$ ).

For the stellar-heated dust, we adopt the semi-empirical templates of Dale et al. (2014), which include modified templates from the Dale & Helou (2002) library. For the AGN-heated dust, we adopt the templates of Fritz et al. (2006), which consider the emission of the central source as well as the radiation from the dusty torus. The Fritz et al. (2006) templates introduce six additional parameters (see Table 4.1), which describe the geometrical configuration of the torus and the properties of the dust emission. We fix these parameters to mean values based on studies that extensively test AGN fitting with CIGALE (Ciesla et al., 2015; Heinis et al., 2016; Bernhard et al., 2016; Wylezalek et al., 2016). By fixing these parameters, we reduce the parameter space and hence the overall degeneracy of the models, without compromising

---

<sup>2</sup><http://cigale.lam.fr>

**Table 4.1** Modules and Parameters used in CIGALE

Module	Model
Star Formation History	Delayed $\tau$
Single Stellar Population models	Bruzual & Charlot (2003)
Initial Mass Function	Chabrier (2003)
Attenuation law	Calzetti et al. (2000)
Dust emission models	Dale et al. (2014)
AGN emission models	Fritz et al. (2006)
Parameter	Value
E-folding timescale <sup>1</sup> , $\tau$ (Gyr)	1, 3, 5, 7, 9, 11
Age of oldest stars <sup>1</sup> , $t$ (Gyr)	1, 3, 5, 7, 9, 11
E(B-V) <sub>*</sub> for young population	0.01, 0.05, 0.1, 0.5, 1.0, 1.5
Ratio of torus radii <sup>2</sup>	60
Optical depth at 9.7 $\mu\text{m}$ of torus <sup>2</sup>	0.3, 3.0, 6.0, 10.0
Parameter for torus density <sup>2,3</sup> , $\beta$	-0.5
Parameter for torus density <sup>2,3</sup> , $\gamma$	0
Opening angle of torus <sup>2</sup>	100°
Angle of AGN axis to line of sight <sup>2</sup>	0.001°, 50.100°, 89.990°
AGN fraction of $L_{\text{IR}}$ <sup>2</sup>	0.00 - 0.95 (steps of 0.05)

<sup>1</sup>  $\text{SFR}(t) \propto e^{-t/\tau}$ <sup>2</sup> AGN parameters from Fritz et al. (2006)<sup>3</sup>  $\rho(r, \theta) = \alpha r^\beta e^{-\gamma|\cos(\theta)|}$ 

the recovery of the components. Further details are available in Ciesla et al. (2015), while Table 4.1 lists the parameters we use to complete SED fitting and decomposition.

A caveat to this approach is CIGALE's reliability at low AGN luminosities. Ciesla et al. (2015) found for such sources that the software would tend to overestimate the AGN contribution up to  $\sim 120\%$ . The authors attribute this overestimation to bias from the PDF analysis, where the PDF is truncated and returns an elevated value. To address this, we select all sources with  $\text{error\_}L_{\text{AGN}} > L_{\text{AGN}}$  and scatter them down by randomly drawing a new  $L_{\text{AGN}}$  value from a Gaussian centred on zero with a standard deviation of  $\text{error\_}L_{\text{AGN}}$ . We compute the averages reported below using these new  $L_{\text{AGN}}$  values whenever CIGALE

returns a non-detection of an IR AGN component. For a secure detection, we adopt the output directly from CIGALE

Previous studies, which have used CIGALE to decompose the  $L_{\text{IR}}$  have shown robust luminosity estimations are heavily reliant on rest-frame IR data (Buat et al., 2013; Ciesla et al., 2015). Therefore, we use FourStar (1.1, 1.2, 1.3, 1.6, 1.7, and 2.2  $\mu\text{m}$ ), IRAC (3.6, 4.5, 5.8, and 8  $\mu\text{m}$ ), MIPS (24  $\mu\text{m}$ ), and PACS (100 and 160  $\mu\text{m}$ ) broadband data in our SED fitting. While all sources are detected in multiple bands, only  $\sim 65\%$  are detected in at least one near-IR, one mid-IR, and one far-IR band. For non-detections (flux  $< 0$ ), we replace flux values with their corresponding uncertainties and treat them as upper limits. Such limitations may result in an increased  $\chi^2$  during the fitting process. Examples of best-fit models and decomposition are shown in the left panel of Figure 4.2.

We apply two tests in order to assess CIGALE’s ability to robustly estimate parameters. The first is a check of the CIGALE-derived SFRs, which we achieve by comparing the results to those from an FIR-derived conversion of the bolometric 8 – 1000  $\mu\text{m}$  IR luminosity calculated from a luminosity-independent conversion (Wuyts et al., 2008, 2011) using PACS 160  $\mu\text{m}$  fluxes. The results, which are presented in the right panel of Figure 4.2, show a strong correlation between the two methods of derivation. A noticeable exception is for a selection of high redshift sources, which stray from the 1:1 line. When we investigate these sources, we find they are dominated by AGN (i.e. greater than 50% AGN-heated component) to the  $L_{\text{IR}}$ . While the FIR regime is believed to be largely uncontaminated by AGN, it is not completely immune from AGN-dominated sources towards higher redshifts (Netzer et al., 2007; Mullaney et al., 2012a). This is likely why some of our AGN-dominated sources at high redshift exhibit FIR-derived SFRs that are elevated over their CIGALE-derived counterparts.

The second test we perform is by way of CIGALE’s mock utility, which generates a mock catalogue of artificial SEDs using the best-fit templates to the observed SEDs. The mock catalogue is built by integrating the best-fit SED of each source in the observed bands, before random noise, distributed assuming Gaussian errors with the observed error as the standard deviation, is added to the fluxes. We then run CIGALE on the mock galaxy SEDs and compare the input parameters to the recovered parameters. The results are shown in Figure 4.3. For both the AGN-heated and stellar-heated dust components, we find a very good correlation with  $R > 0.90$ , suggesting CIGALE’s ability to recover parameters is robust, despite the limited filter set and typical flux errors of our observational data. We also point the reader to Ciesla et al. (2015), for a detailed study of broadband SED fitting methods and the reliability of CIGALE to recover parameters via decomposition.

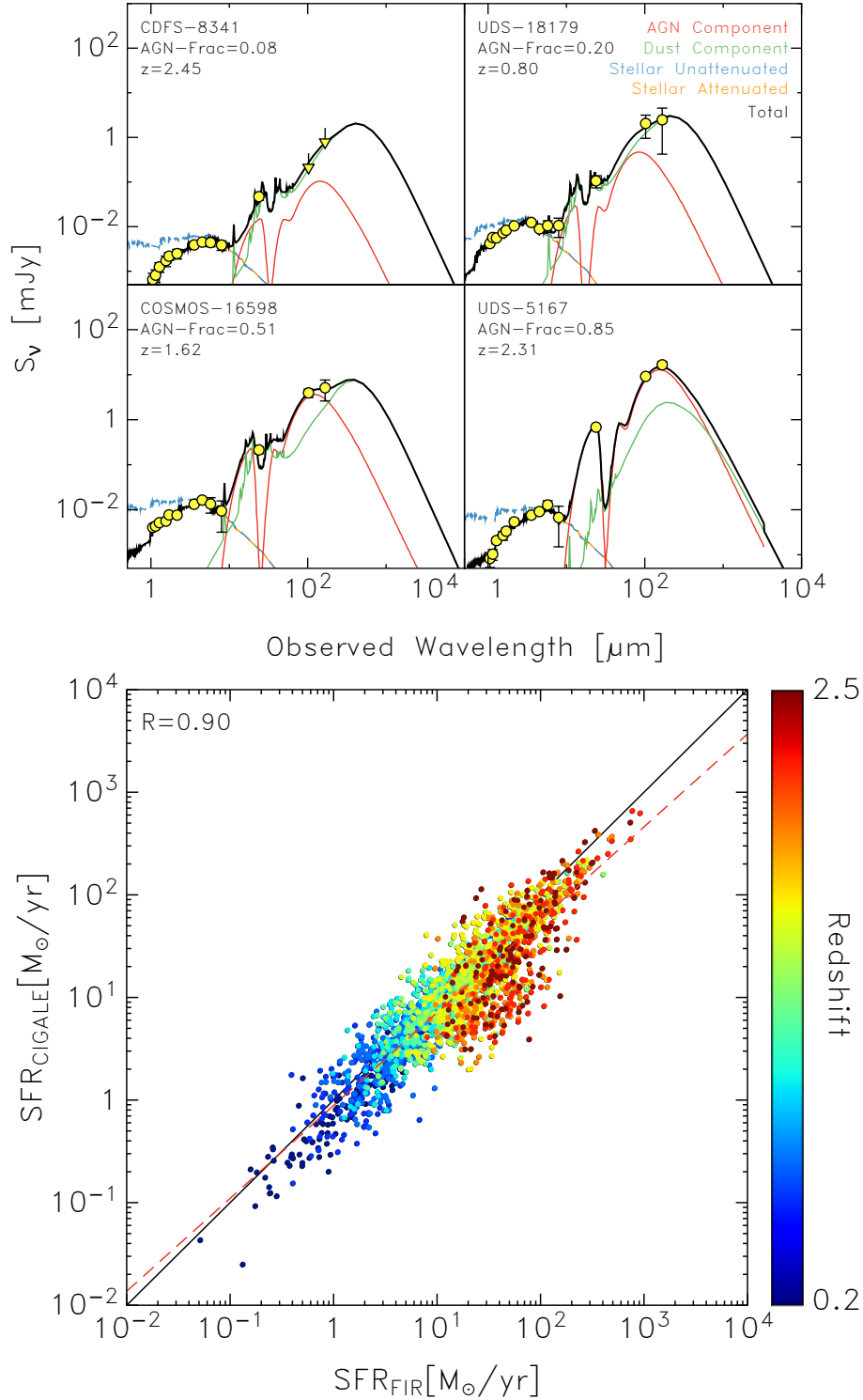


**Fig. 4.2** *Top panels:* SED decomposition on a selection of ZFOURGE sources using CIGALE (Burgarella et al., 2005; Noll et al., 2009). Yellow circles are the observed points, yellow arrows are the upper limits, and the black lines are the best-fit total models. We also show the AGN component in solid red lines, stellar-heated dust component in solid green lines, the unattenuated stellar emission in dashed blue lines, and the attenuated stellar emission in solid orange lines. The corresponding redshift and fraction of AGN emission to the  $L_{\text{IR}}$  for each source are also provided. *Bottom panel:* a comparison of CIGALE-derived SFRs to those from an FIR-derived conversion of the bolometric 8 – 1000  $\mu\text{m}$  IR luminosity calculated from a luminosity-independent conversion (Wuyts et al., 2008, 2011) using PACS 160  $\mu\text{m}$  fluxes. The solid black line is the 1:1 relation, while the dashed red line is the best fit. We also show the linear Pearson correlation coefficient,  $R$ .

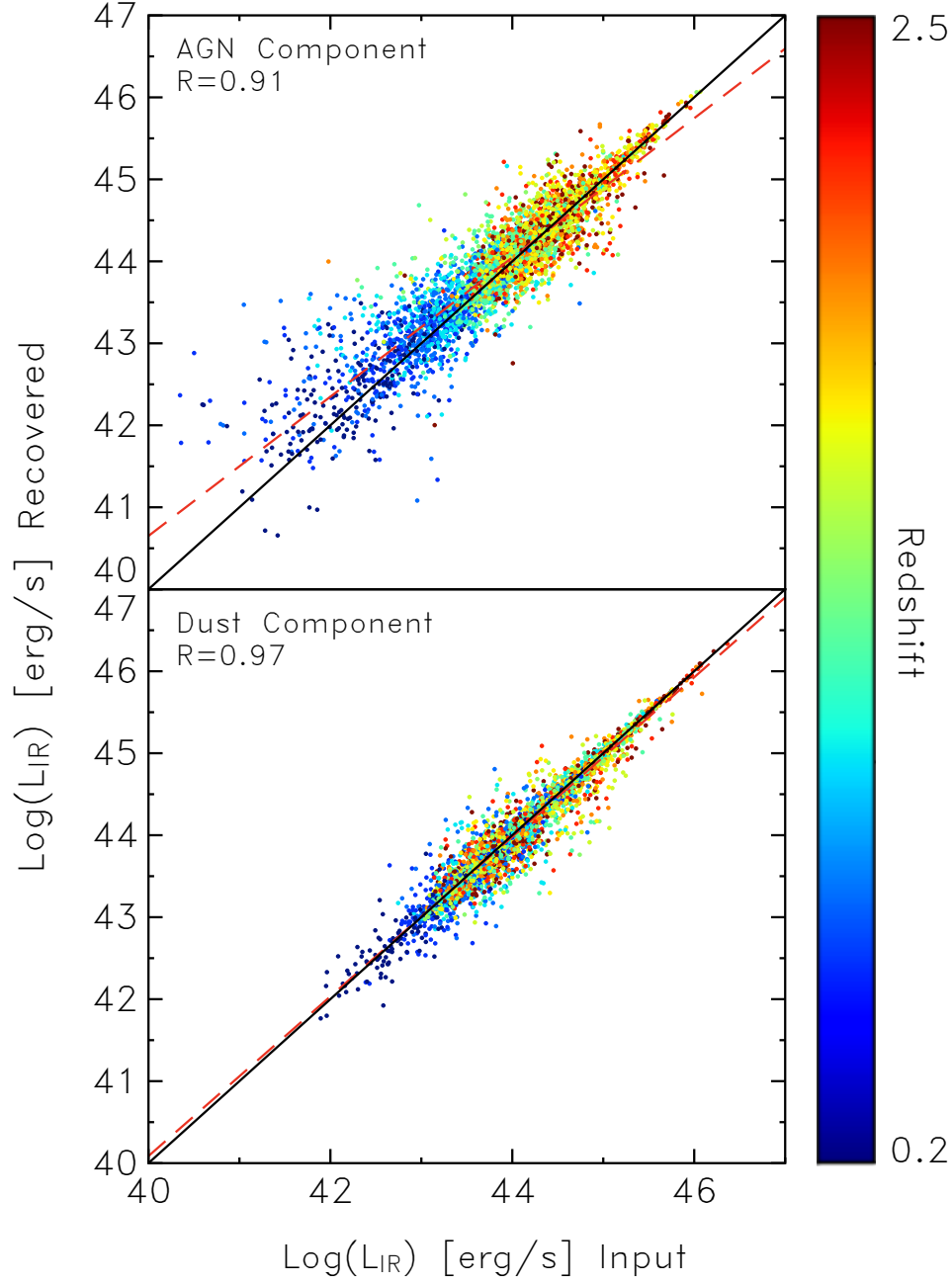


**Fig. 4.3** Comparison of the AGN-heated (top panel) and stellar-heated dust components (bottom panel) recovered by CIGALE for our mock galaxy SEDs. Points are coloured by redshift. The solid black line is the 1:1 relation, while the dashed red line is the best fit. We also show the linear Pearson correlation coefficient,  $R$ .

### 4.3.4 $L_{\text{AGN}}$ from X-ray Stacking

We use the X-ray stacking code, STACKFAST<sup>3</sup> (Hickox et al., 2007) to estimate the average X-ray luminosity for MW- and M31-mass galaxy progenitors in bins of redshift. X-ray stacking allows us to account for those sources that are not individually detected in X-rays. We determine the stacked source count rate (in counts  $\text{s}^{-1}$ ) for the M31- and MW-mass progenitors in bins of redshift and convert to flux (in  $\text{ergs cm}^{-2} \text{s}^{-1}$ ) in the 0.5-7 keV band assuming an intrinsic X-ray spectrum with  $\Gamma = 1.8$ . We derive the average X-ray luminosity using:

$$L_{\text{X}}[\text{erg s}^{-1}] = 4\pi d_l^2 (1+z)^{\Gamma-2} f_x \quad (4.2)$$

where  $d_l$  is the average luminosity distance determined for each redshift bin. Finally, to convert  $L_{\text{X}}$  to  $L_{\text{AGN}}$ , we apply a constant bolometric correction factor of 22.4 (based on a sample of local,  $L_{\text{X}} = 10^{41-46} \text{ erg s}^{-1}$ , AGN from Vasudevan & Fabian 2007). When calculating  $L_{\text{AGN}}$  from the X-ray luminosity, we estimated the contribution to the X-ray emission by star formation using the approach in Lehmer et al. (2016), but found it to be less than the associated errors. Given this, star formation contribution to the X-ray emission is not considered here. More details of STACKFAST are described in Section 5.1 of Hickox et al. (2007), while the basics of our X-ray data processing, reduction and image analysis can be found in Goulding et al. (2012).

## 4.4 Results

### 4.4.1 Evolution of Star Formation and Black Hole Accretion

#### Evolution of the Black Hole Accretion Rates

Using Equation (4.1), we estimate the mean BHAR of all galaxies in bins of stellar mass and redshift and plot the BHAR history of the MW- and M31-mass progenitors in Figure 4.4 (top panel). Both the X-ray and IR-derived BHARs start relatively high in the highest redshift bins and track a similar path as they reduce in rate towards the present day. The notable difference between the two samples is a significant offset. Specifically, we find the IR-derived BHARs to be  $\sim 4$  times higher than the X-ray BHARs. One likely cause of this discrepancy is absorption effects. Currently, we assume no absorption during the X-ray analysis, but if we let the average intrinsic neutral hydrogen column density for the X-ray sample be  $N_{\text{H}} \sim 3 \times 10^{23} \text{ cm}^{-2}$  (i.e. heavily obscured), this would fully account for the offset. Such

<sup>3</sup><http://www.dartmouth.edu/~stackfast/>



levels of obscuration are supported by the flux HR of our X-rays<sup>4</sup>. A similar elevation for IR-derived BHARs was found in Gruppioni et al. (2011).

### Evolution of the Star Formation Rates

Figure 4.4 (middle panel) shows the evolution of the mean SFRs, in bins of stellar mass and redshift, for the progenitors. For the M31-mass progenitors, SFRs start high ( $> 30 M_{\odot} \text{ yr}^{-1}$ ) at the highest redshifts observed, before peaking at  $\sim 40 M_{\odot} \text{ yr}^{-1}$  around  $z \sim 1.75$ . Following this peak, the SFRs for the M31-mass progenitors decline monotonically to values of a few solar masses per year at  $z = 0.2$ . The MW-mass progenitors follow a similar trend, but are lower at  $z > 1$ . The SFRs for MW-mass progenitors start at  $\sim 5 M_{\odot} \text{ yr}^{-1}$  in the highest redshift bins, peak at  $\sim 15 M_{\odot} \text{ yr}^{-1}$  around  $z \sim 1.5$ , and then decline at similar values to the M31-mass progenitors at  $z < 1$ . The evolution of the mean SFRs in Figure 4.4 are found to qualitatively match those in Van Dokkum et al. (2013) and Papovich et al. (2015), albeit slightly lower in value. As mentioned in Section 4.3.3, this offset is likely attributed to the different approach to deriving SFRs and the removal of AGN emission performed in this study.

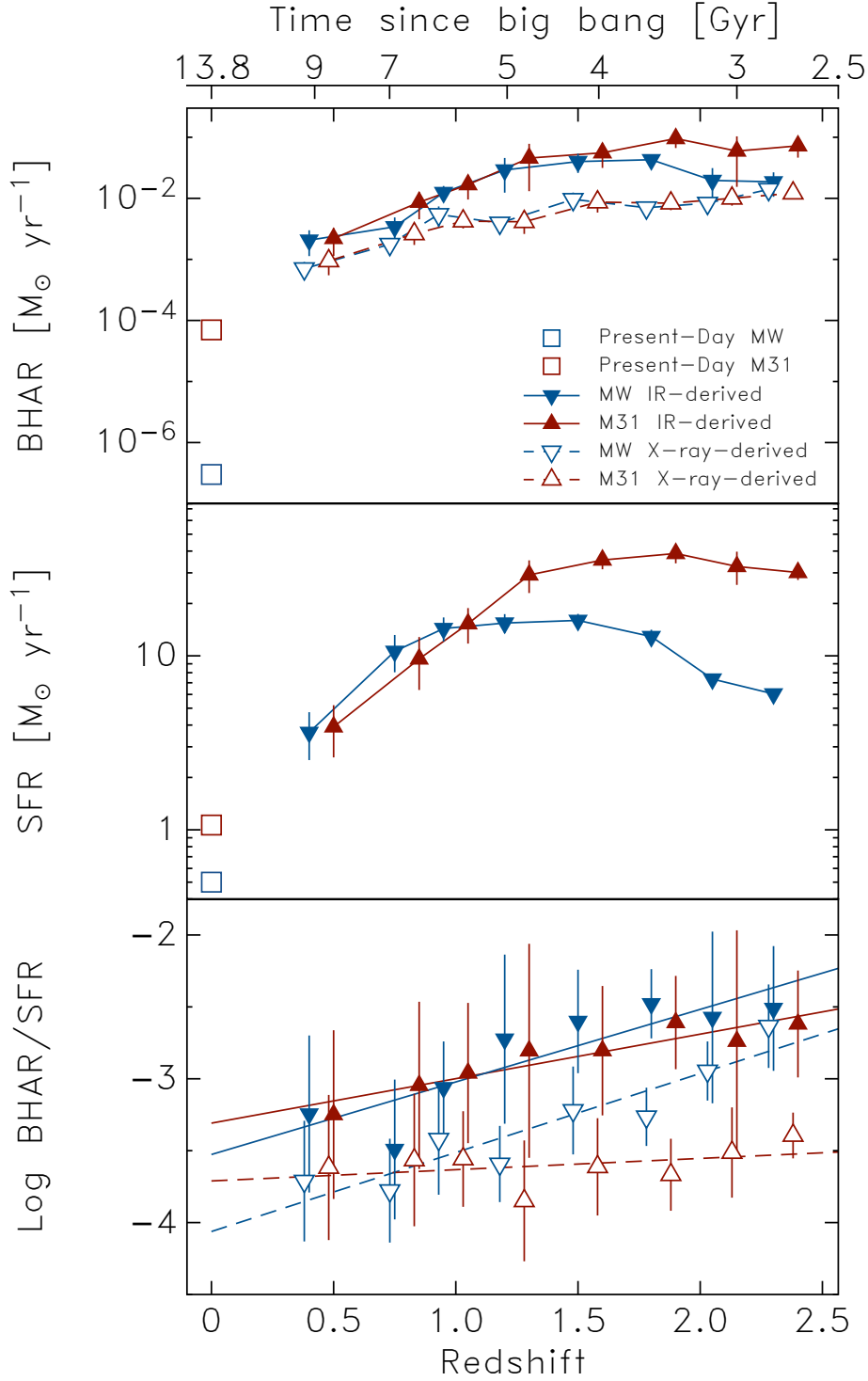
### Evolution of the Relative Black Hole-Galaxy Growth

Figure 4.4 (bottom panel) shows the evolution of the ratio between the BHAR and SFR for the progenitors. In all cases, we find the BHAR/SFR ratios increase with redshift for the MW- and M31-mass progenitors. Upon applying a least-squares fit, we find the slopes of the MW-mass progenitors to be  $0.64(\pm 0.11)$  (i.e.  $\log[\text{BHAR}/\text{SFR}] = 0.64(\pm 0.11) \times z - 3.52$ ) and  $0.55(\pm 0.10)$  for the IR-derived and X-ray-derived BHAR/SFR ratios, respectively. This is marginally stronger than the M31-mass progenitors, which exhibit slopes of  $0.39(\pm 0.08)$  and  $0.08(\pm 0.08)$ . The flatter slope of the massive M31-mass progenitors is more consistent with studies that adopt different sample selection, such as Calhau et al. (2017) who find an almost flat relationship of  $\sim 10^{-3.2}$  in BHAR/SFR over  $z = 0 - 2.23$  for  $\text{H}\alpha$ -selected star-forming galaxies.

### Evolution of the Quiescent Fraction and Quenching Rate

Figure 4.5 (top panel) shows the evolution of the quiescent fraction of the progenitors, where the quiescent fraction is defined as the ratio of the total number of quiescent galaxies to the

<sup>4</sup>We calculate flux HR between the 0.5-2 and 2-7 keV bands. We find HR values consistent with moderate to heavy obscuration, with the M31-mass progenitors systematically higher ( $\text{HR} \sim 4$ ) than the MW-mass progenitors ( $\text{HR} \sim 3.8$ )



**Fig. 4.4** *Top panel:* The mean BHAR as a function of redshift for our MW- (blue; down triangles) and M31-mass (red; up triangles) progenitors. Vertical errors represent errors on the mean. A slight offset in redshift is applied for clarity. We also provide BHAR values for the present-day MW (blue box; Yusef-Zadeh et al., 2015) and M31 (red box; Liu & Melia, 2001). *Middle panel:* the mean SFR as a function of redshift for our progenitors (same symbols as top panel). We also provide SFR values for the present-day MW (blue box; Robitaille & Whitney, 2010) and M31 (red box; Kang et al., 2009). *Bottom panel:* the mean BHAR to SFR ratio as a function of redshift for our progenitors (same symbols as top panel). The solid lines indicate a least-squares linear fit to these data.

total number of galaxies ( $f_{\text{quies}} = N_{\text{quies}} / (N_{\text{quies}} + N_{\text{sf}})$ ). We separate quiescent galaxies from star-forming galaxies using  $UVJ$ -colour analysis (see Chapter 3). Errors are calculated using the Clopper-Pearson approximation of the binomial confidence interval. For both samples, the quiescent fraction increases with decreasing redshift. We also show the quenching rate (bottom-panel), which is the rate at which the progenitors quench (i.e. move from star-forming to quiescent in  $UVJ$ -colour space) per gigayear. We quantify the quenching rate as the probability that a star-forming progenitor will become quenched per unit time, i.e.  $(f_{\text{zbin}(n)}^{\text{sf}} - f_{\text{zbin}(n-1)}^{\text{sf}}) / f_{\text{zbin}(n)}^{\text{sf}} / \text{Gyr}_{\text{zbin}(n-1) - \text{zbin}(n)}$ . Evidence for AGN quenching would likely return high quenching rates during periods of high BHAR. Instead, we find the evolution of the BHAR for the the MW- and M31-mass progenitors (see Figure 4.4) to be decoupled from the quenching rate over similar timescales.

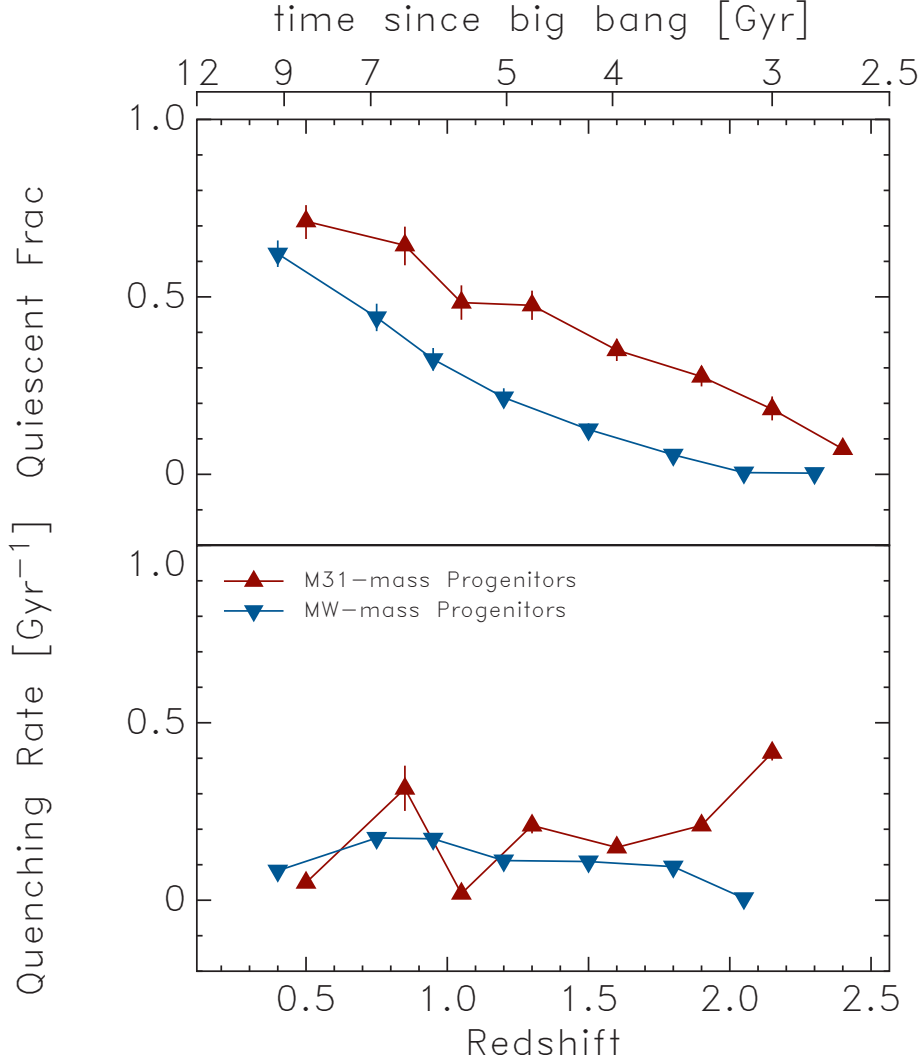


**Fig. 4.5** *Top panel:* The evolution of the quiescent fraction ( $f_{\text{quies}} = N_{\text{quies}} / (N_{\text{quies}} + N_{\text{sf}})$ ) for our MW- (blue; down triangles) and M31-mass (red; up triangles) progenitors as a function of redshift. We apply a slight offset in redshift for clarity. Vertical errors represent the binomial confidence interval. *Bottom panel:* the evolution of the quenching rate  $((f_{z_{\text{bin}(n)}}^{\text{sf}} - f_{z_{\text{bin}(n-1)}}^{\text{sf}}) / f_{z_{\text{bin}(n)}}^{\text{sf}}) / \text{Gyr}_{z_{\text{bin}(n-1)} - z_{\text{bin}(n)}}$  for our progenitors (same symbols as top panel).

## 4.5 Discussion

Tight correlations between BHAR and SFR are well documented (e.g. Merloni & Heinz, 2008; Aird et al., 2010; Gruppioni et al., 2011; Delvecchio et al., 2014) with both models (Silk, 2013) and observations (Calhau et al., 2017; Mullaney et al., 2012b; Dai et al., 2015) producing a nearly flat BHAR/SFR ratio across cosmic time. This flat correlation is often explained by a simple scenario where a joint fuelling process regulates both SMBH growth and star formation (see Mullaney et al., 2012b).

In contrast to past work, our results show that the BHAR/SFR ratios of our progenitor samples tend to decrease towards the present day. As this appears to hold whether we use X-ray or IR-derived BHARs (see the caveat for M31 below), we hypothesise this difference is driven by sample differences as previous efforts have used various sample galaxy selections (e.g. X-ray or mass-limited samples). To test this hypothesis, we limited our sample to X-ray selected AGN in ZFOURGE (see Chapter 2) and examined the evolution of the BHAR/SFR ratios for the MW- and M31-mass progenitors using both X-ray and IR-derived BHARs. We find an almost completely flat relationship in BHAR/SFR ratios (slopes of  $-0.04$  and  $-0.11$ , respectively) across all redshifts, which is consistent with the literature (e.g. Stanley et al., 2015).

While we find an evolving BHAR/SFR ratio for the bulk of our sample, a possible exception is the M31-mass progenitors, which exhibit an almost flat ratio when using the X-ray-derived BHARs. While this differs from the IR-derived BHAR/SFR ratios of the M31-mass progenitors, we postulate this may be driven by obscuration effects, where the X-rays of the more massive, high-redshift M31-mass progenitors are highly-obscured (e.g. Polletta et al., 2008; Treister et al., 2008). Indeed, when we investigate the X-ray hardness ratios for the M31-mass progenitors, we find results consistent with heavy obscuration ( $HR \sim 4$ ) at this redshift range. Therefore, such results argue for the inclusion of IR-based AGN whenever possible to fully assess the impact of dust obscuration changes.

The apparent differences we find for the evolution of BHAR/SFR ratios compared to past work illustrates the importance of selecting progenitor samples when looking for evolutionary changes in AGN. Indeed, mass-limited, star-forming or X-ray selected may not capture underlying evolutionary trends because these samples contain galaxies with very different evolutionary paths (Leja et al., 2013). The present work directly addresses this by adopting a selection that attempts to account for the mass growth of galaxies over the redshift range considered here.

Finally, the decline of the mean BHARs and SFRs with decreasing redshift casts doubts over the suppression of star formation being predominantly driven by luminous AGN feedback (i.e. high BHARs) in MW- and M31-mass progenitors. While one may expect to see

an increase in BHARs during a period of quenching, we instead find that the rate at which the progenitors quench (see Figure 4.5) is decoupled from the BHARs, which decline over similar timescales. An alternative scenario to explain this is one of morphological quenching (Martig et al., 2009), where the formation of a bulge stabilises gas in the galactic disk and suppresses the efficiency of star formation (e.g. Martig & Bournaud, 2010; Ceverino et al., 2010; Genel et al., 2012; Sales et al., 2012; Genzel et al., 2014).

This scenario is supported by the work of Papovich et al. (2015), who find the Sérsic index of the same progenitors to increase with decreasing redshift, suggesting growth in spheroid size towards the present. Using the Sérsic values from the ZFOURGE catalogues, we reproduce the same in Figure 4.6. This view is consistent with our results in Chapter 2, where AGN feedback is found to only play a dominant role in star formation quenching at lower- $z$ , during periods of low-level (i.e. radio-mode) activity in bulge-dominated hosts. With this said, if bulge growth remains closely tied to SMBH growth throughout cosmic time, then our BHARs suggest that bulge growth is decoupled from quenching.

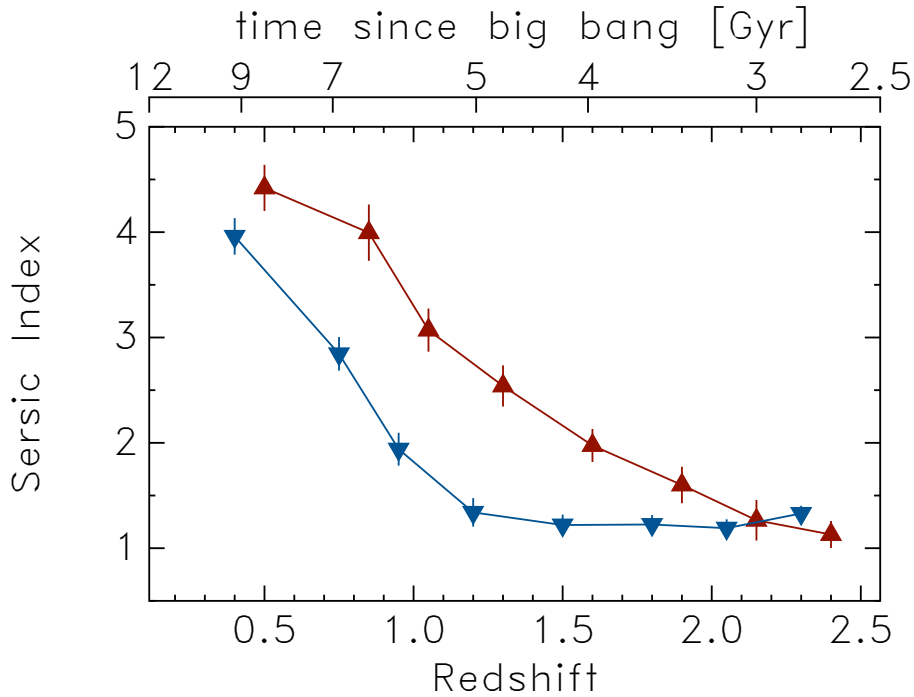


**Fig. 4.6** The evolution of the Sérsic index for our MW- (blue; down triangles) and M31-mass (red; up triangles) progenitors as a function of redshift. We apply a slight offset in redshift for clarity. Vertical errors represent the binomial confidence interval.

# Chapter 5

## A Two Band Approach to Isolate the AGN Contribution to Observed SEDs

Portions of this chapter are based on a single paper, which is planned to be submitted to *Monthly Notices of the Royal Astronomical Society*. The co-authors are L. Spitler, James Mullaney, K-V. Tran, and I. Labbé. L. Spitler supervised this work, James Mullaney provided guidance with respect to the methodology and scientific interpretation, while the remaining co-authors provided discussion and feedback towards the draft manuscript. The candidate's contribution to the work presented in this paper is 95%.

### 5.1 Introduction

In Chapter 4, we investigated the SMBH-galaxy connection by disentangling their relative emissions by way of SED decomposition. This approach has been adopted for numerous similar studies (Cisternas et al., 2011; Gruppioni et al., 2011; Rovilos et al., 2012; Santini et al., 2012; Bongiorno et al., 2013; Karouzos et al., 2014; Ciesla et al., 2015; Stanley et al., 2015; Gruppioni et al., 2016; Heinis et al., 2016), but also as a method to remove galaxy emission when investigating AGN (Murphy et al., 2008; Pozzi et al., 2012; Delvecchio et al., 2014; Rovilos et al., 2014). Unfortunately, the decomposition process is often reliant on an abundant amount of photometric data to adequately constrain relevant parameters. In this Chapter, we present work in progress for an approach to isolate the AGN contribution to the observed SED using only two wave bands. Such an approach lends itself to studies where abundant photometric data may be lacking. While the approach is not without its limitations, we show it can reproduce underlying trends known to exist in active galaxy samples. Specifically, we reproduce the correlation found between star formation and AGN

luminosity in IR-bright AGN sources (Netzer et al., 2007; Netzer, 2009; Gruppioni et al., 2016; Heinis et al., 2016).

## 5.2 Data Sets and Sample Selection

The data used in this work is identical to that used in Chapters 2 – 4, i.e. the galaxies are selected from the ZFOURGE<sup>1</sup> catalogues (Straatman et al., 2016) and AGN are identified by cross-matching to radio, X-ray and infrared (IR) datasets. We limit our sample to 327 actively accreting (radiatively efficient) IR and X-ray AGN over  $z = 1.0 - 3.2$ . This redshift range is motivated by the IR-AGN selection criteria, which is reliant on IRAC (4.5 and 8.0  $\mu\text{m}$ ) and MIPS (24  $\mu\text{m}$ ) photometry (see Chapter 2). While alternative criteria are available to select IR-AGN at  $z < 1.0$ , we limit the redshift to avoid degeneracy effects.

## 5.3 Methodology

To isolate the AGN contribution to the observed SED, we apply an approach that requires only two photometric bands: *Spitzer*-MIPS 24  $\mu\text{m}$  and *Herschel*-PACS 160  $\mu\text{m}$ . The approach is reliant on the assumption that the observed 160  $\mu\text{m}$  flux for each source is pure stellar emission. As detailed in Chapter 2, this regime is considered predominantly immune from the effects of AGN contamination (e.g. Netzer et al., 2007; Santini et al., 2012; Mullaney et al., 2012a). We use the observed 160  $\mu\text{m}$  flux of a source as an estimate of its SFR. We then use the Wuyts et al. (2008) average star-forming galaxy (SFG) SED template to determine the expected 24  $\mu\text{m}$  flux from star formation. The difference between the observed 24  $\mu\text{m}$  and the expected 24  $\mu\text{m}$  for each source is assumed to be driven by AGN emission. For 160  $\mu\text{m}$  non-detections ( $< 1\sigma$ ), we assume all 24  $\mu\text{m}$  emission is due to AGN. We then normalise an AGN SED template to a 24  $\mu\text{m}$  flux value equal to this excess, de-redshift the template and calculate the rest-frame 8 – 1000  $\mu\text{m}$  luminosity or  $L_{\text{IR,AGN}}$ .

Given our sample is infrared-bright from dusty torus emission, we generate our AGN SED template from the AGN torus models of Siebenmorgen et al. (2015). From this suite of 3,600 templates, we construct an average template by first assuming a mid-point viewing angle of  $43^\circ$  and then taking the average of all other model parameters, including radius, cloud optical depth, and cloud filling factor. The average AGN template, along with the  $3\sigma$  uncertainty associated with the scatter from averaging model parameters, is shown in Figure 5.1.

---

<sup>1</sup><http://zfourge.tamu.edu>



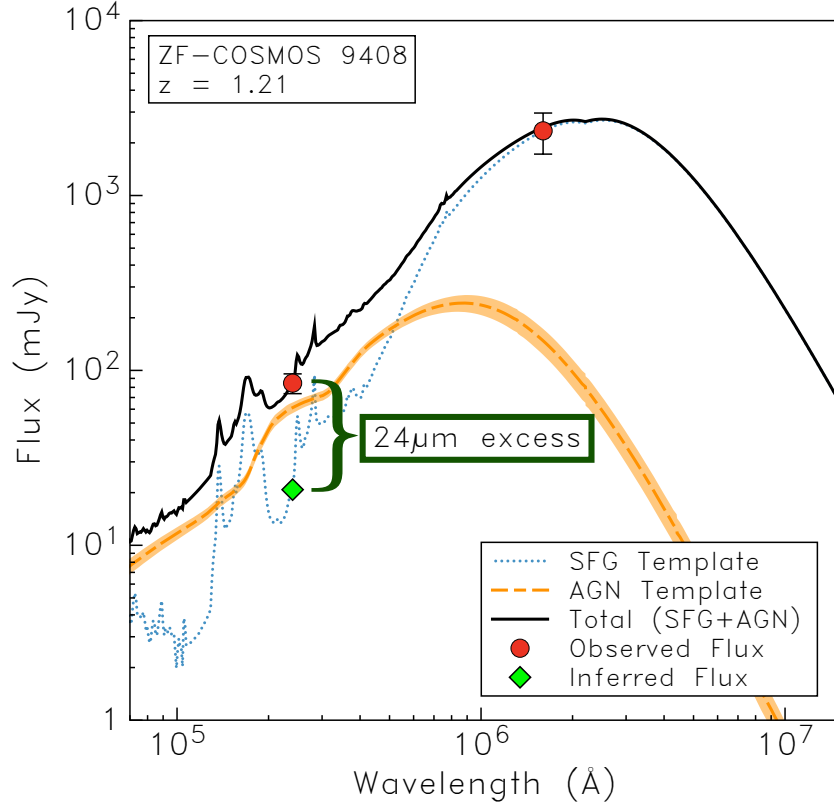


**Fig. 5.1** An example of the average AGN template with  $3\sigma$  uncertainty regions (dashed line), SFG template (dotted line) and corresponding total (i.e. AGN+SFG) SED (solid line) used to estimate  $L_{\text{IR,AGN}}$ . The red circles show the observed 24 and 160  $\mu\text{m}$  flux, while the green diamond shows the expected 24  $\mu\text{m}$  flux from stellar emission. The difference between the observed and expected 24  $\mu\text{m}$  fluxes gives us an estimate on the excess 24  $\mu\text{m}$  flux due to AGN emission, which we use to determine  $L_{\text{IR,AGN}}$ .

### Validation of Methodology

For validating our approach, we use the average SFG and AGN templates to generate a sample of 10,000 mock infrared SEDs. We begin by normalising both templates to 10,000 uncorrelated luminosities, randomly drawn from the typical luminosity ranges, and then sum both to produce a total (i.e. SFG+AGN) SED. Using *Spitzer*-MIPS and *Herschel*-PACS transmission curves, we then estimate the 24  $\mu\text{m}$  and 160  $\mu\text{m}$  fluxes in their respective passbands and add random noise that is consistent with observed flux errors (i.e. higher noise at lower fluxes). We then apply our approach to recover the  $L_{\text{IR,AGN}}$  and 160  $\mu\text{m}$ -derived  $L_{\text{IR,SF}}$  (SFR).

The results of this test are presented in Figure 5.2 and reveal the recovered SFRs and AGN luminosities to be weakly correlated ( $R \sim 0.4$ ). This correlation is driven by a lack of sources with low  $L_{\text{IR,SF}}$  and high  $L_{\text{IR,AGN}}$  luminosities (bottom-right of Figure 5.2), and

those with high  $L_{\text{IR,SF}}$  and low  $L_{\text{IR,AGN}}$  luminosities (top-left of Figure 5.2). We postulate the lack of sources in the top-left with low  $L_{\text{IR,AGN}}$  is a selection effect resulting from our use of radiatively efficient (i.e. luminous) AGN. We explore this in more detail in Section 5.4. For sources in the bottom-right, an examination of their SEDs reveals they are AGN-dominated with contamination at FIR wavelengths. This ultimately yields higher than expected  $160\text{ }\mu\text{m}$  flux recoveries and is more prevalent at higher redshifts where the observed  $160\text{ }\mu\text{m}$  begins to probe lower rest-frame wavelengths. While at lower redshifts, the FIR regime is largely impervious to AGN contamination (Netzer et al., 2007), at  $z \sim 3$  our simulations suggest it can be as high as 22% for AGN dominated ( $> 50\%$  AGN) sources. Given this, we consider the effect of contamination by defining an AGN-dominated region, which we illustrate in Figure 5.3. In this area, our simulations fail to adequately apply our approach as the SF, derived from  $160\text{ }\mu\text{m}$  fluxes, is considered contaminated by AGN emission.

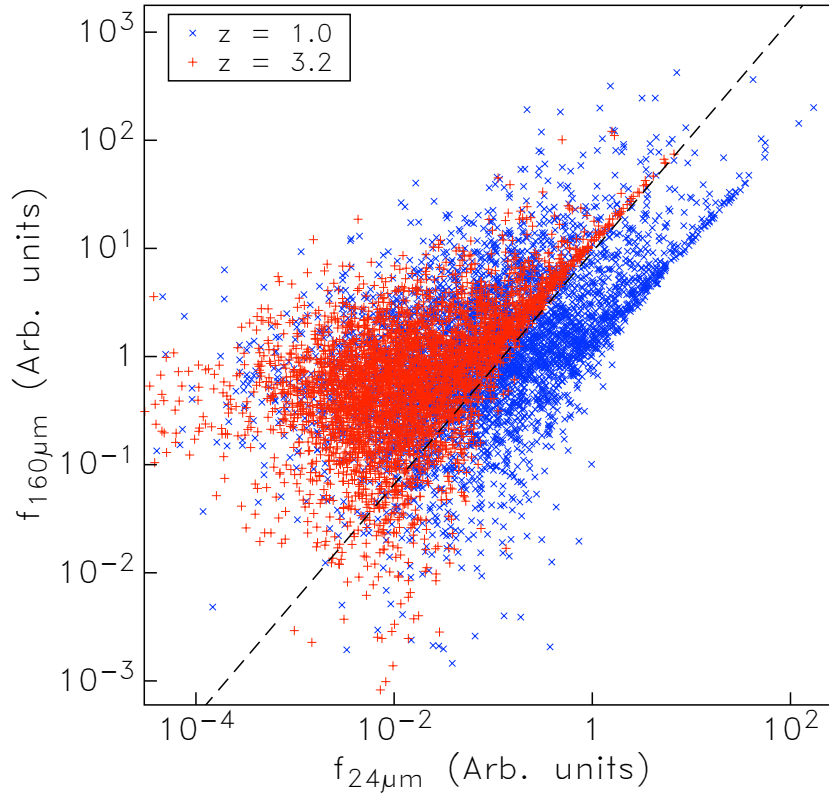


**Fig. 5.2** An example of the recovered  $24\text{ }\mu\text{m}$  and  $160\text{ }\mu\text{m}$  fluxes from our simulation of 10,000 mock infrared SEDs. The blue cross markers represent the recovered fluxes from a simulation run at low redshift ( $z = 1.0$ ), while the red tick markers represent a run at high redshift ( $z = 3.2$ ). A distinct hard edge can be seen, which results from AGN contamination to the  $160\text{ }\mu\text{m}$  flux in our approach. We mark the highest redshift edge with a dashed line and use it to define an AGN-dominated region in our analysis.

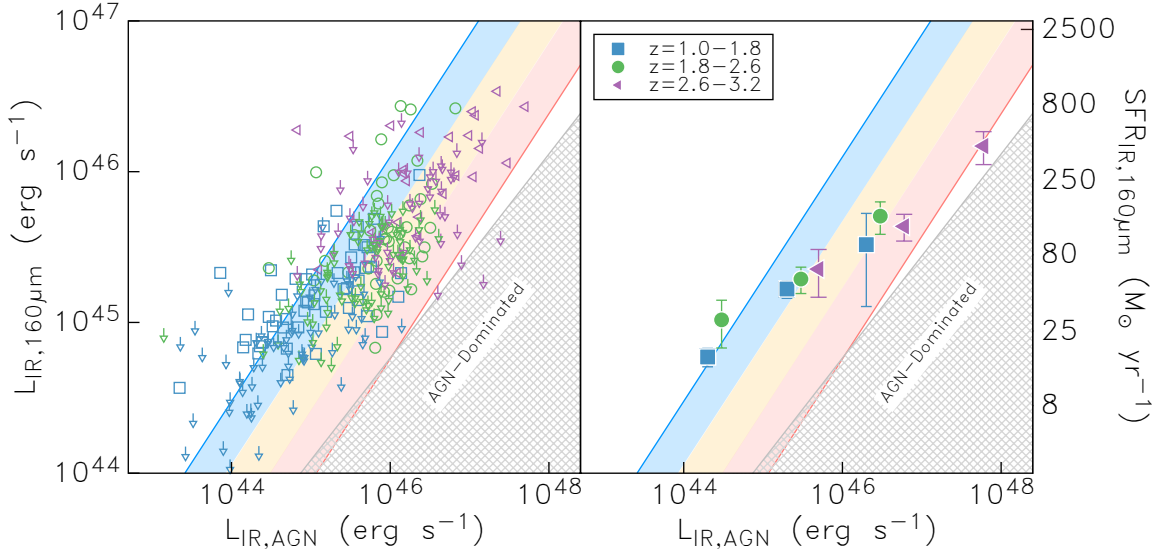


**Fig. 5.3** IR luminosity due to star formation,  $L_{\text{IR,SF}}$ , as a function of the infrared-derived AGN luminosity,  $L_{\text{AGN,IR}}$ . We also give the corresponding SFR values. We plot all sources (left) at  $z = 1.0 - 1.8$  (blue squares),  $z = 1.8 - 2.6$  (green circles) and  $z = 2.6 - 3.2$  (purple triangles). Sources with  $< 3\sigma$  detection at  $160\ \mu\text{m}$  are given  $3\sigma$  upper limits (arrows). We also bin the mean  $L_{\text{IR,SF}}$  and  $L_{\text{AGN,IR}}$  (right). Error bars correspond to 1-sigma confidence limits and were determined by bootstrap resampling. The hatched area represents the region  $160\ \mu\text{m}$ -derived SFRs begin to be contaminated by AGN. The three-colour shaded area shows the AGN contribution to the SED derived by Gruppioni et al. (2016) at  $> 70$  per cent (red),  $30 - 70$  per cent (yellow), and  $< 30$  per cent (blue).

### 5.3.1 Results

The results of our analysis are presented in Figure 5.3. In this figure, we split sources into three redshift bins,  $z = [1.0 - 1.8]$ ,  $[1.8 - 2.6]$ ,  $[2.6 - 3.2]$ . For each redshift bin, we also divide the sample into equal  $L_{\text{IR,AGN}}$  bins. For each of these  $z$ - $L_{\text{IR,AGN}}$  bins, we calculate the mean luminosity due to star formation,  $L_{\text{IR,SF}}$ . Of the 327 AGN-dominated sources inspected, only 117 (i.e.  $\sim 36\%$ ) are detected at  $> 3\sigma$  at  $160\ \mu\text{m}$ . To ensure our results are not biased against galaxies with low SFRs, we consider all sources when calculating the mean SFR, including those with zero or negative  $160\ \mu\text{m}$  fluxes (i.e. upper limits are not considered when calculating overall mean). These values are tabulated in Table 5.1.

Calculating the Pearson correlation coefficient, we find that  $L_{\text{IR,SF}}$  and  $L_{\text{IR,AGN}}$  for the whole sample to be correlated with an R-value of 0.75. The mean  $L_{\text{IR,SF}}$  (and hence mean SFR), increases monotonically with  $L_{\text{IR,AGN}}$  and exhibits a factor of  $\sim 10$  difference between the the highest and lowest  $L_{\text{IR,AGN}}$  bins. We find this correlation has no dependence on redshift, with each bin exhibiting a slope of  $L_{\text{IR,SF}} \propto (L_{\text{IR,AGN}})^{0.5}$  across our full redshift range,  $z = 1.0 - 3.2$ . A similar correlation between  $L_{\text{IR,SF}}$  and  $L_{\text{IR,AGN}}$  has been found in the

literature. We plot the findings of Gruppioni et al. (2016) in Figure 5.3, who investigated a sample of local AGN and found a slope of  $L_{\text{IR,SF}} \propto (L_{\text{IR,AGN}})^{0.8}$ .

**Table 5.1** Mean  $L_{\text{IR,SF}}$  and SFRs for the data presented in Fig. 5.2

Redshift	$L_{\text{IR,AGN}}$ ( $\text{erg s}^{-1}$ )	$\langle L_{\text{IR,SF}} \rangle$ ( $\text{erg s}^{-1}$ )	$\langle \text{SFR} \rangle$ ( $M_{\odot} \text{yr}^{-1}$ )	$N_{\text{AGN}}^2$
$z = 1.0 - 1.8$	$10^{44-45}$	$5.9 \pm 0.8 \times 10^{44}$	$17 \pm 2$	58
	$10^{45-46}$	$1.7 \pm 0.2 \times 10^{45}$	$47 \pm 6$	47
	$10^{46-47}$	$3.3 \pm 2.0 \times 10^{45}$	$93 \pm 57$	4
	$10^{47-48}$	-	-	0
$z = 1.8 - 2.6$	$10^{44-45}$	$1.0 \pm 0.4 \times 10^{45}$	$30 \pm 10$	10
	$10^{45-46}$	$1.9 \pm 0.4 \times 10^{45}$	$55 \pm 11$	70
	$10^{46-47}$	$5.1 \pm 1.2 \times 10^{45}$	$144 \pm 35$	39
	$10^{47-48}$	-	-	0
$z = 2.6 - 3.2$	$10^{44-45}$	-	-	0
	$10^{45-46}$	$2.3 \pm 0.8 \times 10^{45}$	$64 \pm 22$	29
	$10^{46-47}$	$4.3 \pm 0.9 \times 10^{45}$	$124 \pm 25$	43
	$10^{47-48}$	$1.5 \pm 0.4 \times 10^{46}$	$421 \pm 104$	10

<sup>1</sup> Number of AGN hosts within the specified limits

## 5.4 Discussion and Summary

Using a new approach to isolate the AGN component from of a galaxy's SED, we have investigated the relationship between the mean 160  $\mu\text{m}$ -derived SFRs and AGN luminosity for 327 IR-bright active galaxies out to  $z = 3.2$ . While our results are consistent with the literature and reveal a possible connection between star formation and AGN activity in IR-bright active galaxies, we identify factors that suggest selection effects drive this, which complicates the interpretation of our observations.

In Figure 5.3, the hatched section represents the AGN-dominated region derived in Section 5.3. It becomes evident that the correlation observed between the SFR and AGN luminosity closely follows the edge of this region at high luminosities. In other words, we cannot rule out this trend is caused by our inability to identify galaxies with low star formation and high AGN luminosity. Furthermore, our reliance on IR-selected AGN means

our observational data likely leads to a lack of high-SFR, low-AGN objects. Indeed, when we perform a full SED decomposition (see Chapter 4) on the same sample using the multi-component SED fitting code, CIGALE<sup>2</sup> (Code Investigating GALaxy Emission; Burgarella et al., 2005; Noll et al., 2009), we find these very sources to be lacking in our IR-selected AGN (see the right panel of Figure 5.4).

While these selection effects inhibit our ability to directly confirm a positive correlation, the trends we observe are consistent with recent infrared studies that have used SED fitting and decomposition to estimate SFRs and bolometric AGN luminosities. For example, Gruppioni et al. (2016) decompose the SEDs of 76 sources from the local 12  $\mu\text{m}$  sample of Seyfert galaxies (12MGS). They find their IR-derived AGN luminosity to be in good agreement with other estimators (e.g. X-ray luminosity) and positively correlate with their SFR estimations. Heinis et al. (2016), on the other hand, take a unique approach by selecting  $\sim 1000$  AGN by variability, which is another approach to overcome the issue of selection bias against heavily obscured and low luminosity AGN. Using SED fitting, they recover the monochromatic continuum luminosity at 5100  $\text{\AA}$  as a measure of AGN power and also find it correlates positively with their SFRs. While similar investigations at high- $z$  ( $z \sim 2 - 3$ ) have been limited, they too produce a correlation of  $L_{\text{IR,SF}} \propto (L_{\text{IR,AGN}})^{0.7}$  (Shao et al., 2010; Rosario et al., 2012). However, this correlation is limited to AGN-dominated sources, where  $L_{\text{IR,AGN}} > L_{\text{IR,SF}}$ . Indeed, if we limit our sources to the same, we find a tighter correlation ( $R = 0.8$ ) with a similar slope of 0.7.

Despite these findings, our initial simulations show that selection effects (ie. biases against both low-SFR and low-AGN) plausibly might explain prior work and call into question whether there is a relationship between SF and AGN for typical IR-bright AGN galaxies.

## 5.5 Summary and Future Work

The large amounts of data required to perform analyses, such as the one presented here, tend to limit such studies to low redshifts ( $z \lesssim 1$ ). Our technique, coupled with the high-quality photometric redshifts of ZFOURGE, has allowed us to extend this investigation out to higher redshifts and with fewer wavebands.

While the interim results are promising, additional work is required to further validate our new approach. For example, in the case of no 160  $\mu\text{m}$  detection, we currently assume all 24  $\mu\text{m}$  emission is AGN. Strictly speaking, this should be considered an upper limit. Furthermore, when we perform a direct comparison of the recovered AGN luminosity for

---

<sup>2</sup><http://cigale.lam.fr>

individual sources, using CIGALE and the approach detailed in Chapter 4, Figure 5.4 reveals there is no measurable intrinsic scatter, but clearly a lot of scatter due to uncertainties primarily from the 160  $\mu\text{m}$  observations. Our approach also appears to be overestimating values when compared to a full SED decomposition. This may explain why our sources exhibit a shallower slope between  $L_{\text{IR,SF}}$  and  $L_{\text{IR,AGN}}$  compared to the literature. By completing more robust tests, it is hoped the approach can be fine-tuned before offering it as a valuable tool to astronomers wishing to complete similar studies, but are limited by their available datasets.

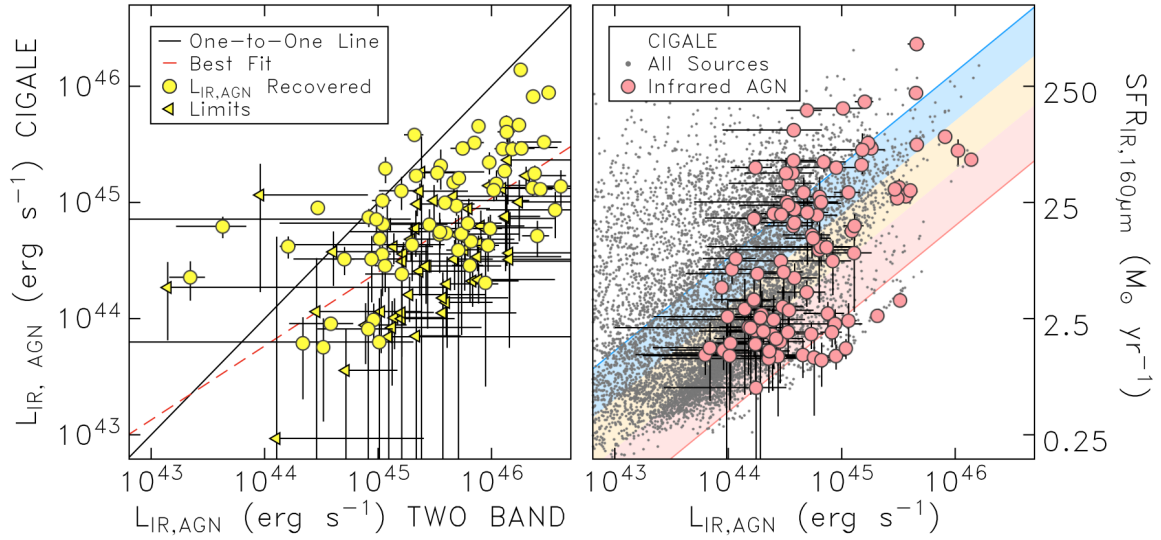


**Fig. 5.4** *Left panel:* Comparison of the AGN luminosity ( $L_{\text{IR,AGN}}$ ) recovered by CIGALE and the two band approach presented here for radiatively efficient AGN in ZFOURGE. Errors are propagated from the flux errors in ZFOURGE. Non-detections at 160  $\mu\text{m}$  are given upper limits (left-facing arrows). The dashed line is the best fit, which returns a Pearson correlation coefficient,  $R$  of 0.7.

*Right panel:* SFR as a function of the infrared-derived AGN luminosity from CIGALE for all sources in ZFOURGE over  $z = 1 - 3.2$ . IR-selected AGN are shown as red markers. Errors are derived by CIGALE during the fitting process. Similar to the findings of the methodology presented here, CIGALE reveals IR-selected AGN to exhibit a positive correlation with a distinct lack of low-SFR, high-AGN sources and high-SFR, low-AGN sources.

# Chapter 6

## Conclusions and Future Work

The work contained in this thesis investigates the connection between galaxies and their supermassive black holes by using rich galaxy catalogues, multi-wavelength AGN identification techniques, and the latest approaches to parameterise galaxy and AGN properties. It advances on previous work by applying new analyses to a more substantial number of sources, with higher quality photometric redshifts, over a broader redshift range, and down to deeper mass-limits than most studies before it. In Chapter 1, we discussed the physical and observational properties of SMBHs, and reviewed how those that are actively accreting may impact the evolution of their host galaxy. We also provided a brief overview of the various surveys and facilities used in this thesis, most notably the ZFOURGE survey, whose data forms the backbone of this work. In Chapter 2, we supplemented ZFOURGE with broadband ancillary photometry, which allowed us to apply new multi-wavelength techniques to uniformly select AGN in ZFOURGE. In this chapter, we summarise the results presented in the remaining chapters and discuss ongoing and future work that aims to continue addressing the outstanding questions relating to the co-evolution of galaxies and supermassive black holes.

### 6.1 An Enhancement of Star Formation in AGN Hosts

In Chapter 3, we compared 225 AGN host galaxies across  $z = 0.2 - 3.2$  to a sample of mass-matched inactive (non-AGN) sources. Careful consideration of AGN contamination was made, while selection bias was minimised by limiting our selection to a stellar-mass cut of  $\log(M_*/M_\odot) \geq 9.75$  with varying AGN luminosity limits based on the thresholds of their respective wavebands (i.e.  $L_{1.4\text{GHz}}$ ,  $L_X$  and  $L_{\text{IR}}$ ). A *UVJ* analysis revealed the colour of radio, X-ray and IR-selected AGN hosts are consistent with distinct galaxy populations, with IR-selected AGN favouring star-forming galaxies, radio-selected AGN favouring quiescent

galaxies, and X-ray-selected AGN straddling between the two. However, this distinction was blurred at higher redshifts ( $z \gtrsim 1.8$ ), where we found all AGN to favour star-forming hosts. Our *UVJ* analysis also revealed our sample of AGN to exhibit a higher dusty star-former fraction and lower quiescent fraction compared to the control sample. This observation was supported by the star formation activity of the AGN hosts, where we found their mean sSFR to be elevated over the non-AGN hosts. The only exception to this was radio-selected AGN at low redshifts ( $z < 0.8$ ), which are known to be hosted in giant, quenched ellipticals. While we only postulated to the reasons for the elevated star formation in these AGN hosts, the results cast doubt on the idea that AGN are the dominant quenching mechanism throughout most of cosmic time.

## 6.2 Decoupled Black Hole Accretion and Quenching

In Chapter 4, we tracked the evolution of the relative black hole-galaxy growth (i.e. their BHAR/SFR ratio) and quenching rate for Milky Way and Andromeda-mass progenitors from  $z = 0.2 - 2.5$ . To estimate the BHARs, we used the decomposition software, CIGALE to split the observed SEDs of our galaxies to isolate the AGN component. As the progenitors evolve, we found a disconnect between the BHAR/SFR ratios and the quenching rate, and also between the BHARs and SFRs themselves. Specifically, we found the redshift evolution of the logarithm of the BHAR/SFR ratios of the Milky Way progenitors to exhibit a slope of  $0.64 \pm 0.11$ , while the Andromeda progenitors were  $0.39 \pm 0.08$ , suggesting a disconnect between SF and black hole accretion. This result contrasts with previous studies that find a correlation when adopting X-ray/AGN-selected or mass-limited samples and is likely due to their use of a broad mixture of galaxies with different evolutionary histories. Our use of progenitor-matched samples highlights the potential importance of carefully selecting progenitors when searching for evolutionary relationships between BHAR/SFRs. Furthermore, the results of this chapter continue to cast doubt on the idea that AGN are the dominant quenching mechanism throughout most of cosmic time.

## 6.3 A Two Band Approach to Isolate the AGN Contribution to Observed SEDs

In Chapter 5, we presented a technique to isolate the AGN contribution to the observed SED using only two photometric bands. Such an approach lends itself to studies where abundant photometric data may be lacking. We demonstrated our approach can reproduce the SF-AGN



correlation found in infrared-selected AGN; however, we highlighted selection-bias, the same as discussed in Chapter 4, may be driving the trends observed here. While robust tests reveal our approach is not without limitations, we envisage that in time, it will lend itself to other studies where abundant photometric data may be lacking, offering them an alternative to full SED decomposition.

## 6.4 Ongoing and Future Work

The work in this thesis presents new, multi-wavelength AGN catalogues spanning most of cosmic time, and work in progress towards a new technique to isolate the AGN contribution to a galaxy's SED using minimal data. Using these resources, our analyses have added significant evidence to the suggestion that the correlations observed between SMBHs and their host galaxies may be driven by selection effects, while also casting doubts over the idea that the suppression of SF is predominantly driven by the negative feedback of luminous AGN. However, an important caveat to consider is that this work focuses on average galaxy trends. Short time-scale variations in mass accretion rates have been shown to wash out underlying correlations between SFR and  $L_{\text{AGN}}$  (Stanley et al., 2015). It could be that short phases of strong AGN feedback do occur in individual galaxies (and are present in our sample), but their impact is not noticeable due to our focus on general trends.

While there remains much to learn about the complex interactions between SMBHs and their hosts, the outlook for such research appears promising. In the coming years, new facilities, such as the James Webb Space Telescope (Gardner et al., 2006) and the Giant Magellan Telescope (Johns et al., 2012), will revolutionise research in the field. However, existing observations and technology can still contribute significantly as well. As a case in point, we outline a work in progress below, which would make a valuable follow-up project to this thesis.

### 6.4.1 The Impact of Low-Luminosity AGN on their Hosts

At the start of this thesis, we applied various photometric-based selection techniques to identify luminous AGN at high redshifts. As shown in Chapter 5, low-luminosity AGN (LLAGN) are often overlooked at high redshift; however, it is possible they far outnumber luminous AGN (Ptak, 2002) making them potentially more relevant to our understanding of the co-evolution of SMBHs and their host galaxies. To that end, we plan to supplement the multi-wavelength AGN catalogues presented here with optical spectra from the ZFIRE survey to select LLAGN using optical diagnostics such as the BPT (Baldwin et al., 1981),

MEx (mass-excitation; Juneau et al., 2011), and CEx (colour-excitation; Yan et al., 2011) optical diagnostic diagrams.

ZFIRE is a near-IR survey taken with the MOSFIRE multi-object spectrograph on the Keck I telescope (Nanayakkara et al., 2016). Its advantage over other similar near-IR surveys (e.g. KBSS; Steidel et al. 2014, MOSDEF; Kriek et al. 2015 or KMOS-3D; Wisnioski et al. 2015) is it spans both cluster and field environments. By combining its data with multi-wavelength observations of ZFOURGE, ZFIRE tracks the star formation histories, ISM conditions, and kinematic scaling relations of galaxies and their dependence on environment.

By combining the AGN catalogues of ZFOURGE and ZFIRE, we hope to better constrain the physical mechanisms that led to present-day galaxies and SMBHs. Reconstructing the history of galaxies from their earliest appearance to the present contributes to important empirical constraints to cosmology. Such work addresses an area that has previously been limited by observational constraints. Therefore, the significance of such a project is not only centred on the co-evolution of SMBHs and their host galaxies, but advancing our theory on the evolution of the Universe as a whole.

# References

- Abramowicz, M. A., Czerny, B., Lasota, J. P., & Szuszkiewicz, E. 1988, *The Astrophysical Journal*, 332, 646
- Aird, J., Nandra, K., Laird, E. S., et al. 2010, *Monthly Notices of the Royal Astronomical Society*, 401, 2531
- Alexander, D. M., & Hickox, R. C. 2012, *New Astronomy Reviews*, 56, 93
- Antonucci, R. 1993, *Annual Review of Astronomy and Astrophysics*, 31, 473
- Antonucci, R. R. J., & Miller, J. S. 1985, *The Astrophysical Journal*, 297, 621
- Azadi, M., Aird, J., Coil, A. L., et al. 2015, *The Astrophysical Journal*, 806, 187
- Baade, W., & Minkowski, R. 1954, *The Astrophysical Journal*, 119, 215
- Baldwin, J. A., Phillips, M. M., & Terlevich, R. 1981, *Publications of the Astronomical Society of the Pacific*, 93, 5
- Barger, A. J., Cowie, L. L., Owen, F. N., et al. 2015, *The Astrophysical Journal*, 801, 87
- Barmby, P., Alonso-Herrero, A., Donley, J. L., et al. 2006, *The Astrophysical Journal*, 642, 126
- Barnes, J. E., & Hernquist, L. E. 1991, *The Astrophysical Journal*, 370, L65
- Begelman, M. C. 1979, *Monthly Notices of the Royal Astronomical Society*, 187, 237
- Begelman, M. C., Volonteri, M., & Rees, M. J. 2006, *Monthly Notices of the Royal Astronomical Society*, 370, 289
- Beifiori, A., Courteau, S., Corsini, E. M., & Zhu, Y. 2011, *Monthly Notices of the Royal Astronomical Society*, 419, 2497
- Bell, E. F. 2003, *The Astrophysical Journal*, 586, 794
- Bell, E. F., Papovich, C., Wolf, C., et al. 2005, *The Astrophysical Journal*, 625, 23
- Bernhard, E., Mullaney, J. R., Daddi, E., Ciesla, L., & Schreiber, C. 2016, *arXiv.org*, 1604.06455
- Böhringer, H., Matsushita, K., Churazov, E., Ikebe, Y., & Chen, Y. 2002, *Astronomy & Astrophysics*, 382, 804

- Bongiorno, A., Merloni, A., Brusa, M., et al. 2013, *Monthly Notices of the Royal Astronomical Society*, 427, 3103
- Bonoli, S., Mayer, L., & Callegari, S. 2014, *Monthly Notices of the Royal Astronomical Society*, 437, 1576
- Boyle, & Terlevich, R. J. 1998, *Monthly Notices of the Royal Astronomical Society*, 293, L49
- Brammer, G. B., Van Dokkum, P. G., & Coppi, P. 2008, *The Astrophysical Journal*, 686, 1503
- Brammer, G. B., Van Dokkum, P. G., Franx, M., et al. 2012, *The Astrophysical Journal Supplement*, 200, 13
- Brandl, B. R., Bernard Salas, J., Spoon, H. W. W., et al. 2006, *The Astrophysical Journal*, 653, 1129
- Bruzual, G., & Charlot, S. 2003, *Monthly Notices of the Royal Astronomical Society*, 344, 1000
- Buat, V., Heinis, S., Boquien, M., et al. 2013, *Astronomy & Astrophysics*, 561, A39
- Burgarella, D., Buat, V., & Iglesias-Páramo, J. 2005, *Monthly Notices of the Royal Astronomical Society*, 360, 1413
- Burgarella, D., Buat, V., Gruppioni, C., et al. 2013, *Astronomy & Astrophysics*, 554, A70
- Calhau, J., Sobral, D., Stroe, A., et al. 2017, *Monthly Notices of the Royal Astronomical Society*, 464, 303
- Calzetti, D., Armus, L., Bohlin, R. C., et al. 2000, *The Astrophysical Journal*, 533, 682
- Ceverino, D., Dekel, A., & Bournaud, F. 2010, *Monthly Notices of the Royal Astronomical Society*, 404, 2151
- Chabrier, G. 2003, *Publications of the Astronomical Society of the Pacific*, 115, 763
- Chen, C.-T. J., Hickox, R. C., Alberts, S., et al. 2013, *The Astrophysical Journal*, 773, 3
- Chiao, R. Y., & Wickramasinghe, N. C. 1972, *Monthly Notices of the Royal Astronomical Society*, 159, 361
- Ciesla, L., Charmandaris, V., Georgakakis, A., et al. 2015, *Astronomy & Astrophysics*, 576, A10
- Ciotti, L., & Ostriker, J. P. 1997, *The Astrophysical Journal*, 487, L105
- Cirasuolo, M., Celotti, A., Magliocchetti, M., & Danese, L. 2003, *Monthly Notices of the Royal Astronomical Society*, 346, 447
- Cisternas, M., Jahnke, K., Bongiorno, A., et al. 2011, *The Astrophysical Journal Letters*, 741, L11

- Clements, D. L., Sutherland, W. J., McMahon, R. G., & Saunders, W. 1996, *Monthly Notices of the Royal Astronomical Society*, 279, 477
- Comastri, A., Setti, G., Zamorani, G., & Hasinger, G. 1995, *Astronomy & Astrophysics*, 296, 1
- Condon, J. J., Cotton, W. D., & Broderick, J. J. 2002, 124, 675
- Conselice, C. J., Mortlock, A., Bluck, A. F. L., Grützbauch, R., & Duncan, K. 2013, *Monthly Notices of the Royal Astronomical Society*, 430, 1051
- Costa, T., Sijacki, D., & Haehnelt, M. G. 2014, *Monthly Notices of the Royal Astronomical Society*, 444, 2355
- Crockett, R. M., Shabala, S. S., Kaviraj, S., et al. 2012, *Monthly Notices of the Royal Astronomical Society*, 421, 1603
- Croft, S., van Breugel, W., de Vries, W., et al. 2006, *The Astrophysical Journal*, 647, 1040
- Croton, D. J., Springel, V., White, S. D. M., et al. 2006, *Monthly Notices of the Royal Astronomical Society*, 365, 11
- Dai, Y. S., Wilkes, B. J., Bergeron, J., et al. 2015, eprint arXiv:1511.06761, 1511.06761
- Dale, D. A., & Helou, G. 2002, *The Astrophysical Journal*, 576, 159
- Dale, D. A., Helou, G., Magdis, G. E., et al. 2014, *The Astrophysical Journal*, 784, 83
- de Graauw, T., Helmich, F. P., Phillips, T. G., et al. 2010, *Astronomy & Astrophysics*, 518, L6
- Dekel, A., & Silk, J. 1986, *The Astrophysical Journal*, 303, 39
- Delvecchio, I., Gruppioni, C., Pozzi, F., et al. 2014, *Monthly Notices of the Royal Astronomical Society*, 439, 2736
- Di Matteo, P., Bournaud, F., Martig, M., et al. 2008, *Astronomy & Astrophysics*, 492, 31
- Di Matteo, T., Springel, V., & Hernquist, L. 2005, *Nature*, 433, 604
- Donley, J. L., Rieke, G. H., Pérez-González, P. G., Rigby, J. R., & Alonso-Herrero, A. 2007, *The Astrophysical Journal*, 660, 167
- Donley, J. L., Rieke, G. H., Rigby, J. R., & Pérez-González, P. G. 2005, *The Astrophysical Journal*, 634, 169
- Donley, J. L., Koekemoer, A. M., Brusa, M., et al. 2012, *The Astrophysical Journal*, 748, 142
- Eckart, M. E., McGreer, I. D., Stern, D., Harrison, F. A., & Helfand, D. J. 2009, *The Astrophysical Journal*, 708, 584
- Elbaz, D., Jahnke, K., Pantin, E., Le Borgne, D., & Letawe, G. 2009, *Astronomy & Astrophysics*, 507, 1359

- Elbaz, D., Dickinson, M., Hwang, H. S., et al. 2011, *Astronomy & Astrophysics*, 533, A119
- Elitzur, M., & Ho, L. C. 2009, *The Astrophysical Journal*, 701, L91
- Ellison, S. L., Patton, D. R., & Hickox, R. C. 2015, *Monthly Notices of the Royal Astronomical Society: Letters*, 451, L35
- Elvis, M., Civano, F., Vignali, C., et al. 2009, *The Astrophysical Journal Supplement*, 184, 158
- Erb, D. K., Pettini, M., Shapley, A. E., et al. 2010, *The Astrophysical Journal*, 719, 1168
- Esin, A. A., Narayan, R., Ostriker, E., & Yi, I. 1996, *The Astrophysical Journal*, 465, 312
- Fabian, A. C. 2012, *Annual Review of Astronomy and Astrophysics*, 50, 455
- Fabian, A. C., Celotti, A., & Erlund, M. C. 2006, *Monthly Notices of the Royal Astronomical Society*, 373, L16
- Faucher-Giguère, C.-A., & Quataert, E. 2012, *Monthly Notices of the Royal Astronomical Society*, 425, 605
- Fazio, G. G., Hora, J. L., Allen, L. E., et al. 2004, *The Astrophysical Journal Supplement*, 154, 10
- Ferrarese, L., & Merritt, D. 2000, *The Astrophysical Journal*, 539, L9
- Feruglio, C., Maiolino, R., Piconcelli, E., et al. 2010, *Astronomy & Astrophysics*, 518, L155
- Fioc, M., & Rocca-Volmerange, B. 1997, *Astronomy & Astrophysics*, 326, 950
- Fischer, J., Sturm, E., González-Alfonso, E., et al. 2010, *Astronomy & Astrophysics*, 518, L41
- Forman, W., Jones, C., Churazov, E., et al. 2007, *The Astrophysical Journal*, 665, 1057
- Freeman, K., & Bland-Hawthorn, J. 2002, *Annual Review of Astronomy and Astrophysics*, 40, 487
- Fritz, J., Franceschini, A., & Hatziminaoglou, E. 2006, *Monthly Notices of the Royal Astronomical Society*, 366, 767
- Fumagalli, M., Labbé, I., Patel, S. G., et al. 2014, *The Astrophysical Journal*, 796, 35
- Gabor, J. M., & Bournaud, F. 2014, *Monthly Notices of the Royal Astronomical Society*, 441, 1615
- García-Burillo, S., Combes, F., Schinnerer, E., Boone, F., & Hunt, L. K. 2005, *Astronomy & Astrophysics*, 441, 1011
- Gardner, J. P., Mather, J. C., Clampin, M., et al. 2006, *Space Science Reviews*, 123, 485
- Garmire, G. P., Bautz, M. W., Ford, P. G., et al. 2003, in *X-Ray and Gamma-Ray Telescopes and Instruments for Astronomy*, ed. J. E. Truemper & H. D. Tananbaum (SPIE), 28

- Gebhardt, K., Bender, R., Bower, G., et al. 2000, *The Astrophysical Journal*, 539, L13
- Genel, S., Dekel, A., & Cacciato, M. 2012, *Monthly Notices of the Royal Astronomical Society*, 425, 788
- Genzel, R., Förster Schreiber, N. M., Lang, P., et al. 2014, *The Astrophysical Journal*, 785, 75
- Giacconi, R., Zirm, A., Wang, J., et al. 2002, *The Astrophysical Journal Supplement*, 139, 369
- Gilli, R., Comastri, A., & Hasinger, G. 2007, *Astronomy & Astrophysics*, 463, 79
- Gilli, R., Salvati, M., & Hasinger, G. 2001, *Astronomy & Astrophysics*, 366, 407
- Goulding, A. D., Forman, W. R., Hickox, R. C., et al. 2012, *The Astrophysical Journal Supplement*, 202, 6
- . 2014, *The Astrophysical Journal*, 783, 40
- Graham, A. W. 2007, *Monthly Notices of the Royal Astronomical Society*, 379, 711
- Graham, A. W., Onken, C. A., Athanassoula, E., & Combes, F. 2011, *Monthly Notices of the Royal Astronomical Society*, 412, 2211
- Griffin, M. J., Abergel, A., Abreu, A., et al. 2010, *Astronomy & Astrophysics*, 518, L3
- Grogin, N. A., Kocevski, D. D., Faber, S. M., et al. 2011, *The Astrophysical Journal Supplement*, 197, 35
- Gruppioni, C., Pozzi, F., Zamorani, G., & Vignali, C. 2011, *Monthly Notices of the Royal Astronomical Society*, 416, 70
- Gruppioni, C., Berta, S., Spinoglio, L., et al. 2016, *Monthly Notices of the Royal Astronomical Society*, 458, 4297
- Gültekin, K., Richstone, D. O., Gebhardt, K., et al. 2009, *The Astrophysical Journal*, 698, 198
- Haan, S., Schinnerer, E., Emsellem, E., et al. 2009, *The Astrophysical Journal*, 692, 1623
- Haiman, Z., & Loeb, A. 2001, *The Astrophysical Journal*, 552, 459
- Hainline, K. N., Hickox, R., Greene, J. E., Myers, A. D., & Zakamska, N. L. 2013, *The Astrophysical Journal*, 774, 145
- Hainline, K. N., Hickox, R. C., Greene, J. E., et al. 2014, *The Astrophysical Journal*, 787, 65
- Häring, N., & Rix, H.-W. 2004, *The Astrophysical Journal*, 604, L89
- Harrison, C. M. 2016, *Observational Constraints on the Influence of Active Galactic Nuclei on the Evolution of Galaxies*, Springer Theses (Cham: Springer International Publishing), doi:10.1007/978-3-319-28454-5

- Harrison, C. M., Alexander, D. M., Mullaney, J. R., et al. 2012, *The Astrophysical Journal Letters*, 760, L15
- Harwit, M. 1962, *The Astrophysical Journal*, 136, 832
- Hasinger, G. 2008, *Astronomy & Astrophysics*, 490, 905
- Hasinger, G., Miyaji, T., & Schmidt, M. 2005, *Astronomy & Astrophysics*, 441, 417
- Hawkins, M. R. S. 2006, *Astronomy & Astrophysics*, 462, 581
- Heinis, S., Gezari, S., Kumar, S., et al. 2016, *The Astrophysical Journal*, 826, 62
- Heisler, C. A., & De Robertis, M. M. 1999, 118, 2038
- Helou, G., Soifer, B. T., & Rowan-Robinson, M. 1985, *The Astrophysical Journal*, 298, L7
- Hickox, R. C., Jones, C., Forman, W. R., et al. 2007, *The Astrophysical Journal*, 671, 1365
- . 2009, *The Astrophysical Journal*, 696, 891
- Ho, L. C. 2005, *The Astrophysical Journal*, 629, 680
- Hopkins, P. F., Hayward, C. C., Narayanan, D., & Hernquist, L. 2011, *Monthly Notices of the Royal Astronomical Society*, 420, 320
- Hopkins, P. F., Hernquist, L., Cox, T. J., et al. 2005, *The Astrophysical Journal*, 630, 705
- . 2006, *The Astrophysical Journal Supplement*, 163, 1
- Hopkins, P. F., Hernquist, L., Cox, T. J., & Kereš, D. 2008, *The Astrophysical Journal Supplement*, 175, 356
- Hopkins, P. F., & Quataert, E. 2010, *Monthly Notices of the Royal Astronomical Society*, 407, 1529
- Ivezić, Ž., Menou, K., Knapp, G. R., et al. 2002, *The Astronomical Journal*, 124, 2364
- Jansen, F., Lumb, D., Altieri, B., et al. 2001, *Astronomy & Astrophysics*, 365, L1
- Jogee, S. 2006, *Physics of Active Galactic Nuclei at all Scales*, 693, 143
- Johns, M., McCarthy, P., Raybould, K., et al. 2012, in *SPIE Astronomical Telescopes + Instrumentation*, ed. L. M. Stepp, R. Gilmozzi, & H. J. Hall (SPIE), 84441H
- Juneau, S., Dickinson, M., Alexander, D. M., & Salim, S. 2011, *The Astrophysical Journal*, 736, 104
- Juneau, S., Dickinson, M., Bournaud, F., et al. 2013, *The Astrophysical Journal*, 764, 176
- Kaiser, C. R., Schoenmakers, A. P., & Röttgering, H. J. A. 2000, *Monthly Notices of the Royal Astronomical Society*, 315, 381
- Kang, Y., Bianchi, L., & Rey, S.-C. 2009, *The Astrophysical Journal*, 703, 614



- Karouzos, M., Im, M., Trichas, M., et al. 2014, *The Astrophysical Journal*, 784, 137
- Kartaltepe, J. S., Sanders, D. B., Le Floch, E., et al. 2010, *The Astrophysical Journal*, 721, 98
- Kawinwanichakij, L., Papovich, C., Quadri, R. F., et al. 2014, *The Astrophysical Journal*, 792, 103
- Kellermann, K. I., Sramek, R., Schmidt, M., Shaffer, D. B., & Green, R. 1989, *The Astronomical Journal*, 98, 1195
- Kennicutt, R. C., & Evans, N. J. 2012, *Annual Review of Astronomy and Astrophysics*, 50, 531
- Kerr, R. P. 1963, *Physical Review Letters*, 11, 237
- Kim, M., Ho, L. C., & Im, M. 2006, *The Astrophysical Journal*, 642, 702
- King, A., & Pounds, K. 2015, *Annual Review of Astronomy and Astrophysics*, 53, 115
- King, A. R. 2010, *Monthly Notices of the Royal Astronomical Society*, 402, 1516
- Knapen, J. H., & James, P. A. 2009, *The Astrophysical Journal*, 698, 1437
- Koekemoer, A. M., Faber, S. M., Ferguson, H. C., et al. 2011, *The Astrophysical Journal Supplement*, 197, 36
- Koo, D. C., & Kron, R. G. 1988, *The Astrophysical Journal*, 325, 92
- Kormendy, J., & Ho, L. C. 2013, *Annual Review of Astronomy and Astrophysics*, 51, 511
- Kormendy, J., & Kennicutt, R. C. J. 2004, *Annual Review of Astronomy and Astrophysics*, 42, 603
- Kormendy, J., & Richstone, D. 1995, *Annual Review of Astronomy and Astrophysics*, 33, 581
- Kriek, M., Van Dokkum, P. G., Labbé, I., et al. 2009, *The Astrophysical Journal*, 700, 221
- Krumholz, M. R., & Thompson, T. A. 2013, *Monthly Notices of the Royal Astronomical Society*, 434, 2329
- Labbé, I., Bouwens, R., Illingworth, G. D., & Franx, M. 2006, *The Astrophysical Journal*, 649, L67
- Labbé, I., Huang, J., Franx, M., et al. 2005, *The Astrophysical Journal*, 624, L81
- Lacy, M., Croft, S., Fragile, C., Wood, S., & Nyland, K. 2017, *The Astrophysical Journal*, 838, 146
- Lacy, M., Laurent-Muehleisen, S. A., Ridgway, S. E., Becker, R. H., & White, R. L. 2001, *The Astrophysical Journal*, 551, L17
- Lacy, M., Petric, A. O., Sajina, A., et al. 2006, 133, 186

- Lanzuisi, G., Ranalli, P., Georgantopoulos, I., et al. 2015, *Astronomy & Astrophysics*, 573, A137
- Larson, R. B. 1974, *Monthly Notices of the Royal Astronomical Society*, 169, 229
- Lawrence, A., Warren, S. J., Almaini, O., et al. 2007, *Monthly Notices of the Royal Astronomical Society*, 379, 1599
- Lehmer, B. D., Basu-Zych, A. R., Mineo, S., et al. 2016, *The Astrophysical Journal Letters*, 825, 7
- Leja, J., van Dokkum, P., & Franx, M. 2013, *The Astrophysical Journal*, 766, 33
- Licquia, T. C., & Newman, J. A. 2015, *The Astrophysical Journal*, 806, 96
- Lira, P., Ward, M., Zezas, A., Alonso-Herrero, A., & Ueno, S. 2002, *Monthly Notices of the Royal Astronomical Society*, 330, 259
- Liu, S., & Melia, F. 2001, *The Astrophysical Journal*, 550, L151
- Luo, B., Brandt, W. N., Xue, Y. Q., et al. 2017, *The Astrophysical Journal Supplement*, 228, 2
- Lutz, D., Mainieri, V., Rafferty, D., et al. 2010, *The Astrophysical Journal*, 712, 1287
- MacDonald, C. J., & Bernstein, G. 2010, *Publications of the Astronomical Society of the Pacific*, 122, 485
- Madau, P., & Dickinson, M. 2014, *Annual Review of Astronomy and Astrophysics*, 52, 415
- Madau, P., Pozzetti, L., & Dickinson, M. 1998, *The Astrophysical Journal*, 498, 106
- Magorrian, J., Tremaine, S., Richstone, D., et al. 1998, 115, 2285
- Maraston, C. 2005, *Monthly Notices of the Royal Astronomical Society*, 362, 799
- Marconi, A., & Hunt, L. K. 2003, *The Astrophysical Journal Letters*, 589, L21
- Marconi, A., Risaliti, G., Gilli, R., et al. 2004, *Monthly Notices of the Royal Astronomical Society*, 351, 169
- Martig, M., & Bournaud, F. 2010, *The Astrophysical Journal*, 714, L275
- Martig, M., Bournaud, F., Teyssier, R., & Dekel, A. 2009, *The Astrophysical Journal*, 707, 250
- Martini, P. 2004, *QSO Lifetimes*
- Matthews, T. A., Morgan, W. W., & Schmidt, M. 1964, *The Astrophysical Journal*, 140, 35
- McConnell, N. J., & Ma, C.-P. 2013, *The Astrophysical Journal*, 764, 184
- McMillan, P. J. 2011, *Monthly Notices of the Royal Astronomical Society*, 414, 2446

- Menci, N., Fiore, F., Puccetti, S., & Cavaliere, A. 2008, *The Astrophysical Journal*, 686, 219
- Merloni, A., & Heinz, S. 2008, *Monthly Notices of the Royal Astronomical Society*, 388, 1011
- Merloni, A., Rudnick, G., & Di Matteo, T. 2004, *Monthly Notices of the Royal Astronomical Society*, 354, L37
- Messias, H., Afonso, J., Salvato, M., Mobasher, B., & Hopkins, A. M. 2012, *The Astrophysical Journal*, 754, 120
- Miller, N. A., Bonzini, M., Fomalont, E. B., et al. 2013, *The Astrophysical Journal Supplement*, 205, 13
- Montesinos Armijo, M. A., & de Freitas Pacheco, J. A. 2011, *Astronomy & Astrophysics*, 526, A146
- Moran, E. C., Lehnert, M. D., & Helfand, D. J. 1999, *The Astrophysical Journal*, 526, 649
- Morić, I., Smolčić, V., Kimball, A., et al. 2010, *The Astrophysical Journal*, 724, 779
- Moster, B. P., Naab, T., & White, S. D. M. 2013, *Monthly Notices of the Royal Astronomical Society*, 428, 3121
- Mullaney, J. R., Pannella, M., Daddi, E., et al. 2012a, *Monthly Notices of the Royal Astronomical Society*, 419, 95
- Mullaney, J. R., Daddi, E., Béthermin, M., et al. 2012b, *The Astrophysical Journal Letters*, 753, L30
- Mullaney, J. R., Alexander, D. M., Aird, J., et al. 2015, *Monthly Notices of the Royal Astronomical Society: Letters*, 453, L83
- Murphy, E. J., Chary, R. R., Alexander, D. M., et al. 2008, *The Astrophysical Journal*, 1380
- Murray, N., Ménard, B., & Thompson, T. A. 2011, *The Astrophysical Journal*, 735, 66
- Murray, N., Quataert, E., & Thompson, T. A. 2005, *The Astrophysical Journal*, 618, 569
- Mutch, S. J., Croton, D. J., & Poole, G. B. 2011, *The Astrophysical Journal*, 736, 84
- Nanayakkara, T., Glazebrook, K., Kacprzak, G. G., et al. 2016, *The Astrophysical Journal*, 828, 21
- Narayan, R., & Yi, I. 1995, *The Astrophysical Journal*, 452, 710
- Negroponte, J., & White, S. D. M. 1983, *Monthly Notices of the Royal Astronomical Society*, 205, 1009
- Nenkova, M., Ivezić, Ž., & Elitzur, M. 2002, *The Astrophysical Journal*, 570, L9
- Nesvadba, N. P. H., Lehnert, M. D., Eisenhauer, F., et al. 2006, *The Astrophysical Journal*, 650, 693

- Netzer, H. 2009, *Monthly Notices of the Royal Astronomical Society*, 399, 1907
- . 2015, *Annual Review of Astronomy and Astrophysics*, 53, 365
- Netzer, H., Lutz, D., Schweitzer, M., et al. 2007, *The Astrophysical Journal*, 666, 806
- Neugebauer, G., Oke, J. B., Becklin, E. E., & Matthews, K. 1979, *The Astrophysical Journal*, 230, 79
- Noeske, K. G., Faber, S. M., Weiner, B. J., et al. 2007, *The Astrophysical Journal*, 660, L47
- Noll, S., Burgarella, D., Giovannoli, E., et al. 2009, *Astronomy & Astrophysics*, 507, 1793
- Norris, R. P., Afonso, J., Appleton, P. N., et al. 2006, 132, 2409
- Osmer, P. S., & Hewett, P. C. 1991, *The Astrophysical Journal Supplement*, 75, 273
- Padovani, P., Alexander, D. M., Assef, R. J., et al. 2017, *Astronomy and Astrophysics Review*, 25, 30
- Page, M. J., Symeonidis, M., Vieira, J. D., et al. 2012, *Nature*, 485, 213
- Papovich, C., Labbé, I., Quadri, R., et al. 2015, *The Astrophysical Journal*, 803, 26
- Persson, S. E., Murphy, D. C., Smee, S., et al. 2013, *Publications of the Astronomical Society of the Pacific*, 125, 654
- Pilbratt, G. L., Riedinger, J. R., Passvogel, T., et al. 2010, *Astronomy & Astrophysics*, 518, L1
- Poglitsch, A., Waelkens, C., Geis, N., et al. 2010, *Astronomy & Astrophysics*, 518, L2
- Polletta, M., Weedman, D., Hönig, S., et al. 2008, *The Astrophysical Journal*, 675, 960
- Polletta, M., Tajer, M., Maraschi, L., et al. 2007, *The Astrophysical Journal*, 663, 81
- Pope, A., Wagg, J., Frayer, D., et al. 2013, *The Astrophysical Journal*, 772, 92
- Pozzi, F., Vignali, C., Gruppioni, C., et al. 2012, *Monthly Notices of the Royal Astronomical Society*, 423, 1909
- Ptak, A. 2002, in *X-RAY ASTRONOMY: Stellar Endpoints, AGN, and the Diffuse X-ray Background (AIP)*, 326–335
- Querejeta, M., Meidt, S. E., Schinnerer, E., et al. 2016, *Astronomy & Astrophysics*, 588, A33
- Rafferty, D. A., Brandt, W. N., Alexander, D. M., et al. 2011, *The Astrophysical Journal*, 742, 3
- Rees, G. A., Spitler, L. R., Norris, R. P., et al. 2016, *Monthly Notices of the Royal Astronomical Society*, 455, 2731

- Rejkuba, M., Minniti, D., Courbin, F., & Silva, D. R. 2002, *The Astrophysical Journal*, 564, 688
- Richards, G. T., Fan, X., Schneider, D. P., et al. 2001, *The Astronomical Journal*, 121, 2308
- Richardson, M. L. A., Scannapieco, E., Devriendt, J., et al. 2016, *The Astrophysical Journal Letters*, 825, 83
- Rieke, G. H., Young, E. T., Engelbracht, C. W., et al. 2004, *The Astrophysical Journal Supplement*, 154, 25
- Robitaille, T. P., & Whitney, B. A. 2010, *The Astrophysical Journal Letters*, 710, L11
- Roos, O., Juneau, S., Bournaud, F., & Gabor, J. M. 2015, *The Astrophysical Journal*, 800, 19
- Rosario, D. J., Santini, P., Lutz, D., et al. 2012, *Astronomy & Astrophysics*, 545, A45
- . 2013, *The Astrophysical Journal*, 771, 63
- Rosario, D. J., McIntosh, D. H., van der Wel, A., et al. 2014, *Astronomy & Astrophysics*, 573, A85
- Rovilos, E., Comastri, A., Gilli, R., et al. 2012, *Astronomy & Astrophysics*, 546, A58
- Rovilos, E., Georgantopoulos, I., Akylas, A., et al. 2014, *Monthly Notices of the Royal Astronomical Society*, 438, 494
- Rowan-Robinson, M. 1977, *The Astrophysical Journal*, 213, 635
- Sales, L. V., Navarro, J. F., Theuns, T., et al. 2012, *Monthly Notices of the Royal Astronomical Society*, 423, 1544
- Salim, S., Rich, R. M., Charlot, S., et al. 2007, *The Astrophysical Journal Supplement*, 173, 267
- Sanders, D. B., Phinney, E. S., Neugebauer, G., Soifer, B. T., & Matthews, K. 1989, *The Astrophysical Journal*, 347, 29
- Sanders, D. B., Soifer, B. T., Elias, J. H., et al. 1988, *The Astrophysical Journal*, 325, 74
- Sani, E., Marconi, A., Hunt, L. K., & Risaliti, G. 2011, *Monthly Notices of the Royal Astronomical Society*, 413, 1479
- Santini, P., Rosario, D. J., Shao, L., et al. 2012, *Astronomy & Astrophysics*, 540, A109
- Satyapal, S., Ellison, S. L., McAlpine, W., et al. 2014, *Monthly Notices of the Royal Astronomical Society*, 441, 1297
- Schawinski, K., Urry, C. M., Virani, S., et al. 2010, *The Astrophysical Journal*, 711, 284
- Schinnerer, E., Sargent, M. T., Bondi, M., et al. 2010, *The Astrophysical Journal Supplement*, 188, 384
- Schmidt, M. 1963, *Nature*, 197, 1040

- Schmidt, M., & Matthews, T. A. 1964, *The Astrophysical Journal*, 139, 781
- Scoville, N., Aussel, H., Brusa, M., et al. 2007, *The Astrophysical Journal Supplement*, 172, 1
- Shabala, S. S., Sen Ting, Y., Kaviraj, S., et al. 2012, *Monthly Notices of the Royal Astronomical Society*, 423, 59
- Shakura, N. I., & Sunyaev, R. A. 1973, *Astronomy & Astrophysics*, 24, 337
- Shankar, F., Cavaliere, A., Cirasuolo, M., & Maraschi, L. 2008, *The Astrophysical Journal*, 676, 131
- Shao, L., Lutz, D., Nordon, R., et al. 2010, *Astronomy & Astrophysics*, 518, L26
- Siebenmorgen, R., Heymann, F., & Efstathiou, A. 2015, *Astronomy & Astrophysics*, 583, A120
- Silk, J. 2005, *Monthly Notices of the Royal Astronomical Society*, 364, 1337
- . 2013, *The Astrophysical Journal*, 772, 112
- Silk, J., & Norman, C. 2009, *The Astrophysical Journal*, 700, 262
- Silk, J., & Rees, M. J. 1998, *Astronomy & Astrophysics*, 331, L1
- Silverman, J. D., Green, P. J., Barkhouse, W. A., et al. 2008, *The Astrophysical Journal*, 679, 118
- Silverman, J. D., Lamareille, F., Maier, C., et al. 2009, *The Astrophysical Journal*, 696, 396
- Silverman, J. D., Kampczyk, P., Jahnke, K., et al. 2011, *The Astrophysical Journal*, 743, 2
- Simoes Lopes, R. D., Storch Bergmann, T., de Fatima Saraiva, M., & Martini, P. 2007, *The Astrophysical Journal*, 655, 718
- Simpson, C., Martínez-Sansigre, A., Rawlings, S., et al. 2006, *Monthly Notices of the Royal Astronomical Society*, 372, 741
- Skelton, R. E., Whitaker, K. E., Momcheva, I. G., et al. 2014, *The Astrophysical Journal Supplement*, 214, 24
- Spitler, L. R., Labbé, I., Glazebrook, K., et al. 2012, *The Astrophysical Journal Letters*, 748, L21
- Spitler, L. R., Straatman, C. M. S., Labbé, I., et al. 2014, *The Astrophysical Journal Letters*, 787, L36
- Springel, V. 2000, *Monthly Notices of the Royal Astronomical Society*, 312, 859
- Stanley, F., Harrison, C. M., Alexander, D. M., et al. 2015, *Monthly Notices of the Royal Astronomical Society*, 453, 591
- Stern, D., Eisenhardt, P., Gorjian, V., et al. 2005, *The Astrophysical Journal*, 631, 163

- Straatman, C. M. S., Spitler, L. R., Quadri, R. F., et al. 2016, *The Astrophysical Journal*, 830, 51
- Szokoly, G. P., Bergeron, J., Hasinger, G., et al. 2004, *The Astrophysical Journal Supplement*, 155, 271
- Tomczak, A. R., Quadri, R. F., Tran, K.-V. H., et al. 2014, *The Astrophysical Journal*, 783, 85
- Treister, E., Krolik, J. H., & Dullemond, C. 2008, *The Astrophysical Journal*, 679, 140
- Treister, E., Schawinski, K., Urry, C. M., & Simmons, B. D. 2012, *The Astrophysical Journal Letters*, 758, L39
- Tremaine, S., Gebhardt, K., Bender, R., et al. 2002, *The Astrophysical Journal*, 574, 740
- Tremonti, C. A., Heckman, T. M., Kauffmann, G., et al. 2004, *The Astrophysical Journal*, 613, 898
- Turner, M. J. L., Abbey, A., Arnaud, M., et al. 2001, *Astronomy & Astrophysics*, 365, L27
- Ueda, Y., Watson, M. G., Stewart, I. M., et al. 2008, *The Astrophysical Journal Supplement*, 179, 124
- Ulvestad, J. S., & Wilson, A. S. 1984, *The Astrophysical Journal*, 285, 439
- Urry, C. M., & Padovani, P. 1995, *Publications of the Astronomical Society of the Pacific*, 107, 803
- Van Dokkum, P. G., & Franx, M. 2001, *The Astrophysical Journal*, 553, 90
- Van Dokkum, P. G., Leja, J., Nelson, E. J., et al. 2013, *The Astrophysical Journal*, 771, L35
- Vasudevan, R. V., & Fabian, A. C. 2007, *Monthly Notices of the Royal Astronomical Society*, 381, 1235
- Watson, M. G., Augeres, J. L., Ballet, J., et al. 2001, *Astronomy & Astrophysics*, 365, L51
- Weisskopf, M. C., Tananbaum, H. D., Van Speybroeck, L. P., & O'Dell, S. L. 2000, in *Astronomical Telescopes and Instrumentation*, ed. J. E. Truemper & B. Aschenbach (SPIE), 2–16
- Werner, M. W., Roellig, T. L., Low, F. J., et al. 2004, *The Astrophysical Journal Supplement*, 154, 1
- Whitaker, K. E., Labbé, I., Van Dokkum, P. G., et al. 2011, *The Astrophysical Journal*, 735, 86
- Whitaker, K. E., Franx, M., Leja, J., et al. 2014, *The Astrophysical Journal*, 795, 104
- Williams, R. J., Quadri, R. F., Franx, M., van Dokkum, P., & Labbé, I. 2009, *The Astrophysical Journal*, 691, 1879
- Wuyts, S., Labbé, I., Schreiber, N. M. F., et al. 2008, *The Astrophysical Journal*, 682, 985

- Wuyts, S., Labbé, I., Franx, M., et al. 2007, *The Astrophysical Journal*, 655, 51
- Wuyts, S., Forster Schreiber, N. M., Lutz, D., et al. 2011, *The Astrophysical Journal*, 738, 106
- Wylezalek, D., Zakamska, N. L., Liu, G., & Obied, G. 2016, *Monthly Notices of the Royal Astronomical Society*, 457, 745
- Xue, Y. Q., Brandt, W. N., Luo, B., et al. 2010, *The Astrophysical Journal*, 720, 368
- Xue, Y. Q., Luo, B., Brandt, W. N., et al. 2011, *The Astrophysical Journal Supplement*, 195, 10
- Yan, R., Ho, L. C., Newman, J. A., et al. 2011, *The Astrophysical Journal*, 728, 38
- Yusef-Zadeh, F., Bushouse, H., Schödel, R., et al. 2015, *The Astrophysical Journal Letters*, 809, 10
- Zinn, P. C., Middelberg, E., Norris, R. P., & Dettmar, R. J. 2013, *The Astrophysical Journal Supplement*, 774, 66
- Zubovas, K., & King, A. 2012, *The Astrophysical Journal*, 745, L34



# Appendix A

## Catalogue of AGN Candidates

In the table below, we summarise the columns of our AGN dataset, which provides all host galaxy parameters used to select AGN in Chapter 2. This dataset acts as a complementary catalogue to the primary ZFOURGE catalogues and is used throughout the body of this work.

1. Source ID number
2. J2000 RA of the *Ks*-band selected hosts
3. J2000 declination of the *Ks*-band selected hosts
4. Photometric redshift
5. *Ks*-band magnitude (AB)
6. *UVJ* criteria, where quiescent = 1, star-forming = 2 and dusty star-forming = 3
7. Host stellar mass ( $M_{\odot}$ )
8. Integrated 1216-3000Å rest-frame UV luminosity ( $L_{\odot}$ )
9. Integrated 8 – 1000 $\mu$ m rest-frame IR luminosity ( $L_{\odot}$ )
10. 0.5-8 keV rest-frame luminosity ( $\text{erg s}^{-1}$ )
11. 1.4GHz rest-frame luminosity ( $\text{W Hz}^{-1}$ )
12. IR AGN flag, where AGN = 1, else = 0
13. X-Ray AGN flag, where AGN = 1, else = 0
14. Radio AGN flag, where AGN = 1, else = 0

**Table A.1** AGN in ZFOURGE

ID <sup>1</sup>	RA-J2000 <sup>2</sup>	Dec-J2000 <sup>3</sup>	$z_{\text{phot}}$ <sup>4</sup>	$K_{\text{S, mag}}$ <sup>5</sup>	UVJ <sup>6</sup>	$\log(M_{\text{A}})$ <sup>7</sup>	$\log(L_{\text{UV}})$ <sup>8</sup>	$\log(L_{\text{IR}})$ <sup>9</sup>	$\log(L_{\text{X}})$ <sup>10</sup>	$\log(L_{1.4\text{GHz}})$ <sup>11</sup>	IR-AGN <sup>12</sup>	X-AGN <sup>13</sup>	Rad-AGN <sup>14</sup>
COSMOS_1132	150.0646515	2.1909399	6.59	22.24	3	12.32	1.11E+11	-99	1.68E+45	1.39E+25	0	1	0
COSMOS_1219	150.1508636	2.1913352	1.24	21.54	3	10.15	9.93E+08	3.10E+10	8.27E+42	-99	0	1	-1
COSMOS_1265	150.1997681	2.1908534	2.94	20.01	2	11.15	2.32E+11	3.73E+12	4.61E+44	-99	0	1	-1
COSMOS_1285	150.1594849	2.1914873	1.00	20.30	3	10.35	1.75E+09	1.16E+12	-99	6.21E+23	1	-1	0
COSMOS_1578	150.1047668	2.1957085	1.20	22.09	3	10.31	3.83E+08	3.28E+10	-99	-99	1	-1	-1
COSMOS_1813	150.0365448	2.1983893	2.65	22.90	3	11.05	2.51E+09	2.59E+11	-99	-99	1	-1	-1
COSMOS_1946	150.1934662	2.1993923	2.50	22.53	2	10.85	4.42E+09	-2.68E+11	5.37E+43	-99	0	1	-1
COSMOS_1958	150.1598816	2.198812	1.13	20.57	3	10.58	5.58E+09	1.66E+11	-99	-99	1	-1	-1
COSMOS_1964	150.100235	2.1998861	1.29	21.97	2	10.19	1.52E+09	-8.45E+09	2.99E+43	-99	0	1	-1
COSMOS_2220	150.1550598	2.2021444	0.87	21.17	3	9.73	1.70E+09	6.58E+10	-99	-99	1	-1	-1
COSMOS_2338	150.0640411	2.2032876	1.60	21.92	3	10.34	3.26E+09	2.80E+11	-99	-99	1	-1	-1
COSMOS_2384	150.1799011	2.2036521	1.15	21.61	3	10.24	1.72E+09	1.13E+11	-99	-99	1	-1	-1
COSMOS_2477	150.2146759	2.2042632	0.73	20.82	2	9.51	2.65E+10	-1.54E+10	4.11E+43	-99	1	1	-1
COSMOS_2531	150.0396423	2.2057285	1.22	23.13	2	9.38	1.13E+09	2.01E+11	-99	-99	1	-1	-1
COSMOS_2717	150.181366	2.2065947	1.15	21.07	3	10.61	5.56E+08	2.81E+11	-99	-99	1	-1	-1
COSMOS_2859	150.0907135	2.2056594	0.41	17.86	1	10.94	1.14E+09	4.31E+10	-99	1.99E+23	0	-1	1
COSMOS_2869	150.0572052	2.2058876	0.18	17.52	2	9.99	1.83E+09	7.49E+09	3.14E+41	3.54E+22	0	1	1
COSMOS_3166	150.0740204	2.2113466	0.90	23.09	3	8.74	7.63E+08	6.24E+10	-99	-99	1	-1	-1
COSMOS_3324	150.1273651	2.2116182	0.95	21.01	2	9.95	4.09E+09	1.24E+11	-99	-99	1	-1	-1
COSMOS_3384	150.1326447	2.2119355	2.18	21.26	3	11.47	5.54E+09	7.12E+12	-99	4.05E+24	1	-1	0
COSMOS_3509	150.1059875	2.2131407	0.95	20.26	3	10.37	4.59E+09	2.30E+11	5.52E+42	-99	0	1	-1
COSMOS_3846	150.1760254	2.2155676	0.67	20.20	2	10.24	2.65E+09	-1.60E+09	2.95E+42	-99	0	1	-1
COSMOS_3847	150.1614227	2.2170615	1.95	22.11	2	10.32	9.18E+09	1.66E+11	-99	-99	1	-1	-1
COSMOS_3855	150.0963135	2.2171569	1.14	21.24	2	10.13	5.63E+09	2.98E+10	-99	-99	1	-1	-1
COSMOS_3910	150.1704865	2.2188063	1.21	21.54	3	10.12	2.80E+09	3.77E+11	3.28E+43	1.02E+24	1	1	1
COSMOS_3954	150.045105	2.2178605	2.23	20.98	2	10.6	4.16E+10	7.03E+11	2.49E+43	-99	0	1	-1
COSMOS_3993	150.0592346	2.2198634	1.16	20.42	3	10.75	6.08E+09	-7.02E+12	3.45E+43	-99	0	1	-1
COSMOS_4131	150.1926422	2.2198358	3.07	21.96	3	10.94	3.52E+10	2.27E+12	9.35E+43	-99	0	1	-1
COSMOS_4174	150.0957336	2.2212021	0.17	23.45	2	7.24	3.86E+07	-7.83E+08	-99	-99	1	-1	-1
COSMOS_4229	150.1203766	2.2212648	2.15	22.61	1	10.49	1.70E+09	-2.77E+11	1.82E+43	-99	0	1	-1
COSMOS_4291	150.0590668	2.2200422	1.15	19.80	3	10.98	8.74E+09	8.31E+11	-99	-99	1	-1	-1
COSMOS_4356	150.1143646	2.2219763	1.24	21.18	3	10.03	2.85E+09	1.63E+11	-99	-99	1	-1	-1
COSMOS_4618	150.118576	2.223103	0.84	19.73	3	10.79	1.52E+09	1.24E+11	-99	3.74E+23	1	-1	1

continued ...

ID <sup>1</sup>	RA-J2000 <sup>2</sup>	Dec-J2000 <sup>3</sup>	$z_{\text{phot}}$ <sup>4</sup>	$K_{\text{Smag}}$ <sup>5</sup>	UVJ <sup>6</sup>	$\log(M_{\star})$ <sup>7</sup>	$\log(L_{\text{UV}})$ <sup>8</sup>	$\log(L_{\text{IR}})$ <sup>9</sup>	$\log(L_{\star})$ <sup>10</sup>	$\log(L_{1.4\text{GHz}})$ <sup>11</sup>	IR-AGN <sup>12</sup>	X-AGN <sup>13</sup>	Rad-AGN <sup>14</sup>
COSMOS_4695	150.1363983	2.2252984	1.85	21.63	3	10.45	5.73E+09	2.56E+12	1.93E+43	1.00E+24	0	1	0
COSMOS_4706	150.1382751	2.2250166	1.64	21.14	3	11.18	1.52E+09	3.26E+11	1.89E+43	-99	0	1	-1
COSMOS_4844	150.0908508	2.226373	1.16	21.61	2	10	2.50E+09	5.75E+10	-99	-99	1	-1	-1
COSMOS_5101	150.1209412	2.2271283	0.72	18.57	1	11.06	3.61E+09	2.47E+09	-99	3.17E+23	0	-1	1
COSMOS_5131	150.0959167	2.2309027	1.48	21.90	2	10.35	8.71E+09	1.36E+10	1.29E+43	-99	1	1	-1
COSMOS_5146	150.0692444	2.2313242	1.83	22.41	2	9.64	9.12E+09	-4.91E+10	7.94E+43	-99	0	1	-1
COSMOS_5200	150.1800232	2.2312827	1.25	21.80	2	10.1	5.74E+09	2.95E+11	4.09E+43	-99	1	1	-1
COSMOS_5365	150.1792297	2.2336783	2.22	22.51	1	10.88	8.90E+08	1.02E+12	-99	-99	1	-1	-1
COSMOS_5434	150.1691589	2.2339015	1.25	21.48	2	10.06	7.58E+09	2.94E+11	-99	-99	1	-1	-1
COSMOS_5636	150.0559235	2.2334719	1.00	18.67	3	11.3	1.88E+10	8.24E+11	3.64E+43	-99	1	1	-1
COSMOS_5751	150.0936279	2.237221	1.42	20.86	2	10.46	1.75E+10	6.59E+10	-99	-99	1	-1	-1
COSMOS_6336	150.0495911	2.2402644	0.57	19.94	3	10.34	1.30E+09	3.69E+10	1.59E+42	-99	0	1	-1
COSMOS_6344	150.1046753	2.2436953	1.80	22.12	3	10.74	9.43E+08	1.68E+11	5.03E+43	-99	0	1	-1
COSMOS_6532	150.2034454	2.2467072	2.97	22.85	2	10.64	4.74E+09	-8.46E+10	3.77E+43	-99	0	1	-1
COSMOS_6550	150.0940552	2.245899	1.77	22.05	3	10.41	9.08E+09	1.30E+12	-99	-99	1	-1	-1
COSMOS_6789	150.1829834	2.2479241	1.51	19.91	2	11.31	9.04E+09	5.55E+11	1.58E+43	-99	1	1	-1
COSMOS_6797	150.0648956	2.2486718	2.56	22.61	2	10.44	6.80E+09	7.83E+11	-99	-99	1	-1	-1
COSMOS_7496	150.2307281	2.2554808	2.37	21.22	3	11.3	5.86E+09	6.44E+11	5.40E+43	-99	0	1	-1
COSMOS_7647	150.036911	2.2578084	2.70	22.48	3	11.02	2.72E+09	7.03E+10	9.08E+43	-99	1	1	-1
COSMOS_7689	150.1374512	2.2584884	0.93	21.28	2	9.73	4.13E+09	1.61E+10	-99	-99	1	-1	-1
COSMOS_7841	150.2176971	2.2610216	2.95	23.05	3	10.8	3.40E+09	5.28E+12	-99	-99	1	-1	-1
COSMOS_7967	150.151062	2.2623641	2.86	23.58	3	10.45	1.35E+09	7.74E+10	-99	-99	1	-1	-1
COSMOS_8045	150.2157898	2.2626021	1.18	21.71	3	10.03	1.62E+09	1.75E+09	-99	-99	1	-1	-1
COSMOS_8174	150.0760193	2.2642891	2.93	22.32	2	10.55	2.45E+10	-8.72E+11	7.93E+43	-99	0	1	-1
COSMOS_8287	150.1419983	2.2651024	2.18	22.03	3	11.03	3.56E+09	1.80E+11	3.55E+43	-99	0	1	-1
COSMOS_8449	150.2028961	2.2667546	1.95	21.82	2	10.71	4.01E+09	1.61E+12	-99	-99	1	-1	-1
COSMOS_8509	150.0790558	2.2665696	1.84	20.75	2	10.96	3.03E+10	7.40E+10	2.74E+43	-99	0	1	-1
COSMOS_8549	150.080368	2.2659395	1.43	20.76	2	10.84	5.48E+09	2.42E+11	2.19E+43	-99	0	1	-1
COSMOS_8793	150.2221985	2.2702763	2.95	23.12	3	10.74	5.65E+09	5.06E+11	3.72E+43	-99	0	1	-1
COSMOS_8924	150.0366364	2.2709649	1.87	22.39	3	10.53	5.17E+09	1.56E+12	-99	-99	1	-1	-1
COSMOS_8926	150.2240448	2.2707946	1.70	20.55	2	11.07	9.41E+09	2.48E+12	5.30E+43	2.49E+24	1	1	0
COSMOS_9088	150.1412354	2.2729745	0.92	21.21	2	9.81	3.54E+09	3.00E+09	-99	-99	1	-1	-1
COSMOS_9206	150.2175446	2.2731247	1.27	21.18	2	10.21	1.17E+10	2.48E+11	-99	-99	1	-1	-1
COSMOS_9284	150.0545502	2.275347	1.45	21.10	3	11.04	1.65E+09	2.87E+11	-99	-99	1	-1	-1
COSMOS_9408	150.1365356	2.274405	1.21	19.22	1	11.33	7.45E+09	1.82E+11	5.42E+42	-99	0	1	-1
COSMOS_9514	150.2189789	2.2787063	4.43	23.56	3	11.13	8.80E+09	2.54E+13	4.78E+44	-99	1	1	-1

continued ...

ID <sup>1</sup>	RA-J2000 <sup>2</sup>	Dec-J2000 <sup>3</sup>	$z_{\text{phot}}$ <sup>4</sup>	$K_{\text{Smag}}$ <sup>5</sup>	UVJ <sup>6</sup>	$\log(M_*)$ <sup>7</sup>	$\log(L_{\text{UV}})$ <sup>8</sup>	$\log(L_{\text{IR}})$ <sup>9</sup>	$\log(L_\lambda)$ <sup>10</sup>	$\log(L_{1.4\text{GHz}})$ <sup>11</sup>	IR-AGN <sup>12</sup>	X-AGN <sup>13</sup>	Rad-AGN <sup>14</sup>
COSMOS_9523	150.1413116	2.2781932	2.18	22.60	3	10.85	1.53E+09	6.52E+10	3.73E+43	-99	0	1	-1
COSMOS_9653	150.0410461	2.2804437	3.64	24.40	3	11.24	5.38E+08	1.09E+11	-99	-99	1	-1	-1
COSMOS_9791	150.0867615	2.2814937	2.62	22.88	1	10.6	1.90E+09	-1.52E+11	3.68E+43	-99	0	1	-1
COSMOS_9965	150.2074585	2.2818861	0.93	19.59	1	11.06	1.17E+09	4.55E+10	-99	3.01E+24	0	-1	1
COSMOS_10008	150.0878143	2.2832317	1.19	21.50	2	10.12	5.47E+09	3.85E+10	-99	-99	1	-1	-1
COSMOS_10039	150.2249756	2.2841661	0.11	21.86	3	7.1	1.78E+07	3.25E+08	6.56E+40	-99	1	0	-1
COSMOS_10197	150.227066	2.2856464	1.12	21.58	2	9.91	2.70E+09	-1.89E+10	-99	-99	1	-1	-1
COSMOS_10283	150.0704956	2.2862778	0.92	20.74	1	10.53	9.25E+08	1.73E+09	1.23E+43	-99	0	1	-1
COSMOS_10324	150.0782318	2.2873745	0.92	21.98	2	9.81	6.86E+08	-5.77E+09	-99	-99	1	-1	-1
COSMOS_10553	150.1653748	2.2894073	0.75	20.09	3	10.08	1.53E+09	3.64E+11	-99	-99	1	-1	-1
COSMOS_10649	150.1380157	2.2916684	0.17	16.75	3	10.56	1.14E+09	2.82E+10	4.12E+42	-99	0	1	-1
COSMOS_10657	150.1471558	2.291575	1.80	22.25	3	10.64	1.62E+09	-3.94E+10	-99	-99	1	-1	-1
COSMOS_10672	150.0843811	2.2905147	1.29	20.52	2	10.8	1.23E+10	4.41E+11	3.93E+43	-99	1	1	-1
COSMOS_10787	150.0965118	2.2930152	1.74	21.56	1	10.83	2.50E+09	8.35E+10	7.28E+43	-99	0	1	-1
COSMOS_10822	150.0366211	2.2942481	1.59	22.87	3	10.28	1.58E+09	-2.33E+09	-99	-99	1	-1	-1
COSMOS_11077	150.1193085	2.2968464	2.04	23.45	2	9.56	8.08E+09	3.90E+11	-99	-99	1	-1	-1
COSMOS_11132	150.0660248	2.2955425	1.22	20.10	1	10.95	4.59E+09	4.92E+10	1.80E+43	-99	0	1	-1
COSMOS_11161	150.1196136	2.2958577	2.17	20.36	2	11.43	2.38E+10	8.22E+11	3.20E+44	-99	0	1	-1
COSMOS_11296	150.0857849	2.2976573	1.28	19.92	3	10.62	1.88E+10	1.69E+12	-99	6.75E+23	1	-1	0
COSMOS_11322	150.0473938	2.299125	1.46	22.15	3	10.31	1.26E+09	3.74E+12	-99	-99	1	-1	-1
COSMOS_11385	150.0961456	2.2985673	0.35	17.94	1	10.75	7.45E+08	2.88E+09	-99	2.54E+22	0	-1	1
COSMOS_11571	150.0940704	2.2991059	0.69	19.69	2	9.99	1.06E+10	4.53E+11	-99	-99	1	-1	-1
COSMOS_11598	150.089325	2.2995667	0.55	19.82	3	10.27	1.52E+09	1.53E+10	-99	6.63E+22	0	-1	1
COSMOS_11650	150.0746002	2.3020091	2.16	21.24	3	11.24	4.00E+09	6.67E+10	9.79E+43	-99	0	1	-1
COSMOS_11661	150.0790405	2.3017457	1.43	21.70	2	10.32	6.97E+09	3.68E+11	-99	-99	1	-1	-1
COSMOS_11764	150.0566864	2.3013859	0.73	18.63	1	11.02	1.85E+09	5.40E+09	-99	2.43E+23	0	-1	1
COSMOS_11808	150.0566864	2.3024392	1.69	21.61	3	10.81	5.97E+09	3.96E+11	-99	-99	1	-1	-1
COSMOS_12003	150.1330719	2.3032517	1.59	20.05	3	11.46	1.10E+10	4.25E+09	7.53E+44	-99	1	1	-1
COSMOS_12112	150.0830078	2.3048217	0.34	19.26	3	10.18	2.96E+08	-2.20E+09	1.12E+42	-99	0	1	-1
COSMOS_12129	150.051651	2.3058436	1.48	20.49	3	11.06	6.29E+09	6.01E+11	3.34E+43	-99	1	1	-1
COSMOS_12173	150.1521912	2.3078091	3.27	21.89	2	11.05	1.62E+10	1.89E+12	1.02E+44	-99	1	1	-1
COSMOS_12348	150.1699219	2.3089187	0.26	22.42	2	8.04	9.04E+08	-2.10E+09	-99	-99	1	-1	-1
COSMOS_12853	150.216568	2.3150182	1.78	22.42	2	9.82	6.84E+09	1.44E+12	-99	-99	1	-1	-1
COSMOS_13407	150.0986633	2.3208246	2.87	23.50	3	9.92	5.46E+09	6.99E+12	-99	-99	1	-1	-1
COSMOS_13425	150.0365143	2.3212206	5.06	23.40	3	11.23	1.10E+10	-99	3.02E+44	-99	1	1	-1
COSMOS_13550	150.0917969	2.3219059	1.56	22.08	1	10.33	1.77E+09	1.84E+10	1.61E+43	-99	0	1	-1

continued ...

ID <sup>1</sup>	RA-J2000 <sup>2</sup>	Dec-J2000 <sup>3</sup>	$z_{\text{phot}}$ <sup>4</sup>	$K_{\text{S, mag}}$ <sup>5</sup>	UVJ <sup>6</sup>	$\log(M_{\star})$ <sup>7</sup>	$\log(L_{\text{UV}})$ <sup>8</sup>	$\log(L_{\text{IR}})$ <sup>9</sup>	$\log(L_{\star})$ <sup>10</sup>	$\log(L_{1.4\text{GHz}})$ <sup>11</sup>	IR-AGN <sup>12</sup>	X-AGN <sup>13</sup>	Rad-AGN <sup>14</sup>
COSMOS_13652	150.2151489	2.3227775	1.52	21.10	3	10.59	6.21E+09	4.95E+11	2.97E+43	-99	1	1	-1
COSMOS_13712	150.0487213	2.3221078	0.61	19.85	1	10.47	1.34E+09	2.34E+09	8.82E+42	-99	0	1	-1
COSMOS_13746	150.1101227	2.3245585	1.32	22.12	3	9.89	2.17E+09	7.11E+10	-99	-99	1	-1	-1
COSMOS_13753	150.1412354	2.3230076	0.92	20.35	3	10.68	9.44E+08	5.71E+10	-99	1.46E+23	0	-1	1
COSMOS_14228	150.0496521	2.3283734	0.95	19.93	2	10.62	4.17E+09	3.50E+10	4.35E+42	-99	0	1	-1
COSMOS_14230	150.0645447	2.3290317	3.35	20.62	2	10.67	1.40E+11	5.27E+12	2.22E+44	-99	0	1	-1
COSMOS_14262	150.1112976	2.3296711	1.22	21.27	1	10.51	1.34E+09	-1.89E+10	5.53E+42	-99	0	1	-1
COSMOS_14521	150.1617889	2.3323591	0.66	20.74	3	9.55	5.65E+08	1.58E+10	1.26E+43	1.24E+23	1	1	1
COSMOS_14931	150.1711426	2.3370435	1.28	21.19	3	10.57	2.58E+09	-4.65E+10	1.74E+43	-99	0	1	-1
COSMOS_15317	150.1218262	2.3413129	2.30	22.63	2	10.6	3.58E+09	2.94E+12	-99	-99	1	-1	-1
COSMOS_15674	150.2345123	2.3453355	1.76	21.74	3	10.65	3.62E+09	-1.44E+11	2.19E+43	-99	1	1	-1
COSMOS_16016	150.200882	2.348335	1.32	22.25	1	10.2	8.74E+08	2.54E+10	3.60E+43	-99	0	1	-1
COSMOS_16032	150.0736389	2.3468611	1.37	20.34	3	9.8	2.23E+10	7.04E+11	1.15E+44	-99	1	1	-1
COSMOS_16255	150.2252808	2.351193	2.46	22.20	2	10.5	1.34E+10	-9.70E+11	6.72E+43	-99	0	1	-1
COSMOS_16459	150.1841583	2.3535497	1.78	22.81	2	9.94	2.78E+09	-1.77E+10	2.23E+43	-99	0	1	-1
COSMOS_16650	150.187973	2.3529198	0.27	18.68	3	10.04	1.00E+09	4.45E+10	8.52E+41	1.71E+22	0	1	0
COSMOS_16957	150.208847	2.357069	1.51	21.68	2	10.21	8.72E+09	2.66E+10	-99	-99	1	-1	-1
COSMOS_16988	150.1236877	2.3582504	0.83	18.82	2	10.19	4.80E+10	4.27E+11	1.02E+44	-99	1	1	-1
COSMOS_17096	150.0368042	2.3584974	1.97	21.44	3	10.98	4.16E+09	-3.06E+11	7.44E+43	-99	0	1	-1
COSMOS_17328	150.1808929	2.3621531	1.20	21.21	2	10.19	8.95E+09	2.62E+11	-99	-99	1	-1	-1
COSMOS_17577	150.2318115	2.3639772	2.84	20.62	2	10.46	2.29E+11	6.89E+11	5.17E+44	-99	0	1	-1
COSMOS_17632	150.1502686	2.3641484	2.37	21.80	3	11.22	5.30E+09	7.16E+11	3.80E+43	-99	0	1	-1
COSMOS_17779	150.0465088	2.3673911	3.72	23.78	1	10.61	3.00E+09	1.66E+12	5.80E+43	-99	0	1	-1
COSMOS_17872	150.0522766	2.3692918	2.56	22.46	3	11.14	2.45E+09	8.43E+10	9.82E+43	-99	0	1	-1
COSMOS_19608	150.0925751	2.3827517	1.23	21.62	1	10.49	5.33E+08	-7.37E+10	-99	-99	1	-1	-1
COSMOS_19644	150.133255	2.3787253	2.13	21.83	2	10.89	6.99E+09	5.61E+11	3.22E+43	-99	0	1	-1
COSMOS_19708	150.0580597	2.3804162	0.36	17.37	1	10.95	1.86E+09	3.79E+09	1.54E+42	6.35E+22	0	1	1
COSMOS_19718	150.1370392	2.3814902	1.53	22.09	2	9.98	5.50E+09	2.93E+11	-99	-99	1	-1	-1
COSMOS_20231	150.1361084	2.3705294	0.93	19.31	3	11.02	2.21E+09	9.19E+11	-99	1.49E+23	1	-1	0
COSMOS_20310	150.0565643	2.37374	0.90	20.59	3	10.65	1.77E+09	5.84E+11	1.31E+43	-99	1	1	-1
COSMOS_20380	150.0480347	2.3737261	1.00	21.10	3	10.32	1.03E+09	3.39E+11	9.88E+42	-99	0	1	-1
COSMOS_20632	150.0671082	2.3724194	1.27	20.65	3	10.53	5.58E+09	5.43E+11	2.21E+43	-99	0	1	-1
COSMOS_20714	150.1280365	2.3694596	2.49	23.19	3	10.53	1.40E+09	1.27E+11	-99	1.17E+24	0	-1	1
CDFS_5952	53.0534477	-27.8832798	2.34	23.04	2	10.18	4.40E+09	9.91E+11	-99	-99	1	-1	-1
CDFS_6314	53.0656586	-27.8788586	2.01	21.50	1	10.81	4.25E+09	1.88E+11	3.33E+42	-99	0	1	-1
CDFS_6465	53.0760002	-27.878149	2.70	23.33	2	10.26	1.03E+10	2.95E+11	2.05E+43	-99	0	1	-1

continued ...

ID <sup>1</sup>	RA-J2000 <sup>2</sup>	Dec-J2000 <sup>3</sup>	$z_{\text{phot}}$ <sup>4</sup>	$K_{\text{Smag}}$ <sup>5</sup>	UVJ <sup>6</sup>	$\log(M_*)$ <sup>7</sup>	$\log(L_{\text{UV}})$ <sup>8</sup>	$\log(L_{\text{IR}})$ <sup>9</sup>	$\log(L_\lambda)$ <sup>10</sup>	$\log(L_{1.4\text{GHz}})$ <sup>11</sup>	IR-AGN <sup>12</sup>	X-AGN <sup>13</sup>	Rad-AGN <sup>14</sup>
CDFS_6472	53.0529709	-27.8776302	3.52	23.02	3	10.66	1.04E+10	1.85E+12	-99	-99	1	-1	-1
CDFS_6566	53.0539131	-27.8768921	2.55	22.46	2	10.66	1.27E+10	5.95E+11	1.17E+44	-99	0	1	-1
CDFS_6576	53.0923004	-27.877039	1.88	23.63	3	9.95	5.94E+08	6.60E+10	3.29E+42	-99	0	1	-1
CDFS_6761	53.0804176	-27.8720264	1.12	19.91	1	10.98	1.63E+09	8.56E+09	-99	1.60E+23	0	-1	1
CDFS_6767	53.105217	-27.8751221	2.68	22.66	3	10.87	2.03E+09	2.68E+12	2.08E+42	-99	0	1	-1
CDFS_6815	53.0760536	-27.8736057	0.71	21.04	2	9.54	2.55E+09	6.31E+10	1.76E+41	-99	0	1	-1
CDFS_6825	53.0812912	-27.8715782	1.11	20.11	3	10.85	2.94E+09	2.46E+10	-99	7.00E+23	0	-1	1
CDFS_6875	53.0706444	-27.8750248	0.79	23.28	2	8.8	1.12E+09	8.23E+09	-99	-99	1	-1	-1
CDFS_6935	53.0715332	-27.8724499	1.10	20.14	3	10.75	3.75E+09	8.20E+11	5.98E+43	3.38E+23	1	1	0
CDFS_6964	53.0793571	-27.8706779	1.85	22.54	3	9.73	6.01E+09	8.68E+10	-99	5.64E+23	1	-1	1
CDFS_7015	53.0553932	-27.8733158	3.06	23.92	3	10.32	1.70E+09	3.62E+11	-99	-99	1	-1	-1
CDFS_7341	53.0473022	-27.8704376	3.12	22.81	3	11.17	4.23E+09	3.58E+11	2.80E+44	-99	0	1	-1
CDFS_7433	53.0536385	-27.869194	1.89	22.10	3	10.48	1.82E+09	6.69E+11	3.46E+42	-99	0	1	-1
CDFS_7438	53.0742989	-27.8695717	1.85	23.20	2	10.14	3.23E+09	6.72E+10	1.28E+42	-99	0	1	-1
CDFS_7453	53.1014748	-27.8698883	3.19	24.53	3	10.3	8.16E+08	2.54E+12	-99	-99	1	-1	-1
CDFS_7652	53.0475578	-27.868618	2.95	24.49	3	9.58	8.22E+08	2.33E+12	-99	-99	1	-1	-1
CDFS_7784	53.0683975	-27.8664818	1.91	23.82	2	9.84	2.10E+09	1.63E+11	8.02E+42	-99	0	1	-1
CDFS_7867	53.0826988	-27.8665466	3.29	23.26	3	11.2	2.25E+09	8.18E+11	8.88E+42	-99	0	1	-1
CDFS_7916	53.0426445	-27.8655834	1.53	22.56	3	10.51	1.08E+09	4.67E+10	3.61E+42	-99	0	1	-1
CDFS_7932	53.0764885	-27.8641071	3.47	23.16	2	10.63	4.41E+09	2.45E+11	8.04E+42	-99	0	1	-1
CDFS_8007	53.0862732	-27.861721	0.66	19.59	2	10.08	7.85E+09	2.25E+11	1.14E+41	-99	0	1	-1
CDFS_8216	53.0383873	-27.8621101	1.43	20.79	3	10.69	5.89E+09	1.13E+12	9.63E+41	-99	1	1	-1
CDFS_8272	53.1238518	-27.8627071	2.70	23.42	3	9.95	2.43E+09	2.76E+11	4.38E+43	-99	0	1	-1
CDFS_8323	53.0647163	-27.8625278	4.64	25.29	3	10.91	2.05E+09	5.52E+12	-99	-99	1	-1	-1
CDFS_8428	53.0784569	-27.8598518	3.66	22.33	2	11.03	1.24E+10	1.88E+12	7.42E+43	1.53E+24	0	1	0
CDFS_8455	53.1026306	-27.8606205	4.19	24.14	2	10.81	4.52E+09	8.51E+12	-4.66E+42	-99	1	-1	-1
CDFS_8522	53.0624123	-27.8575153	0.67	19.17	1	10.82	2.16E+09	1.12E+10	6.78E+42	-99	0	1	-1
CDFS_8702	53.1507034	-27.8573551	1.54	21.72	3	10.46	2.64E+09	3.07E+11	6.83E+42	2.38E+23	0	1	0
CDFS_8905	53.030529	-27.8556709	1.54	20.74	3	10.71	8.86E+09	1.14E+12	2.33E+42	6.79E+23	0	1	0
CDFS_8922	53.1075554	-27.8556862	2.58	23.25	1	10.64	8.32E+08	-1.58E+11	5.73E+42	-99	0	1	-1
CDFS_9162	53.0601158	-27.8529873	1.56	20.94	2	10.8	9.91E+09	3.45E+11	6.09E+42	-99	0	1	-1
CDFS_9248	53.0916557	-27.8533459	2.36	22.93	3	10.37	1.68E+09	2.48E+12	1.39E+43	-99	0	1	-1
CDFS_9332	53.1243668	-27.8516273	3.65	22.15	2	10.91	1.62E+10	8.31E+11	1.23E+44	-99	0	1	-1
CDFS_9365	53.0619011	-27.8510456	1.59	21.81	1	10.65	9.62E+08	2.43E+10	1.94E+43	-99	0	1	-1
CDFS_9427	53.0583496	-27.8501854	0.83	20.32	3	7.91	3.52E+09	8.55E+09	2.98E+43	-99	0	1	-1
CDFS_9511	53.0707664	-27.8506699	0.97	21.97	3	9.61	1.02E+09	1.94E+11	-2.86E+41	-99	1	-1	-1

continued ...

ID <sup>1</sup>	RA-J2000 <sup>2</sup>	Dec-J2000 <sup>3</sup>	$z_{\text{phot}}$ <sup>4</sup>	$K_{\text{S, mag}}$ <sup>5</sup>	UVJ <sup>6</sup>	$\log(M_{\star})$ <sup>7</sup>	$\log(L_{\text{UV}})$ <sup>8</sup>	$\log(L_{\text{IR}})$ <sup>9</sup>	$\log(L_{\star})$ <sup>10</sup>	$\log(L_{1.4\text{GHz}})$ <sup>11</sup>	IR-AGN <sup>12</sup>	X-AGN <sup>13</sup>	Rad-AGN <sup>14</sup>
CDFS_9514	53.0887566	-27.8504448	1.81	21.98	2	10.3	6.25E+09	1.77E+11	1.95E+42	-99	0	1	-1
CDFS_9549	53.0763969	-27.8486652	1.57	20.40	1	11.06	8.17E+09	-1.26E+10	5.54E+43	4.21E+23	0	1	1
CDFS_9664	53.0717392	-27.8493862	0.90	24.09	2	8.86	7.10E+08	1.71E+09	-99	-99	1	-1	-1
CDFS_9966	53.11549	-27.8446674	1.07	19.83	3	10.66	7.99E+09	5.56E+11	2.84E+41	2.45E+23	0	1	0
CDFS_10032	53.1046066	-27.8453484	1.05	21.72	2	9.98	3.05E+09	1.73E+10	3.11E+42	-99	0	1	-1
CDFS_10096	53.1988525	-27.8438931	1.56	20.90	3	11.17	2.18E+09	6.12E+11	1.07E+43	-99	0	1	-1
CDFS_10129	53.1219978	-27.8465061	0.12	22.45	2	8.08	1.39E+07	1.34E+08	-99	-99	1	-1	-1
CDFS_10130	53.1372032	-27.8446503	2.21	21.94	2	10.19	2.18E+10	4.96E+11	8.45E+41	-99	0	1	-1
CDFS_10152	53.0702248	-27.8455219	3.77	23.36	2	10.4	9.44E+09	6.26E+11	8.36E+42	-99	0	1	-1
CDFS_10158	53.1506615	-27.8436279	1.86	21.31	1	10.94	4.38E+09	1.84E+10	1.18E+43	-99	0	1	-1
CDFS_10273	53.1644173	-27.8421612	0.58	19.84	1	10.44	4.70E+08	-2.59E+09	3.40E+41	-99	0	1	-1
CDFS_10316	53.0638428	-27.8436928	3.12	22.19	3	10.67	1.99E+10	1.12E+13	1.93E+43	1.36E+24	1	1	0
CDFS_10343	53.2017899	-27.8441277	2.91	24.55	3	10.44	5.94E+08	2.54E+12	-3.80E+42	-99	1	-1	-1
CDFS_10345	53.1314316	-27.8413181	1.59	20.79	3	11.16	2.66E+09	5.62E+11	9.34E+41	3.88E+23	0	1	0
CDFS_10584	53.1251297	-27.8407516	0.99	21.66	1	10.15	4.62E+08	-1.40E+10	2.04E+41	-99	0	1	-1
CDFS_10669	53.1450233	-27.840271	0.94	21.56	2	9.56	7.94E+09	1.45E+11	2.01E+41	-99	0	1	-1
CDFS_10776	53.1077576	-27.8388138	1.07	20.55	2	10.27	1.01E+10	2.46E+11	2.46E+41	-99	0	1	-1
CDFS_11087	53.0476837	-27.8350372	1.33	20.81	2	10.73	5.29E+09	3.66E+10	2.55E+42	-99	0	1	-1
CDFS_11172	53.1647682	-27.8368759	3.02	24.05	3	10.25	4.10E+09	8.30E+11	-99	-99	1	-1	-1
CDFS_11232	53.0409698	-27.8376446	7.54	25.90	3	11.38	6.19E+09	-99	1.08E+44	8.08E+24	1	1	0
CDFS_11252	53.0409431	-27.8360806	2.04	21.69	2	10.75	7.49E+09	4.95E+10	1.72E+42	-99	0	1	-1
CDFS_11305	53.0751266	-27.8314152	0.66	18.66	3	10.96	4.12E+09	2.73E+11	2.61E+41	4.93E+22	0	1	0
CDFS_11309	53.1039848	-27.8355694	1.07	22.66	2	9.66	1.05E+09	-4.12E+09	4.34E+42	-99	0	1	-1
CDFS_11433	53.0578651	-27.8335056	2.60	21.38	1	11.28	3.84E+09	-7.82E+10	1.83E+43	-99	0	1	-1
CDFS_11442	53.1572533	-27.8335133	1.59	20.87	3	10.66	9.55E+09	2.42E+12	4.85E+41	1.47E+24	0	1	0
CDFS_11561	53.1325188	-27.8329105	0.97	20.60	2	10.03	7.98E+09	2.20E+11	2.49E+41	-99	0	1	-1
CDFS_11568	53.2165794	-27.8342667	1.74	23.75	2	9.54	2.58E+09	1.07E+11	-99	-99	1	-1	-1
CDFS_11681	53.0939522	-27.8305073	0.72	20.09	3	10.59	4.18E+08	4.47E+10	6.18E+41	-99	0	1	-1
CDFS_11734	53.215519	-27.8308258	0.71	20.23	2	10.04	6.37E+09	2.08E+11	2.63E+41	5.08E+22	0	1	0
CDFS_11752	53.198143	-27.8320999	1.52	22.62	3	10.35	3.42E+08	-4.34E+10	2.20E+42	-99	0	1	-1
CDFS_11844	53.0673294	-27.8282661	0.66	18.78	3	10.9	3.26E+09	1.46E+11	5.00E+41	4.51E+22	0	1	0
CDFS_11990	53.107254	-27.8267612	0.57	18.59	1	10.92	2.00E+09	2.85E+10	3.47E+41	-99	0	1	-1
CDFS_12006	53.1320038	-27.8305264	2.92	26.60	2	9.89	4.55E+09	2.53E+11	-99	-99	1	-1	-1
CDFS_12213	53.1295624	-27.8276463	1.77	22.38	1	10.53	9.26E+08	-8.23E+08	5.55E+41	-99	0	1	-1
CDFS_12255	53.1852226	-27.8278313	1.01	21.01	1	10.3	1.92E+09	2.58E+09	1.50E+43	-99	0	1	-1
CDFS_12276	53.0710716	-27.8227291	0.33	18.09	1	10.48	9.33E+08	4.22E+10	1.24E+41	-99	0	1	-1

continued ...

ID <sup>1</sup>	RA-J2000 <sup>2</sup>	Dec-J2000 <sup>3</sup>	$z_{\text{phot}}$ <sup>4</sup>	$K_{\text{Smag}}$ <sup>5</sup>	UVJ <sup>6</sup>	$\log(M_*)$ <sup>7</sup>	$\log(L_{\text{UV}})$ <sup>8</sup>	$\log(L_{\text{IR}})$ <sup>9</sup>	$\log(L_\lambda)$ <sup>10</sup>	$\log(L_{1.4\text{GHz}})$ <sup>11</sup>	IR-AGN <sup>12</sup>	X-AGN <sup>13</sup>	Rad-AGN <sup>14</sup>
CDFS_12333	53.1427994	-27.8278484	3.77	23.52	3	10.27	8.92E+09	7.55E+12	-3.30E+42	-99	1	-1	-1
CDFS_12369	53.0306473	-27.8283157	3.55	23.29	2	9.84	6.39E+09	3.15E+12	9.80E+42	-99	1	1	-1
CDFS_12416	53.0923653	-27.8268051	2.72	23.13	3	10.53	2.71E+09	3.15E+12	2.67E+42	9.85E+23	0	1	0
CDFS_12428	53.0523148	-27.8272781	2.39	22.98	2	10.42	3.73E+09	9.44E+10	1.29E+42	-99	0	1	-1
CDFS_12438	53.2023239	-27.8261909	1.07	21.11	3	10.48	2.48E+08	-5.82E+12	6.84E+41	3.50E+23	0	1	0
CDFS_12441	53.1514359	-27.8258591	1.64	21.42	2	10.72	3.05E+09	2.94E+10	5.25E+41	-99	0	1	-1
CDFS_12583	53.0938873	-27.8257275	2.16	22.27	2	10.56	4.05E+09	1.25E+12	1.40E+42	-99	0	1	-1
CDFS_12751	53.0254936	-27.8243732	1.38	21.05	2	10.66	3.82E+09	1.93E+11	2.13E+43	-99	0	1	-1
CDFS_12763	53.1697731	-27.8239403	2.13	21.53	2	10.75	1.37E+10	1.04E+12	1.25E+42	-99	0	1	-1
CDFS_12803	53.0282402	-27.8226814	0.65	19.53	2	10.16	5.23E+09	1.33E+11	1.48E+41	-99	0	1	-1
CDFS_12850	53.1208305	-27.8230629	0.73	20.80	1	10.26	3.86E+08	8.57E+09	3.58E+41	-99	0	1	-1
CDFS_12862	53.1105919	-27.8236237	1.47	22.79	2	9.63	7.22E+09	3.32E+09	5.22E+41	-99	0	1	-1
CDFS_12998	53.1207771	-27.8189716	1.09	19.32	3	11.03	1.21E+10	3.55E+11	2.00E+41	-99	0	1	-1
CDFS_13086	53.1488304	-27.8211117	2.58	21.71	2	11.1	9.08E+09	6.87E+12	1.15E+43	1.08E+24	1	1	0
CDFS_13178	53.1801414	-27.8206005	2.60	21.46	2	10.38	3.08E+10	1.31E+12	2.01E+44	-99	0	1	-1
CDFS_13208	53.2331581	-27.8200817	0.83	20.42	1	10.46	1.23E+09	-6.25E+08	6.44E+41	-99	0	1	-1
CDFS_13232	53.0281754	-27.8205471	1.28	20.98	1	10.54	3.18E+09	1.82E+11	1.40E+42	-99	0	1	-1
CDFS_13269	53.1385002	-27.8211346	3.65	24.39	2	9.91	5.77E+09	-6.58E+11	9.33E+42	-99	0	1	-1
CDFS_13307	53.0694199	-27.8211536	1.59	24.26	2	9.11	1.79E+09	4.86E+10	-99	-99	1	-1	-1
CDFS_13343	53.0588989	-27.8195095	2.05	22.38	3	10.46	7.76E+09	4.71E+11	1.39E+42	1.35E+24	0	1	1
CDFS_13495	53.2259521	-27.8177071	0.99	19.99	3	10.66	3.38E+09	2.19E+11	4.71E+41	-99	0	1	-1
CDFS_13528	53.2361603	-27.8189945	1.35	23.44	2	9.1	5.79E+09	1.06E+10	-99	-99	1	-1	-1
CDFS_13529	53.0720177	-27.8189335	1.74	22.73	3	10.48	4.28E+08	7.22E+11	8.08E+41	3.98E+23	0	1	0
CDFS_13663	53.1810341	-27.8171577	1.62	21.93	3	10.61	1.91E+09	8.51E+11	6.72E+41	-99	0	1	-1
CDFS_13714	53.1416435	-27.8165684	2.53	22.89	3	11	2.01E+09	3.92E+10	1.35E+43	-99	0	1	-1
CDFS_13780	53.0456619	-27.8156052	0.88	21.95	3	9.3	4.48E+08	7.72E+10	7.56E+42	-99	1	1	-1
CDFS_13876	53.1313477	-27.8149471	1.70	21.97	3	10.61	3.24E+09	2.26E+11	3.11E+42	-99	0	1	-1
CDFS_13920	53.0558205	-27.8155937	2.69	24.04	2	10.14	1.35E+09	2.57E+11	3.26E+43	-99	0	1	-1
CDFS_13954	53.1652794	-27.8140678	3.04	21.62	2	11.12	1.51E+10	7.38E+11	2.38E+44	1.49E+24	0	1	1
CDFS_14019	53.1498795	-27.8139973	1.29	20.81	2	10.1	2.80E+10	2.84E+11	1.54E+42	-99	0	1	-1
CDFS_14074	53.0306511	-27.8141384	0.62	22.94	2	8.81	6.70E+08	4.23E+10	2.78E+41	-99	1	1	-1
CDFS_14146	53.1819878	-27.8141174	9.49	24.05	3	11.51	3.09E+10	-99	-99	-99	1	-1	-1
CDFS_14208	53.1793327	-27.8125114	1.80	21.83	1	10.61	3.47E+09	6.03E+10	3.25E+43	-99	0	1	-1
CDFS_14222	53.1975937	-27.8137417	4.16	24.89	3	10.78	1.77E+09	3.37E+12	-99	-99	1	-1	-1
CDFS_14480	53.0479012	-27.8043404	0.55	18.16	1	11.05	2.21E+09	-6.51E+08	-99	5.33E+22	0	-1	1
CDFS_14580	53.1858292	-27.8099632	2.81	22.91	2	10.56	8.84E+09	5.57E+11	4.43E+43	-99	0	1	-1

continued ...



ID <sup>1</sup>	RA-J2000 <sup>2</sup>	Dec-J2000 <sup>3</sup>	$z_{\text{phot}}$ <sup>4</sup>	$K_{\text{mag}}$ <sup>5</sup>	UVJ <sup>6</sup>	$\log(M_{\star})$ <sup>7</sup>	$\log(L_{\text{UV}})$ <sup>8</sup>	$\log(L_{\text{IR}})$ <sup>9</sup>	$\log(L_{\star})$ <sup>10</sup>	$\log(L_{1.4\text{GHz}})$ <sup>11</sup>	IR-AGN <sup>12</sup>	X-AGN <sup>13</sup>	Rad-AGN <sup>14</sup>
CDFS_14739	53.1632156	-27.8089828	2.71	22.82	1	10.6	2.60E+09	1.32E+11	7.96E+42	-99	0	1	-1
CDFS_14767	53.0999298	-27.8084373	2.01	22.48	1	10.38	1.65E+09	2.28E+08	9.52E+41	-99	0	1	-1
CDFS_15251	53.0940132	-27.8041286	2.33	22.22	3	11.09	3.15E+09	5.11E+11	1.34E+43	-99	0	1	-1
CDFS_15282	53.0734596	-27.8032875	0.75	20.59	3	10.01	5.28E+08	1.96E+10	3.29E+41	-99	0	1	-1
CDFS_15342	53.0923004	-27.803154	2.32	22.63	3	11.14	1.72E+09	1.12E+12	1.72E+43	-99	0	1	-1
CDFS_15343	53.1377563	-27.8020897	1.20	21.25	1	10.55	8.12E+08	-1.44E+10	3.99E+41	-99	0	1	-1
CDFS_15366	53.0446854	-27.8019791	0.67	19.91	3	10.16	6.84E+08	5.18E+11	1.07E+41	7.54E+22	1	1	0
CDFS_15368	53.0393562	-27.8018875	0.10	19.63	2	8.61	6.44E+07	1.38E+09	1.65E+41	-99	1	1	-1
CDFS_15467	53.1786842	-27.8026333	2.74	23.56	3	10.87	7.85E+08	1.44E+11	6.20E+42	-99	0	1	-1
CDFS_15575	53.0938072	-27.8012867	2.30	22.71	3	10.65	3.43E+09	1.65E+09	6.15E+42	6.82E+23	0	1	1
CDFS_15639	53.0927925	-27.8012276	2.94	23.42	3	10.47	2.23E+09	4.10E+10	-99	9.84E+23	0	-1	1
CDFS_15702	53.166893	-27.7987423	1.93	21.23	2	10.69	1.47E+10	2.22E+12	1.26E+42	-99	0	1	-1
CDFS_15768	53.1199493	-27.7987633	1.37	21.02	3	10.48	4.95E+09	3.95E+11	5.31E+41	-99	0	1	-1
CDFS_15910	53.0791435	-27.7987309	0.67	22.32	1	9.38	2.84E+08	1.04E+09	3.92E+42	-99	0	1	-1
CDFS_16014	53.1083183	-27.7976437	1.84	22.26	3	10.56	3.99E+09	-2.17E+13	6.15E+41	-99	0	1	-1
CDFS_16030	53.1403008	-27.7975235	1.75	22.20	1	10.44	1.60E+09	-1.83E+09	8.01E+41	-99	0	1	-1
CDFS_16050	53.0399017	-27.7984772	3.64	24.64	2	10.04	2.42E+09	-2.97E+11	1.03E+43	-99	0	1	-1
CDFS_16070	53.231266	-27.7976952	1.66	21.96	2	10.29	4.55E+09	5.09E+10	1.53E+43	-99	0	1	-1
CDFS_16167	53.0618134	-27.7939701	0.74	20.52	1	10.3	8.23E+08	-2.23E+09	1.77E+41	-99	0	1	-1
CDFS_16370	53.0853233	-27.792305	0.61	19.90	3	10.23	5.87E+08	4.97E+10	7.50E+42	-99	0	1	-1
CDFS_16440	53.0750542	-27.7884769	0.73	17.77	1	11.5	2.96E+09	4.63E+09	2.76E+41	8.38E+23	0	0	1
CDFS_16522	53.1841507	-27.7926407	0.73	20.82	2	9.69	6.85E+09	1.12E+11	1.91E+41	-99	0	1	-1
CDFS_16538	53.1491508	-27.792984	1.17	21.71	1	10.44	1.01E+09	-1.23E+10	9.18E+41	-99	0	1	-1
CDFS_16600	53.0268097	-27.7913227	1.01	19.61	3	10.77	7.96E+09	5.57E+11	4.26E+41	2.83E+23	0	1	0
CDFS_16653	53.0544739	-27.7929955	1.66	23.29	3	10.1	4.34E+08	7.60E+10	2.15E+42	-99	0	1	-1
CDFS_16665	53.1306305	-27.7902603	0.65	20.30	2	9.81	5.50E+09	9.93E+10	1.02E+41	-99	0	1	-1
CDFS_16927	53.1304436	-27.7911129	3.26	24.36	2	10.1	1.96E+09	-8.41E+10	1.74E+43	-99	0	1	-1
CDFS_17069	53.1661682	-27.7875137	1.07	20.43	2	10.28	1.08E+10	2.42E+11	1.87E+41	-99	0	1	-1
CDFS_17126	53.0479431	-27.7869606	0.61	19.34	3	10.08	2.06E+09	4.19E+11	1.02E+41	2.61E+23	0	1	0
CDFS_17232	53.2152519	-27.7876244	2.74	23.55	2	10.45	2.39E+09	-1.48E+11	3.39E+42	-99	0	1	-1
CDFS_17262	53.1651497	-27.785862	1.32	20.68	1	10.78	2.45E+09	1.62E+10	5.66E+41	-99	0	1	-1
CDFS_17495	53.0444565	-27.7867775	1.61	23.74	2	9.21	3.15E+09	4.95E+10	-99	-99	1	-1	-1
CDFS_17559	53.0916252	-27.7822056	0.67	19.04	1	10.97	1.83E+09	4.67E+10	2.55E+41	-99	0	1	-1
CDFS_17564	53.0355553	-27.780077	0.30	17.16	3	10.78	1.08E+09	1.70E+11	1.96E+41	5.76E+22	0	1	0
CDFS_17676	53.1817207	-27.7829876	1.53	22.22	2	10.04	5.46E+09	3.12E+11	6.53E+41	-99	0	1	-1
CDFS_17829	53.1784897	-27.784029	3.24	23.14	2	9.97	1.20E+10	1.64E+11	9.40E+43	-99	0	1	-1

continued ...

ID <sup>1</sup>	RA-J2000 <sup>2</sup>	Dec-J2000 <sup>3</sup>	$z_{\text{phot}}$ <sup>4</sup>	$K_{\text{Smag}}$ <sup>5</sup>	UVJ <sup>6</sup>	$\log(M_*)$ <sup>7</sup>	$\log(L_{\text{UV}})$ <sup>8</sup>	$\log(L_{\text{IR}})$ <sup>9</sup>	$\log(L_\lambda)$ <sup>10</sup>	$\log(L_{1.4\text{GHz}})$ <sup>11</sup>	IR-AGN <sup>12</sup>	X-AGN <sup>13</sup>	Rad-AGN <sup>14</sup>
CDFS_17916	53.1008263	-27.7832966	1.07	23.79	2	9.01	1.13E+09	-1.70E+10	-99	-99	1	-1	-1
CDFS_17971	52.9976616	-27.7809982	0.73	20.18	1	10.46	8.02E+08	5.79E+10	7.48E+41	-99	0	1	-1
CDFS_17974	53.0333252	-27.7825794	2.73	22.62	3	10.84	7.64E+09	2.33E+12	1.35E+44	-99	0	1	-1
CDFS_17976	53.0907364	-27.7824097	1.92	22.81	3	10.4	1.11E+09	1.37E+12	5.64E+42	-99	0	1	-1
CDFS_18009	53.0475273	-27.7805519	0.57	20.15	1	10.23	8.93E+08	-4.69E+09	9.97E+41	-99	0	1	-1
CDFS_18121	53.0058899	-27.7797279	1.85	20.12	1	11.69	5.02E+09	9.42E+10	2.17E+44	6.17E+26	0	1	1
CDFS_18192	53.1340256	-27.7809601	2.87	23.37	2	10.47	2.52E+09	1.95E+11	4.02E+43	-99	0	1	-1
CDFS_18336	53.1805038	-27.779644	2.67	23.31	3	10.43	1.96E+09	1.69E+12	2.14E+42	-99	0	1	-1
CDFS_18355	53.1009789	-27.7796154	1.87	24.00	2	9.37	3.43E+09	-6.10E+10	-99	-99	1	-1	-1
CDFS_18399	53.0222778	-27.7789021	2.83	22.06	2	11.08	5.29E+09	1.25E+11	7.52E+43	-99	0	1	-1
CDFS_18480	53.0062675	-27.7796803	1.03	22.00	3	10.16	6.44E+08	7.68E+10	-99	-99	1	-1	-1
CDFS_18548	53.0449409	-27.7743969	1.62	19.97	1	11.45	4.59E+09	1.03E+11	2.31E+42	1.80E+24	0	1	1
CDFS_18591	53.0801697	-27.7756042	0.74	19.47	1	10.79	1.22E+09	-2.13E+08	1.02E+41	-99	0	1	-1
CDFS_18617	53.0186386	-27.7786503	2.62	25.33	1	9.92	4.83E+08	1.26E+11	4.38E+43	-99	0	1	-1
CDFS_18658	53.1833878	-27.7763844	2.83	22.65	2	10.11	1.78E+10	4.76E+12	3.59E+43	-99	1	1	-1
CDFS_18701	53.1605835	-27.7761402	2.62	22.85	2	10.49	1.02E+10	5.88E+12	1.46E+42	-99	1	1	-1
CDFS_18729	53.1212196	-27.7747135	2.19	21.52	2	10.87	1.78E+10	9.40E+11	9.92E+41	-99	0	1	-1
CDFS_18738	53.0644264	-27.7753658	0.34	20.95	3	9.78	7.81E+07	4.11E+10	-2.81E+40	-99	1	-1	-1
CDFS_18748	53.065815	-27.7750416	0.98	21.26	2	9.69	1.09E+10	2.01E+11	4.62E+41	-99	0	1	-1
CDFS_18787	53.1527557	-27.7752781	0.94	21.08	2	10.15	1.97E+09	1.08E+11	2.49E+41	-99	0	1	-1
CDFS_18796	53.1930962	-27.7755585	1.26	22.27	2	10.11	9.63E+08	-1.23E+10	3.54E+43	-99	1	1	-1
CDFS_18814	53.0591545	-27.7762413	2.71	23.48	3	10.49	2.48E+09	4.49E+12	2.09E+42	-99	1	1	-1
CDFS_18843	53.0522041	-27.7747707	1.62	20.64	1	10.99	2.69E+09	1.83E+10	2.11E+42	-99	0	1	-1
CDFS_18911	53.1197319	-27.772316	0.73	19.67	1	10.75	1.29E+09	1.54E+10	1.19E+42	4.37E+23	0	1	1
CDFS_18937	53.1207466	-27.7732086	0.72	20.07	3	10.61	7.13E+08	3.52E+11	1.14E+41	-99	0	1	-1
CDFS_19033	53.1310997	-27.7731075	2.22	20.76	2	11.17	2.59E+10	1.72E+12	5.18E+42	1.39E+24	1	1	0
CDFS_19045	53.0490456	-27.774498	1.72	22.57	3	10.25	1.44E+09	2.55E+10	3.16E+43	-99	1	1	-1
CDFS_19070	53.1584435	-27.7739697	2.10	22.44	3	10.77	1.28E+09	3.75E+10	3.31E+43	-99	0	1	-1
CDFS_19111	53.0509262	-27.7724133	1.02	20.22	3	10.51	3.56E+09	2.69E+11	9.33E+42	-99	0	1	-1
CDFS_19133	53.1999817	-27.774065	4.36	24.59	3	10.5	4.26E+09	1.00E+13	-99	-99	1	-1	-1
CDFS_19214	53.1059265	-27.7714214	0.87	20.38	3	10.15	4.16E+09	2.24E+11	1.52E+41	-99	0	1	-1
CDFS_19325	53.0199051	-27.7707024	1.24	20.28	2	10.81	5.39E+09	1.62E+11	9.33E+41	-99	0	1	-1
CDFS_19487	53.1655579	-27.7697926	1.61	21.16	3	11.21	2.44E+09	8.60E+11	3.42E+43	-99	1	1	-1
CDFS_19546	53.0714912	-27.7697906	1.72	21.96	1	10.56	1.52E+09	-2.03E+10	2.18E+42	-99	0	1	-1
CDFS_19548	53.0152283	-27.7676849	0.58	18.59	1	10.95	1.74E+09	3.30E+09	1.05E+43	7.16E+22	0	1	1
CDFS_19697	53.1628494	-27.7671585	2.71	19.97	2	9.97	2.54E+11	1.83E+11	1.71E+44	-99	0	1	-1

continued ...

ID <sup>1</sup>	RA-J2000 <sup>2</sup>	Dec-J2000 <sup>3</sup>	$z_{\text{phot}}$ <sup>4</sup>	$K_{\text{smag}}$ <sup>5</sup>	UVJ <sup>6</sup>	$\log(M_{\star})$ <sup>7</sup>	$\log(L_{\text{UV}})$ <sup>8</sup>	$\log(L_{\text{IR}})$ <sup>9</sup>	$\log(L_{\star})$ <sup>10</sup>	$\log(L_{1.4\text{GHz}})$ <sup>11</sup>	IR-AGN <sup>12</sup>	X-AGN <sup>13</sup>	Rad-AGN <sup>14</sup>
CDFS_19741	53.0768661	-27.7655258	0.74	19.38	1	10.79	1.47E+09	3.04E+10	2.99E+41	-99	0	1	-1
CDFS_19742	53.098381	-27.7669525	1.07	20.87	3	10.48	9.85E+08	4.38E+11	6.83E+41	-99	0	1	-1
CDFS_19767	53.0102043	-27.7667618	1.50	20.81	3	10.8	4.47E+09	9.56E+10	4.63E+43	-99	1	1	-1
CDFS_19769	53.0939293	-27.7677288	1.93	22.16	3	10.58	5.10E+09	2.93E+11	5.54E+43	-99	0	1	-1
CDFS_19833	53.0819969	-27.7672062	2.41	22.60	3	11.09	7.10E+08	3.09E+12	2.05E+42	8.32E+23	0	1	0
CDFS_19846	53.1410179	-27.7667294	1.90	20.95	1	11.12	5.03E+09	-9.83E+09	7.95E+41	-99	0	1	-1
CDFS_19964	53.1115608	-27.7677708	4.73	24.16	3	10.77	4.56E+09	1.42E+12	6.88E+43	-99	1	1	-1
CDFS_19986	53.0964699	-27.7651825	1.20	20.91	2	10.4	4.14E+09	1.75E+11	1.49E+42	-99	0	1	-1
CDFS_20046	53.2181015	-27.7656975	1.08	21.66	2	9.93	4.16E+09	4.09E+10	1.68E+42	-99	0	1	-1
CDFS_20142	53.1191559	-27.7657623	1.84	22.53	1	10.63	4.54E+08	-6.90E+10	7.90E+41	-99	0	1	-1
CDFS_20172	53.0266991	-27.7652092	1.33	20.90	3	10.92	5.73E+08	5.77E+11	1.90E+42	-99	0	1	-1
CDFS_20182	53.1375732	-27.7631702	0.86	19.38	3	10.69	3.34E+09	2.91E+11	8.63E+42	-99	0	1	-1
CDFS_20240	53.0793228	-27.7647305	0.60	21.72	3	9.93	5.30E+07	1.34E+10	-99	-99	1	-1	-1
CDFS_20367	53.1515312	-27.7620163	0.44	20.21	3	9.3	7.22E+08	7.22E+10	-99	-99	1	-1	-1
CDFS_20429	53.0287971	-27.7635441	1.08	22.59	2	9.35	3.14E+09	2.20E+10	5.28E+41	-99	0	1	-1
CDFS_20469	53.0508118	-27.7583523	0.68	19.51	1	10.49	1.72E+09	2.24E+10	1.27E+42	-99	0	1	-1
CDFS_20565	53.2180138	-27.76161	1.43	21.12	3	10.34	1.17E+10	3.25E+12	2.39E+42	4.06E+23	1	1	0
CDFS_20613	53.0935287	-27.7621956	1.62	24.61	2	9.63	3.87E+08	1.29E+11	3.10E+42	-99	0	1	-1
CDFS_20702	53.1095543	-27.7600441	1.24	20.69	1	10.62	3.69E+09	-1.25E+10	2.75E+42	-99	0	1	-1
CDFS_20703	52.9992943	-27.7612839	2.14	23.00	1	10.55	1.10E+09	3.31E+11	-99	2.79E+24	0	-1	1
CDFS_20803	53.1249161	-27.7583008	2.07	20.03	2	10.01	1.32E+11	1.11E+12	2.40E+44	-99	0	1	-1
CDFS_20916	53.1264381	-27.756546	1.23	19.98	1	11.09	4.28E+09	9.62E+10	3.41E+41	-99	0	1	-1
CDFS_20990	53.0575867	-27.7571125	1.33	20.27	3	11.05	3.93E+09	1.17E+11	6.23E+42	-99	0	1	-1
CDFS_21045	53.0949478	-27.7578354	2.02	23.01	2	10.34	1.60E+09	2.19E+11	1.82E+42	-99	0	1	-1
CDFS_21051	53.125248	-27.7565479	0.97	20.27	3	9.96	9.08E+09	5.19E+11	9.76E+42	1.02E+23	1	1	0
CDFS_21086	53.125164	-27.757349	1.17	22.83	2	9.64	1.21E+09	6.97E+11	-99	-99	1	-1	-1
CDFS_21234	53.196537	-27.7569656	2.46	24.97	3	9.97	5.81E+08	3.95E+11	-99	-99	1	-1	-1
CDFS_21280	53.1409988	-27.7557125	2.43	22.95	2	10.23	4.81E+09	7.09E+11	1.82E+43	-99	0	1	-1
CDFS_21397	53.082531	-27.755249	2.67	23.79	3	10.34	3.63E+09	1.97E+11	5.09E+43	-99	0	1	-1
CDFS_21488	53.1283226	-27.7551556	2.76	23.74	2	9.68	6.37E+09	9.63E+10	-99	-99	1	-1	-1
CDFS_21522	52.9922295	-27.7498226	0.58	19.13	1	10.79	1.52E+09	7.42E+08	5.40E+41	-99	0	1	-1
CDFS_21537	52.9943733	-27.7545261	3.21	23.12	3	11.26	8.94E+08	3.66E+12	-99	-99	1	-1	-1
CDFS_21589	53.1081047	-27.7539825	2.73	23.22	2	10.32	3.34E+09	3.15E+10	3.36E+43	-99	0	1	-1
CDFS_21681	53.2077255	-27.7532692	2.21	24.05	2	9.53	2.81E+09	-1.84E+10	6.06E+42	-99	0	1	-1
CDFS_21715	53.1259003	-27.7512741	0.70	20.79	2	9.55	1.01E+10	1.63E+10	2.21E+43	-99	1	1	-1
CDFS_22085	53.0132713	-27.7503128	2.56	23.99	3	10.66	6.01E+08	6.96E+11	-99	-99	1	-1	-1

continued ...

ID <sup>1</sup>	RA-J2000 <sup>2</sup>	Dec-J2000 <sup>3</sup>	$z_{\text{phot}}$ <sup>4</sup>	$K_{\text{Smag}}$ <sup>5</sup>	UVJ <sup>6</sup>	$\log(M_*)$ <sup>7</sup>	$\log(L_{\text{UV}})$ <sup>8</sup>	$\log(L_{\text{IR}})$ <sup>9</sup>	$\log(L_\chi)$ <sup>10</sup>	$\log(L_{1.4\text{GHz}})$ <sup>11</sup>	IR-AGN <sup>12</sup>	X-AGN <sup>13</sup>	Rad-AGN <sup>14</sup>
CDFS_22101	53.133503	-27.7477036	0.91	20.14	1	10.63	1.93E+09	2.34E+09	5.57E+41	-99	0	1	-1
CDFS_22174	53.0601807	-27.749054	0.73	21.68	1	9.84	2.65E+08	-2.69E+09	7.81E+41	-99	0	1	-1
CDFS_22211	53.0279274	-27.7486649	2.27	22.65	2	10.55	2.44E+09	2.78E+10	6.99E+42	-99	0	1	-1
CDFS_22231	53.088707	-27.7432785	0.52	18.21	1	11	1.18E+09	3.77E+09	1.42E+41	1.87E+23	0	1	1
CDFS_22411	53.0126419	-27.7472382	2.58	22.31	2	10.67	6.16E+09	1.56E+11	5.48E+43	-99	0	1	-1
CDFS_22428	53.0835381	-27.7464371	1.93	21.98	3	8.56	5.37E+09	1.80E+12	4.56E+43	-99	1	1	-1
CDFS_22455	53.2159576	-27.7435131	0.52	18.78	3	10.66	4.12E+09	1.08E+11	-99	7.71E+22	1	-1	0
CDFS_22468	53.0240211	-27.7463646	1.67	22.85	2	10.56	1.42E+09	-7.94E+10	1.24E+43	-99	0	1	-1
CDFS_22594	53.0963631	-27.7450542	1.55	22.00	3	10.5	9.41E+08	3.59E+11	6.95E+41	-99	0	1	-1
CDFS_22607	53.063488	-27.7438641	1.10	21.59	3	10	1.48E+09	2.00E+11	4.21E+41	-99	0	1	-1
CDFS_22621	53.2169647	-27.7403145	0.53	18.46	1	11.06	1.26E+09	-1.19E+10	3.07E+41	1.21E+23	0	1	1
CDFS_22631	53.2136993	-27.7414055	0.53	18.52	1	10.87	1.11E+09	5.36E+09	3.07E+41	-99	0	1	-1
CDFS_22634	53.2201805	-27.7456799	1.78	22.63	3	10.28	2.24E+09	5.38E+11	-99	-99	1	-1	-1
CDFS_22711	53.0165901	-27.7448483	3.43	23.15	2	10.35	6.95E+09	-2.93E+11	1.83E+43	-99	0	1	-1
CDFS_22730	53.1248436	-27.7432613	0.13	23.04	1	7.64	7474000	-4.68E+08	-99	-99	1	-1	-1
CDFS_22775	53.1627121	-27.7442627	2.59	23.27	2	10.38	2.43E+09	-2.23E+11	5.30E+43	-99	0	1	-1
CDFS_22899	53.0941086	-27.7405148	0.72	19.03	3	10.59	6.82E+09	3.30E+11	8.32E+41	1.71E+23	0	1	0
CDFS_22926	53.1228409	-27.7433968	3.83	24.62	2	10.26	6.17E+09	2.21E+12	-99	-99	1	-1	-1
CDFS_23073	53.010643	-27.7416019	3.60	22.90	1	10.88	3.91E+09	3.56E+10	3.98E+43	-99	0	1	-1
CDFS_23103	53.1705894	-27.7409916	1.22	21.68	3	10.47	8.29E+08	1.75E+10	3.33E+42	-99	0	1	-1
CDFS_23120	53.1200638	-27.7321243	0.21	17.11	1	10.65	1.16E+09	2.60E+09	1.98E+41	5.20E+23	0	1	1
CDFS_23130	53.1501236	-27.7399273	1.03	21.16	2	10.01	7.59E+09	1.79E+11	3.18E+41	-99	0	1	-1
CDFS_23162	53.1271706	-27.7403431	0.92	22.67	2	9.41	1.81E+09	-2.38E+10	-99	-99	1	-1	-1
CDFS_23166	53.0837975	-27.7395687	1.16	20.61	3	10.51	3.97E+09	2.75E+11	9.00E+41	-99	0	1	-1
CDFS_23265	53.0371017	-27.7402115	2.84	23.22	1	10.54	1.47E+09	-6.99E+11	1.94E+43	-99	0	1	-1
CDFS_23360	53.1305428	-27.7386055	0.60	21.26	3	9.75	5.53E+08	3.10E+10	1.10E+41	-99	0	1	-1
CDFS_23361	53.0835838	-27.7401867	0.25	26.81	2	7.2	1.07E+07	2.95E+09	-99	5.36E+21	0	-1	1
CDFS_23408	53.1185837	-27.7387009	1.14	22.26	2	9.67	3.93E+09	4.84E+10	-99	-99	1	-1	-1
CDFS_23429	53.045475	-27.737484	3.02	20.84	3	11.42	8.31E+10	4.54E+12	5.11E+44	9.52E+25	0	1	1
CDFS_23462	53.0779343	-27.7368736	0.96	20.69	3	10.49	1.86E+09	7.07E+09	1.35E+42	-99	0	1	-1
CDFS_23463	53.1529617	-27.7351227	0.67	20.33	3	10.23	1.23E+09	1.14E+09	1.22E+43	-99	0	1	-1
CDFS_23471	53.2209015	-27.7391891	3.89	-99.00	2	10.46	2.64E+09	1.44E+12	-99	-99	1	-1	-1
CDFS_23524	53.1471825	-27.738121	1.37	23.25	2	9.52	1.41E+09	2.49E+10	-99	-99	1	-1	-1
CDFS_23541	53.1462593	-27.7362862	1.85	21.16	3	9.43	1.15E+10	4.18E+11	5.37E+42	-99	0	1	-1
CDFS_23751	53.1178436	-27.7342854	3.30	21.75	2	11.13	2.76E+10	3.66E+11	6.88E+42	-99	0	1	-1
CDFS_23850	52.995491	-27.7331085	1.31	20.54	1	10.74	2.60E+09	-1.48E+10	-99	3.14E+23	0	-1	1

continued ...

ID <sup>1</sup>	RA-J2000 <sup>2</sup>	Dec-J2000 <sup>3</sup>	$z_{\text{phot}}$ <sup>4</sup>	$K_{\text{Smag}}$ <sup>5</sup>	UVJ <sup>6</sup>	$\log(M_{\star})$ <sup>7</sup>	$\log(L_{\text{UV}})$ <sup>8</sup>	$\log(L_{\text{IR}})$ <sup>9</sup>	$\log(L_{\star})$ <sup>10</sup>	$\log(L_{1.4\text{GHz}})$ <sup>11</sup>	IR-AGN <sup>12</sup>	X-AGN <sup>13</sup>	Rad-AGN <sup>14</sup>
CDFS_23954	53.1182175	-27.7334175	0.47	22.14	3	8.94	1.30E+08	3.63E+09	-99	-99	1	-1	-1
CDFS_23961	53.0616188	-27.7340202	1.59	22.72	3	10.35	1.19E+09	1.39E+11	3.73E+42	-99	0	1	-1
CDFS_23990	53.1244316	-27.7319145	1.57	22.50	2	9.89	1.02E+10	2.09E+10	-99	-99	1	-1	-1
CDFS_24019	53.0062752	-27.7340527	4.12	24.19	3	10.75	1.41E+09	5.84E+12	4.71E+43	-99	1	1	-1
CDFS_24052	53.1744499	-27.733305	2.16	23.07	2	9.89	3.21E+09	-6.03E+10	3.84E+43	-99	0	1	-1
CDFS_24110	53.1717606	-27.7335453	2.89	25.54	3	10.07	5.33E+08	2.20E+11	-99	-99	1	-1	-1
CDFS_24283	53.1959267	-27.7295818	1.16	20.56	3	10.89	3.94E+09	8.44E+08	1.18E+43	-99	0	1	-1
CDFS_24340	53.0454559	-27.7286263	1.00	19.75	3	10.95	6.21E+09	1.63E+11	3.79E+42	-99	0	1	-1
CDFS_24402	53.1777153	-27.7300892	2.87	23.19	2	10.62	4.92E+09	1.56E+11	-99	-99	1	-1	-1
CDFS_24422	53.1548729	-27.7306824	2.72	23.78	3	10.53	6.32E+08	9.83E+11	-99	-99	1	-1	-1
CDFS_24464	53.1560097	-27.7303314	4.36	24.99	2	9.71	5.34E+09	1.04E+12	-99	-99	1	-1	-1
CDFS_24780	53.0588646	-27.7263374	1.69	22.05	3	10.76	5.52E+08	3.82E+11	-99	-99	1	-1	-1
CDFS_24930	53.1738052	-27.724474	0.98	20.61	3	10.61	1.45E+09	2.86E+11	1.08E+43	-99	0	1	-1
CDFS_24936	53.1326752	-27.7248363	0.99	21.63	1	10.3	3.64E+08	-5.04E+09	5.08E+41	-99	0	1	-1
CDFS_25000	53.0697365	-27.7243099	0.51	20.77	1	9.7	4.84E+08	4.31E+08	2.22E+41	-99	0	1	-1
CDFS_25088	53.006588	-27.724165	2.78	22.52	2	10.3	1.93E+10	1.04E+12	2.49E+44	-99	0	1	-1
CDFS_25096	53.1681099	-27.7235508	1.28	22.01	2	9.57	1.13E+10	5.41E+10	-99	-99	1	-1	-1
CDFS_25190	53.1228218	-27.7228031	1.66	21.46	2	10.69	5.14E+09	1.12E+11	4.15E+42	-99	0	1	-1
CDFS_25246	53.0014763	-27.722126	1.85	21.00	2	9.53	3.71E+10	-7.39E+10	1.65E+44	-99	0	1	-1
CDFS_25599	53.0714264	-27.7175884	0.60	19.36	2	10.34	5.02E+09	4.74E+11	1.08E+43	1.21E+23	0	1	0
CDFS_25651	53.1684074	-27.7194195	3.18	23.86	2	9.73	7.63E+09	1.17E+11	5.66E+42	-99	0	1	-1
CDFS_25715	53.1247673	-27.717104	1.37	20.91	3	10.45	6.37E+09	1.11E+12	1.01E+42	-99	0	1	-1
CDFS_25730	53.1070099	-27.7182293	1.55	21.70	3	11.06	1.33E+09	3.87E+11	5.80E+43	-99	1	1	-1
CDFS_25801	53.1507149	-27.7161865	0.93	20.76	2	9.86	1.62E+10	2.22E+11	9.48E+41	-99	0	1	-1
CDFS_25813	53.0609131	-27.7183361	3.39	25.06	3	10.33	5.78E+08	1.38E+12	-99	1.18E+24	1	-1	0
CDFS_25831	53.040432	-27.7133617	0.73	18.90	1	11.08	1.61E+09	3.79E+09	1.12E+42	4.24E+23	0	1	1
CDFS_25889	53.1853485	-27.7173233	2.37	23.23	1	10.34	1.17E+09	-3.37E+11	5.07E+42	-99	0	1	-1
CDFS_25940	53.1008224	-27.7159863	2.29	21.88	2	10.78	8.51E+09	-4.39E+10	1.47E+43	-99	0	1	-1
CDFS_25975	53.0577393	-27.713583	0.73	19.50	3	10.76	2.85E+09	1.09E+11	6.77E+42	-99	0	1	-1
CDFS_26006	53.0976486	-27.7152824	2.14	21.76	1	10.82	5.40E+09	8.23E+11	5.34E+42	-99	0	1	-1
CDFS_26007	53.1929359	-27.7143059	0.73	20.05	1	10.63	5.77E+08	-8.14E+09	4.46E+41	-99	0	1	-1
CDFS_26091	53.05513	-27.7113743	0.61	18.57	2	10.42	1.79E+10	2.89E+11	1.54E+43	9.72E+22	0	1	0
CDFS_26102	53.1971359	-27.7133102	0.73	19.49	3	10.35	4.91E+09	7.46E+11	9.62E+41	1.09E+23	0	1	0
CDFS_26107	53.0332565	-27.7109585	0.55	20.44	3	10.02	1.01E+09	3.64E+09	1.95E+42	-99	1	1	-1
CDFS_26129	53.1511765	-27.7137299	1.62	20.57	1	11.2	2.85E+09	2.64E+10	2.88E+42	-99	0	1	-1
CDFS_26136	53.0448303	-27.7096138	0.41	17.64	1	11.05	2.42E+09	2.12E+10	2.44E+41	-99	0	1	-1

continued ...

ID <sup>1</sup>	RA-J2000 <sup>2</sup>	Dec-J2000 <sup>3</sup>	$z_{\text{phot}}$ <sup>4</sup>	$K_{\text{Smag}}$ <sup>5</sup>	UVJ <sup>6</sup>	$\log(M_*)$ <sup>7</sup>	$\log(L_{\text{UV}})$ <sup>8</sup>	$\log(L_{\text{IR}})$ <sup>9</sup>	$\log(L_{\chi})$ <sup>10</sup>	$\log(L_{1.4\text{GHz}})$ <sup>11</sup>	IR-AGN <sup>12</sup>	X-AGN <sup>13</sup>	Rad-AGN <sup>14</sup>
CDFS_26333	53.1235085	-27.7118187	0.67	19.63	2	10.05	8.72E+09	1.78E+11	5.78E+41	-99	0	1	-1
CDFS_26360	53.1171761	-27.7134018	1.63	23.26	2	9.35	6.62E+09	-2.34E+10	-99	-99	1	-1	-1
CDFS_26375	53.1622925	-27.7121353	2.48	21.31	1	11.26	8.30E+09	1.28E+12	1.32E+43	-99	0	1	-1
CDFS_26483	53.083149	-27.7120056	2.35	23.30	2	10.24	1.99E+09	-6.70E+10	3.30E+43	-99	0	1	-1
CDFS_26531	53.1224403	-27.7120056	1.58	24.39	2	8.87	2.22E+09	2.92E+11	-99	-99	1	-1	-1
CDFS_26586	53.1995163	-27.7091122	1.01	19.01	3	10.98	1.81E+10	7.05E+11	1.37E+44	6.76E+23	1	1	0
CDFS_26691	53.0892601	-27.7086544	0.74	19.99	2	10.39	3.87E+09	1.59E+10	1.93E+42	-99	0	1	-1
CDFS_26715	53.0624046	-27.706913	1.90	19.52	1	11.49	2.83E+10	1.95E+11	1.89E+43	-99	0	1	-1
CDFS_26721	53.2059631	-27.7079492	0.99	20.79	3	10.37	9.93E+08	4.54E+11	-99	1.17E+25	0	-1	1
CDFS_26743	53.1386719	-27.7099915	0.92	22.45	3	10.21	4.53E+07	-1.93E+10	9.40E+42	-99	1	1	-1
CDFS_26816	53.1574249	-27.7090054	3.16	22.97	2	9.94	1.61E+10	2.41E+12	-99	-99	1	-1	-1
CDFS_26832	53.0383034	-27.7071171	0.74	20.20	1	10.5	8.54E+08	-7.46E+09	1.69E+42	-99	0	1	-1
CDFS_26855	53.0586586	-27.7083969	2.13	22.76	3	10.31	8.39E+09	6.69E+11	1.46E+43	-99	0	1	-1
CDFS_27020	53.0619926	-27.7064877	1.91	21.10	3	11.04	6.30E+09	9.31E+11	4.64E+42	-99	0	1	-1
CDFS_27025	53.0847511	-27.7079926	4.12	26.18	3	11.11	4.47E+08	-1.12E+11	5.71E+43	-99	0	1	-1
CDFS_27048	53.0543327	-27.7076931	0.84	24.56	2	8.42	2.13E+08	-1.18E+10	-99	7.55E+22	0	-1	1
CDFS_27054	52.9987755	-27.7075348	2.99	24.43	3	9.53	1.40E+09	3.41E+11	-99	-99	1	-1	-1
CDFS_27121	53.1048508	-27.7052288	0.11	20.86	3	10.7	2.20E+07	7.10E+09	1.46E+41	1.84E+21	1	0	0
CDFS_27124	53.1507492	-27.7063122	2.18	23.52	3	10.45	7.83E+08	2.42E+12	-99	5.61E+23	1	-1	0
CDFS_27198	53.1905365	-27.7036324	0.93	19.80	1	10.76	3.42E+09	1.26E+10	8.55E+42	-99	0	1	-1
CDFS_27294	52.990715	-27.7023659	0.68	19.36	1	10.75	1.71E+09	1.14E+10	4.71E+42	1.36E+23	0	1	1
CDFS_27300	53.0025787	-27.7043839	2.42	23.02	3	10.74	1.16E+09	-1.42E+11	1.96E+43	-99	0	1	-1
CDFS_27484	53.0626717	-27.7025089	2.92	22.62	2	10.39	1.91E+10	1.86E+12	-99	-99	1	-1	-1
CDFS_27516	53.1042786	-27.7026596	2.20	23.61	3	10.38	4.32E+08	2.01E+10	6.52E+42	-99	0	1	-1
CDFS_27528	53.1411591	-27.7010975	1.61	20.88	1	10.88	5.74E+09	2.42E+11	3.13E+42	-99	0	1	-1
CDFS_27539	53.1860275	-27.7006798	0.71	19.65	3	10.54	1.45E+09	2.26E+11	5.36E+41	8.93E+22	0	1	0
CDFS_27587	53.0657578	-27.7021618	2.88	23.46	2	10.08	7.87E+09	4.06E+11	2.18E+43	-99	0	1	-1
CDFS_27693	53.0809517	-27.7013264	3.54	25.10	3	10.36	1.51E+09	-6.12E+11	1.95E+43	-99	0	1	-1
CDFS_27751	53.0632477	-27.6996422	2.33	22.16	2	10.72	5.69E+09	4.25E+11	1.61E+43	-99	0	1	-1
CDFS_27758	53.0740776	-27.7001286	1.76	23.05	2	9.64	3.98E+09	-8.38E+09	-99	-99	1	-1	-1
CDFS_27809	53.1336365	-27.6986542	1.90	21.34	2	10.54	1.24E+10	9.00E+11	2.96E+43	-99	0	1	-1
CDFS_27973	53.0344429	-27.6982098	2.63	23.21	2	10.43	3.48E+09	5.52E+10	1.37E+43	-99	0	1	-1
CDFS_27977	53.1996422	-27.6966267	0.19	19.74	3	8.75	2.53E+08	5.16E+07	1.77E+42	-99	1	1	-1
CDFS_27992	53.1103096	-27.6980591	1.29	23.04	2	9.85	1.02E+09	1.58E+10	-99	-99	1	-1	-1
CDFS_28002	53.111515	-27.6959858	0.76	19.85	3	10.33	2.26E+09	7.84E+10	6.93E+42	-99	1	1	-1
CDFS_28083	53.0527344	-27.6969643	1.55	22.83	3	10.18	9.44E+08	-9.24E+10	4.47E+42	-99	0	1	-1

continued ...

ID <sup>1</sup>	RA-J2000 <sup>2</sup>	Dec-J2000 <sup>3</sup>	$z_{\text{phot}}$ <sup>4</sup>	$K_{\text{S, mag}}$ <sup>5</sup>	UVJ <sup>6</sup>	$\log(M_{\star})$ <sup>7</sup>	$\log(L_{\text{UV}})$ <sup>8</sup>	$\log(L_{\text{IR}})$ <sup>9</sup>	$\log(L_{\star})$ <sup>10</sup>	$\log(L_{1.4\text{GHz}})$ <sup>11</sup>	IR-AGN <sup>12</sup>	X-AGN <sup>13</sup>	Rad-AGN <sup>14</sup>
CDFS_28088	53.1150894	-27.6958065	0.67	19.97	3	10.16	2.40E+09	1.52E+10	1.88E+43	-99	1	1	-1
CDFS_28258	53.1010628	-27.6906738	0.53	18.93	1	10.77	1.54E+09	1.70E+09	4.05E+42	-99	0	1	-1
CDFS_28291	53.0060501	-27.6940861	1.43	21.47	3	10.65	2.61E+09	4.34E+11	8.91E+43	-99	1	1	-1
CDFS_28412	53.082531	-27.6896496	0.23	17.91	1	10.16	1.59E+09	3.07E+10	1.33E+41	2.40E+22	0	1	0
CDFS_28439	53.07127	-27.6935787	2.12	22.70	3	10.54	1.82E+09	2.86E+09	3.53E+43	-99	0	1	-1
CDFS_28446	53.1557465	-27.6906166	0.67	18.14	1	11.38	2.74E+09	-1.80E+09	5.90E+41	-99	0	1	-1
CDFS_28635	53.0202141	-27.6909275	1.54	21.86	2	10.52	4.71E+09	5.08E+11	5.02E+43	3.04E+23	0	1	0
CDFS_28670	53.1374283	-27.6880722	1.06	19.15	1	11.28	4.32E+09	1.93E+11	2.06E+42	-99	0	1	-1
CDFS_28904	53.1125221	-27.6847229	2.62	18.40	2	10.08	9.97E+11	1.30E+11	2.83E+45	-99	0	1	-1
CDFS_29064	53.1489868	-27.6865463	1.70	23.46	2	9.81	1.59E+09	1.96E+11	-99	-99	1	-1	-1
CDFS_29152	53.1040878	-27.6837559	0.74	19.83	2	10.21	4.93E+09	9.02E+10	1.06E+43	-99	0	1	-1
CDFS_29192	53.1456223	-27.6852436	2.86	23.72	2	9.63	9.75E+09	9.55E+10	-99	-99	1	-1	-1
CDFS_29209	53.1493378	-27.6831913	0.73	19.93	3	10.52	2.18E+09	-4.77E+09	5.37E+42	-99	0	1	-1
CDFS_29228	53.110775	-27.6843128	1.06	22.69	2	9.6	2.06E+09	8.81E+10	-99	-99	1	-1	-1
CDFS_29316	53.1352539	-27.6823826	1.29	21.05	2	10.27	7.34E+09	6.44E+10	-99	-99	1	-1	-1
CDFS_29318	53.1891899	-27.6824169	0.73	20.49	1	10.41	3.71E+08	7.19E+09	8.85E+41	-99	0	1	-1
CDFS_29364	53.0807686	-27.6809959	0.69	19.30	3	10.53	3.22E+09	4.69E+11	8.17E+41	8.16E+22	1	1	0
CDFS_29483	53.1110115	-27.6812611	1.20	23.33	2	9.33	2.48E+09	2.21E+10	-99	-99	1	-1	-1
CDFS_29639	53.1103897	-27.6765385	2.62	19.20	3	11.1	6.19E+11	7.05E+12	7.22E+44	8.01E+23	1	1	0
CDFS_29829	53.101017	-27.6766758	1.63	24.28	2	9.18	2.04E+09	5.96E+10	-99	-99	1	-1	-1
CDFS_29924	53.1243858	-27.6751518	1.43	22.80	2	9.66	3.11E+09	7.05E+10	-99	-99	1	-1	-1
CDFS_30130	53.1110992	-27.6704178	1.69	21.67	2	10.6	1.04E+10	5.06E+11	1.05E+44	-99	1	1	-1
CDFS_30143	53.1022568	-27.6695728	0.95	20.27	3	10.38	3.19E+09	2.29E+11	5.26E+42	1.08E+23	1	1	0
CDFS_30290	53.1560707	-27.6666927	0.68	20.73	2	9.65	3.26E+09	-1.25E+10	8.18E+42	-99	0	1	-1
CDFS_30311	53.1038895	-27.6676178	2.85	24.14	2	10.33	1.48E+09	8.14E+08	-99	-99	1	-1	-1
CDFS_30389	53.1143417	-27.6597404	1.18	22.85	2	9.45	1.61E+09	3.02E+10	-99	-99	1	-1	-1
CDFS_30472	53.1856079	-27.6641083	0.58	21.19	1	9.84	3.70E+08	-2.26E+09	2.44E+42	-99	0	1	-1
CDFS_30584	53.1015358	-27.6629791	3.77	24.11	1	10.67	2.13E+09	5.91E+12	-99	-99	1	-1	-1
CDFS_30617	53.1434441	-27.6536102	1.57	-99.00	1	11.28	4.51E+09	-1.84E+10	1.54E+44	-99	0	1	-1
CDFS_30708	53.1670494	-27.6596069	0.74	19.82	3	10.57	7.59E+08	8.69E+10	1.77E+43	-99	1	1	-1
CDFS_30724	53.1234016	-27.6634235	1.80	24.33	2	9.66	9.91E+08	2.75E+10	-99	-99	1	-1	-1
CDFS_30761	53.1397858	-27.6580124	0.96	20.79	2	10.01	6.72E+09	5.93E+11	-99	1.28E+23	1	-1	0
CDFS_30781	53.1588287	-27.6624489	2.63	19.74	2	10.92	3.50E+11	6.99E+09	1.19E+45	-99	0	1	-1
CDFS_30842	53.1298218	-27.6549664	1.11	20.43	3	10.1	6.13E+09	3.99E+11	1.29E+43	2.37E+23	0	1	0
UDS_1154	34.3220558	-5.3002253	1.56	22.07	2	10.37	1.20E+10	5.39E+11	-99	-99	1	-1	-1
UDS_1582	34.2669067	-5.2949014	2.84	23.48	2	10.55	5.83E+09	-4.37E+11	1.06E+45	-99	0	1	-1

continued ...

ID <sup>1</sup>	RA-J2000 <sup>2</sup>	Dec-J2000 <sup>3</sup>	$z_{\text{phot}}$ <sup>4</sup>	$K_{\text{Smag}}$ <sup>5</sup>	UVJ <sup>6</sup>	$\log(M_*)$ <sup>7</sup>	$\log(L_{\text{UV}})$ <sup>8</sup>	$\log(L_{\text{IR}})$ <sup>9</sup>	$\log(L_{\chi})$ <sup>10</sup>	$\log(L_{1.4\text{GHz}})$ <sup>11</sup>	IR-AGN <sup>12</sup>	X-AGN <sup>13</sup>	Rad-AGN <sup>14</sup>
UDS_1708	34.2725525	-5.2939501	1.46	22.86	3	10.35	5.11E+08	-7.20E+10	-99	-99	1	-1	-1
UDS_1792	34.2671967	-5.2919302	1.87	22.17	3	10.55	6.69E+09	1.06E+12	-99	-99	1	-1	-1
UDS_2034	34.3655586	-5.2889066	3.98	21.63	2	10.43	1.36E+11	1.82E+12	-99	-99	1	-1	-1
UDS_2093	34.3650017	-5.2879133	1.40	22.30	2	9.82	7.63E+09	1.86E+10	-99	-99	1	-1	-1
UDS_2164	34.2715721	-5.2871718	1.73	22.16	2	10.44	6.50E+09	-5.49E+09	-99	-99	1	-1	-1
UDS_2183	34.3950043	-5.2882314	1.51	24.85	2	8.85	9.60E+08	1.16E+10	8.73E+44	-99	0	1	-1
UDS_2215	34.2796326	-5.286592	1.43	22.59	3	10.28	1.25E+09	2.57E+11	-99	-99	1	-1	-1
UDS_2653	34.2968407	-5.2805319	0.80	20.82	3	10.12	4.53E+08	4.52E+11	-99	-99	1	-1	-1
UDS_2717	34.2826118	-5.2800627	1.01	21.00	3	10.45	3.80E+09	6.09E+10	-99	-99	1	-1	-1
UDS_2789	34.3501778	-5.2790871	1.22	21.80	2	10.33	2.78E+09	5.09E+09	-99	-99	1	-1	-1
UDS_3093	34.271286	-5.2747836	0.81	19.79	2	9.88	2.26E+10	1.50E+10	-99	-99	1	-1	-1
UDS_3221	34.3857574	-5.2748122	0.95	21.49	2	9.78	2.92E+09	5.52E+09	-99	-99	1	-1	-1
UDS_3378	34.2611656	-5.2717752	0.63	20.45	3	10.13	3.89E+08	1.55E+11	-99	1.20E+24	0	-1	1
UDS_3446	34.3546181	-5.2715826	1.93	21.52	3	10.9	3.78E+09	4.34E+11	-99	1.65E+24	1	-1	1
UDS_3471	34.2641792	-5.2721095	2.13	23.32	2	10.17	3.57E+09	2.66E+10	-99	-99	1	-1	-1
UDS_3944	34.3450508	-5.2667303	2.95	23.80	3	10.79	1.07E+09	4.53E+11	-99	-99	1	-1	-1
UDS_3986	34.2503929	-5.2660646	1.50	23.49	2	9.63	5.62E+09	6.75E+10	-99	-99	1	-1	-1
UDS_4158	34.2565842	-5.2635937	1.62	21.83	3	10.34	6.01E+09	9.63E+11	-99	-99	1	-1	-1
UDS_4184	34.3041229	-5.2639399	1.54	22.50	3	10.25	7.04E+08	5.25E+10	-99	-99	1	-1	-1
UDS_4305	34.3182411	-5.2620516	0.94	21.35	2	10	1.64E+09	2.39E+09	-99	-99	1	-1	-1
UDS_4392	34.214077	-5.2605748	2.44	22.02	3	11.02	6.56E+09	2.17E+12	-99	-99	1	-1	-1
UDS_4621	34.2698631	-5.2550197	1.26	19.36	1	11.43	3.49E+09	-3.93E+10	-99	2.22E+24	0	-1	1
UDS_4730	34.3315239	-5.2576308	1.30	21.49	2	10.38	1.70E+09	1.08E+11	4.04E+44	-99	1	1	-1
UDS_4841	34.3040237	-5.2572227	2.29	22.88	3	10.77	1.45E+09	9.65E+10	-99	-99	1	-1	-1
UDS_5322	34.3652306	-5.2507448	3.19	21.22	2	10.9	5.49E+10	6.18E+12	3.07E+45	-99	1	1	-1
UDS_5371	34.3365707	-5.2519212	4.03	23.66	3	11.46	2.14E+09	-5.55E+11	-99	-99	1	-1	-1
UDS_5680	34.3702888	-5.2469001	0.99	19.58	3	10.77	4.93E+09	4.37E+11	-99	-99	1	-1	-1
UDS_5861	34.2881393	-5.2454901	1.34	21.81	2	10.35	4.95E+09	3.55E+11	-99	-99	1	-1	-1
UDS_5967	34.3773766	-5.2463422	1.29	22.83	2	9.73	5.78E+08	7.29E+10	-99	-99	1	-1	-1
UDS_5992	34.2280617	-5.2454195	1.46	22.27	3	10.28	7.77E+08	-1.80E+09	-99	-99	1	-1	-1
UDS_6097	34.3347054	-5.2434988	0.88	20.32	3	10.6	2.40E+09	9.08E+09	-99	-99	1	-1	-1
UDS_6391	34.3209381	-5.2422237	1.69	22.40	2	10.07	5.16E+09	-1.20E+11	-99	-99	1	-1	-1
UDS_6566	34.3581924	-5.2409115	3.79	23.50	3	10.99	5.29E+09	8.13E+11	-99	9.85E+24	1	-1	1
UDS_6719	34.2514267	-5.2375641	1.04	21.06	3	10.09	2.84E+09	1.53E+11	-99	-99	1	-1	-1
UDS_6728	34.2373924	-5.2393541	1.50	23.61	2	9.41	1.89E+09	3.13E+10	-99	-99	1	-1	-1
UDS_6897	34.3876381	-5.238349	2.03	23.45	3	10.56	1.93E+08	1.48E+11	-99	-99	1	-1	-1

continued ...



ID <sup>1</sup>	RA-J2000 <sup>2</sup>	Dec-J2000 <sup>3</sup>	$z_{\text{phot}}$ <sup>4</sup>	$K_{\text{smag}}$ <sup>5</sup>	UVJ <sup>6</sup>	$\log(M_{\star})$ <sup>7</sup>	$\log(L_{\text{UV}})$ <sup>8</sup>	$\log(L_{\text{IR}})$ <sup>9</sup>	$\log(L_{\star})$ <sup>10</sup>	$\log(L_{1.4\text{GHz}})$ <sup>11</sup>	IR-AGN <sup>12</sup>	X-AGN <sup>13</sup>	Rad-AGN <sup>14</sup>
UDS_6991	34.4151268	-5.2364745	2.64	23.01	3	10.77	1.98E+09	2.19E+11	-99	-99	1	-1	-1
UDS_7048	34.3040466	-5.2366853	3.77	22.35	3	11.25	1.29E+10	4.58E+12	-99	-99	1	-1	-1
UDS_7429	34.3924217	-5.2275615	0.43	18.23	1	10.78	1.05E+09	1.13E+10	-99	3.02E+23	0	-1	1
UDS_7926	34.2422981	-5.2274261	1.48	21.77	2	10.51	5.09E+09	4.85E+10	-99	-99	1	-1	-1
UDS_8010	34.2788544	-5.2266426	2.06	21.04	3	11.21	5.65E+09	-3.49E+10	-99	2.04E+24	0	-1	1
UDS_8017	34.2365799	-5.2276592	1.53	22.55	2	9.81	3.72E+09	-9.60E+10	-99	-99	1	-1	-1
UDS_8055	34.3835373	-5.2256093	2.73	19.93	2	11.07	2.06E+11	8.91E+12	3.73E+45	-99	0	1	-1
UDS_8144	34.2604485	-5.2268071	1.07	21.98	3	10.21	2.73E+08	2.71E+10	-99	-99	1	-1	-1
UDS_8367	34.3441505	-5.2248378	0.46	22.46	2	8.48	5.63E+08	-1.42E+10	-99	-99	1	-1	-1
UDS_8462	34.3481789	-5.2222924	2.13	22.44	2	10.59	7.08E+09	4.33E+11	-99	-99	1	-1	-1
UDS_8512	34.3241501	-5.2233133	1.27	21.70	3	10.4	9.14E+08	2.60E+11	-99	-99	1	-1	-1
UDS_8833	34.2261963	-5.2212844	2.49	23.84	3	10.62	7.20E+08	-1.06E+11	-99	-99	1	-1	-1
UDS_8863	34.2937202	-5.2207026	0.61	22.39	2	9.29	1.38E+08	-5.25E+09	-99	-99	1	-1	-1
UDS_8999	34.4188309	-5.2196445	3.01	23.35	3	11.31	1.30E+09	1.22E+12	-99	-99	1	-1	-1
UDS_9097	34.351635	-5.2145	0.90	18.66	1	11.22	3.65E+09	-4.97E+10	-99	1.24E+25	0	-1	1
UDS_9282	34.4115677	-5.2159209	3.84	19.99	3	11.12	5.06E+11	5.34E+12	8.22E+45	-99	0	1	-1
UDS_9408	34.4077835	-5.2153516	1.00	21.36	3	9.97	3.32E+09	-2.99E+10	-99	-99	1	-1	-1
UDS_9440	34.3148613	-5.2158008	1.10	23.09	2	9.19	5.00E+09	9.71E+09	-99	-99	1	-1	-1
UDS_9757	34.2959709	-5.212636	2.87	23.52	2	10.62	5.24E+09	2.58E+10	-99	-99	1	-1	-1
UDS_10547	34.3756256	-5.2040067	0.89	20.44	3	10.52	4.06E+09	9.09E+10	-99	-99	1	-1	-1
UDS_10681	34.2858925	-5.2045774	1.62	22.41	2	10.04	7.84E+09	7.59E+10	-99	-99	1	-1	-1
UDS_10797	34.3071747	-5.2016196	1.05	21.50	2	10.1	3.60E+09	8.39E+10	-99	-99	1	-1	-1
UDS_10823	34.324295	-5.2013721	1.09	20.23	3	10.79	4.11E+09	2.83E+10	-99	-99	1	-1	-1
UDS_10945	34.2568436	-5.2014985	0.45	21.24	3	8.61	4.55E+08	2.21E+11	-99	-99	1	-1	-1
UDS_11046	34.2652397	-5.2011952	2.22	21.97	3	10.99	7.23E+09	1.11E+12	-99	-99	1	-1	-1
UDS_11136	34.4066734	-5.1988201	0.89	19.88	3	10.56	3.92E+09	3.34E+11	-99	-99	1	-1	-1
UDS_11156	34.3620949	-5.1994529	0.60	21.14	3	9.75	6.71E+08	7.03E+10	-99	-99	1	-1	-1
UDS_11259	34.2821846	-5.1991668	1.47	22.04	3	10.44	1.13E+09	1.83E+11	-99	-99	1	-1	-1
UDS_11392	34.2277565	-5.1977096	1.61	23.05	2	9.87	4.13E+09	-2.05E+10	-99	-99	1	-1	-1
UDS_11402	34.3222008	-5.198009	1.09	22.01	2	9.81	2.43E+09	5.30E+10	-99	-99	1	-1	-1
UDS_11429	34.3721008	-5.1979094	2.90	22.77	3	10.75	6.55E+09	4.94E+12	-99	-99	1	-1	-1
UDS_11442	34.2238655	-5.1970391	1.51	21.58	2	10.49	4.08E+09	1.71E+11	-99	-99	1	-1	-1
UDS_11477	34.2490768	-5.1979866	3.82	24.08	3	10.94	1.20E+09	1.20E+11	-99	-99	1	-1	-1
UDS_11501	34.2714424	-5.1975045	1.76	22.53	2	10.01	6.04E+09	1.36E+10	-99	-99	1	-1	-1
UDS_11564	34.2301407	-5.1963148	2.85	21.43	2	10.28	1.00E+11	3.19E+11	2.17E+45	-99	0	1	-1
UDS_11785	34.4002914	-5.1952028	1.46	22.79	3	9.82	1.14E+09	5.64E+11	-99	-99	1	-1	-1

continued ...

ID <sup>1</sup>	RA-J2000 <sup>2</sup>	Dec-J2000 <sup>3</sup>	$z_{\text{phot}}$ <sup>4</sup>	$K_{\text{Smag}}$ <sup>5</sup>	UVJ <sup>6</sup>	$\log(M_*)$ <sup>7</sup>	$\log(L_{\text{UV}})$ <sup>8</sup>	$\log(L_{\text{IR}})$ <sup>9</sup>	$\log(L_{\lambda})$ <sup>10</sup>	$\log(L_{1.4\text{GHz}})$ <sup>11</sup>	IR-AGN <sup>12</sup>	X-AGN <sup>13</sup>	Rad-AGN <sup>14</sup>
UDS_11841	34.2855072	-5.1936102	1.66	21.94	3	10.45	5.58E+09	4.70E+10	-99	-99	1	-1	-1
UDS_12000	34.2736549	-5.1921086	1.32	20.14	1	10.94	6.72E+09	9.72E+10	-99	-99	1	-1	-1
UDS_12046	34.2911987	-5.1914816	0.85	21.74	3	10.05	3.11E+08	6.41E+10	-99	-99	1	-1	-1
UDS_12103	34.2196236	-5.1913152	1.76	21.49	3	10.69	4.87E+09	3.46E+12	-99	-99	1	-1	-1
UDS_12109	34.4125481	-5.1906953	0.88	20.99	2	9.96	4.83E+09	1.00E+11	-99	-99	1	-1	-1
UDS_12185	34.3510399	-5.1904788	1.38	21.88	2	10.18	6.82E+09	2.91E+11	-99	-99	1	-1	-1
UDS_12313	34.4181404	-5.1879816	1.43	20.25	3	10.99	6.98E+09	1.45E+12	-99	-99	1	-1	-1
UDS_12496	34.2491264	-5.1830015	0.60	18.13	1	11.17	2.01E+09	-1.96E+10	-99	3.72E+23	0	-1	1
UDS_12596	34.3630981	-5.1874089	0.48	23.59	2	8.3	9.15E+07	2.46E+09	-99	-99	1	-1	-1
UDS_12626	34.2296219	-5.1864638	0.28	21.72	3	7.99	9.34E+07	1.25E+10	-99	-99	1	-1	-1
UDS_12665	34.2476807	-5.1820383	0.63	20.59	2	9.55	4.48E+09	9.58E+10	-99	-99	1	-1	-1
UDS_12853	34.220726	-5.1847715	1.44	22.64	3	10.19	1.07E+09	-2.34E+11	-99	-99	1	-1	-1
UDS_12943	34.2205925	-5.183166	0.16	20.62	3	8.27	3.83E+07	-1.23E+09	1.22E+43	-99	1	1	-1
UDS_12989	34.411541	-5.1838326	1.38	22.25	3	10.21	1.68E+09	-1.95E+10	-99	-99	1	-1	-1
UDS_13185	34.4104004	-5.1821213	5.03	23.68	3	10.97	8.26E+09	-99	-99	-99	1	-1	-1
UDS_13410	34.342926	-5.1773667	1.04	19.56	3	11.16	1.25E+09	1.37E+12	-99	4.09E+23	1	-1	0
UDS_13764	34.2210884	-5.1766696	1.46	22.89	2	9.89	2.80E+09	6.61E+10	-99	-99	1	-1	-1
UDS_13780	34.2192764	-5.1769042	1.50	22.54	2	9.96	3.10E+09	1.53E+10	-99	-99	1	-1	-1
UDS_13873	34.2501068	-5.1767755	0.67	24.80	2	8.32	3.00E+07	3.21E+09	5.50E+43	-99	0	1	-1
UDS_13880	34.3877716	-5.1753907	1.43	21.39	3	10.52	3.71E+09	1.09E+12	-99	-99	1	-1	-1
UDS_14327	34.3776436	-5.1715641	1.68	22.22	3	10.39	2.06E+09	-1.83E+11	8.84E+44	-99	1	1	-1
UDS_14394	34.4157639	-5.1718736	2.75	22.26	3	11.15	3.72E+09	1.31E+12	-99	-99	1	-1	-1
UDS_14539	34.3156662	-5.170496	2.91	22.86	2	10.37	1.09E+10	8.00E+11	1.87E+45	-99	0	1	-1
UDS_14544	34.2725449	-5.1673002	0.90	19.01	1	11.22	3.65E+09	-5.07E+09	-99	1.21E+24	0	-1	1
UDS_14636	34.2359505	-5.1681414	0.24	20.62	3	8.31	3.43E+08	9.23E+08	-99	-99	1	-1	-1
UDS_14668	34.2353859	-5.168025	1.37	20.98	3	10.85	3.72E+09	2.48E+12	-99	-99	1	-1	-1
UDS_14736	34.2379303	-5.1675501	0.82	20.71	3	10.3	5.66E+08	-3.50E+08	-99	-99	1	-1	-1
UDS_14906	34.3167534	-5.1668143	1.01	22.20	3	9.97	3.27E+08	1.51E+11	-99	-99	1	-1	-1
UDS_14929	34.3534851	-5.1660438	1.02	20.80	3	10.55	2.26E+09	3.45E+10	8.14E+43	-99	0	1	-1
UDS_15245	34.2356644	-5.1639676	1.31	22.05	2	10.21	2.56E+09	-5.77E+10	-99	-99	1	-1	-1
UDS_15420	34.2371292	-5.1622796	1.26	21.88	3	10.25	1.52E+09	1.18E+10	-99	-99	1	-1	-1
UDS_15587	34.2178307	-5.1603322	0.63	21.81	3	9.61	2.29E+07	-5.74E+09	-99	-99	1	-1	-1
UDS_15665	34.2686348	-5.1594467	1.22	20.69	1	10.59	4.68E+09	-5.76E+10	-99	-99	1	-1	-1
UDS_15883	34.4113464	-5.1576929	0.89	21.46	3	9.88	9.84E+08	-1.31E+10	-99	-99	1	-1	-1
UDS_15898	34.2722359	-5.1571245	2.21	21.49	3	10.81	7.33E+09	4.28E+12	-99	2.44E+24	1	-1	0
UDS_16040	34.2674255	-5.156116	1.06	21.52	3	10.15	2.22E+09	8.58E+09	-99	-99	1	-1	-1

continued ...

ID <sup>1</sup>	RA-J2000 <sup>2</sup>	Dec-J2000 <sup>3</sup>	$z_{\text{phot}}$ <sup>4</sup>	$K_{\text{mag}}$ <sup>5</sup>	UVJ <sup>6</sup>	$\log(M_{\star})$ <sup>7</sup>	$\log(L_{\text{UV}})$ <sup>8</sup>	$\log(L_{\text{IR}})$ <sup>9</sup>	$\log(L_{\text{X}})$ <sup>10</sup>	$\log(L_{1.4\text{GHz}})$ <sup>11</sup>	IR-AGN <sup>12</sup>	X-AGN <sup>13</sup>	Rad-AGN <sup>14</sup>
UDS_16514	34.3398666	-5.1496196	1.90	20.33	2	11.27	1.70E+10	2.59E+12	1.10E+45	1.83E+24	0	1	0
UDS_16555	34.3063011	-5.1508827	1.47	20.82	3	10.99	3.32E+09	1.40E+12	-99	-99	1	-1	-1
UDS_16767	34.2552185	-5.1497107	1.44	22.40	2	9.95	7.42E+09	8.30E+10	-99	-99	1	-1	-1
UDS_16790	34.3365517	-5.1489959	1.87	21.15	2	10.8	9.46E+09	1.08E+11	-99	-99	1	-1	-1
UDS_16880	34.2411652	-5.149343	1.65	22.98	2	9.66	7.18E+09	-2.99E+10	-99	-99	1	-1	-1
UDS_17062	34.4000359	-5.1479893	1.70	23.27	2	9.71	2.45E+09	-2.46E+11	-99	-99	1	-1	-1
UDS_17313	34.304554	-5.1453228	2.11	23.47	3	10.33	1.33E+09	8.75E+10	-99	-99	1	-1	-1
UDS_17342	34.3979645	-5.144412	1.48	22.41	3	10.06	1.28E+09	6.16E+11	-99	-99	1	-1	-1
UDS_17393	34.3691597	-5.1424632	0.20	21.13	2	7.64	1.10E+09	2.27E+10	-99	-99	1	-1	-1
UDS_17438	34.4107933	-5.1418824	1.31	21.13	3	10.43	6.80E+09	3.51E+12	-99	-99	1	-1	-1
UDS_17495	34.3373032	-5.1436462	2.35	21.63	1	11.2	1.83E+09	7.71E+11	-99	-99	1	-1	-1
UDS_17711	34.2841263	-5.1404157	1.66	20.87	1	11.11	2.24E+09	4.80E+10	-99	2.75E+24	0	-1	1
UDS_17757	34.411808	-5.1387281	0.94	21.14	2	10.02	9.06E+09	1.65E+11	-99	-99	1	-1	-1
UDS_17912	34.4100609	-5.1393723	0.12	21.01	3	7.74	5.93E+07	1.06E+08	-99	-99	1	-1	-1
UDS_18455	34.3455696	-5.1336098	1.52	22.22	3	10.38	8.14E+08	9.99E+11	-99	-99	1	-1	-1
UDS_18548	34.2767448	-5.133606	3.40	25.10	2	9.63	1.62E+09	-2.20E+12	4.08E+45	-99	0	1	-1
UDS_18686	34.3893814	-5.1298189	0.68	20.39	3	9.68	1.47E+09	1.49E+11	-99	-99	1	-1	-1
UDS_18689	34.2956314	-5.1279716	0.81	18.81	3	10.84	7.31E+09	9.18E+11	-99	3.27E+23	1	-1	0
UDS_18778	34.4156761	-5.1302314	1.62	22.86	2	9.77	4.12E+09	-1.90E+11	-99	-99	1	-1	-1
UDS_19378	34.3333397	-5.1183152	1.00	21.31	3	10.09	8.76E+08	2.32E+11	-99	-99	1	-1	-1
UDS_19450	34.2413521	-5.0943031	0.81	20.79	3	9.92	2.93E+09	1.60E+11	-99	-99	1	-1	-1
UDS_19454	34.3798523	-5.1192837	1.33	19.57	3	11.02	1.40E+10	7.46E+12	-99	6.14E+24	1	-1	0
UDS_19477	34.3774338	-5.1186557	1.55	22.25	2	9.89	1.06E+10	-1.36E+11	-99	-99	1	-1	-1
UDS_19481	34.3660774	-5.1178484	0.81	20.86	3	9.71	4.13E+09	2.75E+11	-99	-99	1	-1	-1
UDS_19596	34.401638	-5.1224065	1.47	23.92	2	9.1	8.34E+09	-6.48E+10	-99	-99	1	-1	-1
UDS_19868	34.4097672	-5.1132174	0.80	21.14	3	9.65	2.30E+09	1.13E+11	-99	-99	1	-1	-1
UDS_20062	34.3343277	-5.1235304	1.41	22.07	3	10.15	3.36E+09	2.13E+11	-99	-99	1	-1	-1
UDS_20450	34.2926826	-5.1044464	1.36	22.30	3	10.34	2.03E+09	8.52E+11	-99	-99	1	-1	-1
UDS_20659	34.2915993	-5.0999055	1.30	22.65	2	9.87	1.48E+09	-7.60E+10	-99	-99	1	-1	-1
UDS_20671	34.2361145	-5.0958691	3.05	23.07	3	10.54	1.74E+09	4.75E+11	-99	-99	1	-1	-1
UDS_20866	34.2356148	-5.0966344	1.55	23.10	3	10	1.05E+09	5.38E+11	-99	-99	1	-1	-1
UDS_20944	34.3554153	-5.1124902	2.24	22.79	2	10.18	5.70E+09	1.02E+11	-99	-99	1	-1	-1
UDS_21132	34.306469	-5.1113768	2.44	22.44	1	10.88	1.88E+09	-9.10E+10	-99	5.67E+24	0	-1	1
UDS_21161	34.2182808	-5.1118188	1.40	22.56	2	9.85	2.32E+09	5.18E+10	-99	-99	1	-1	-1
UDS_21310	34.2448235	-5.1027613	1.77	22.22	2	9.88	1.19E+10	1.64E+11	-99	-99	1	-1	-1
UDS_21383	34.3547058	-5.1097341	3.40	23.79	3	11.09	2.05E+09	-1.04E+10	-99	-99	1	-1	-1

continued ...

ID <sup>1</sup>	RA-J2000 <sup>2</sup>	Dec-J2000 <sup>3</sup>	$z_{\text{phot}}$ <sup>4</sup>	$K_{\text{Smag}}$ <sup>5</sup>	$UVJ$ <sup>6</sup>	$\log(M_*)$ <sup>7</sup>	$\log(L_{\text{UV}})$ <sup>8</sup>	$\log(L_{\text{IR}})$ <sup>9</sup>	$\log(L_{\lambda})$ <sup>10</sup>	$\log(L_{1.4\text{GHz}})$ <sup>11</sup>	IR-AGN <sup>12</sup>	X-AGN <sup>13</sup>	Rad-AGN <sup>14</sup>
UDS_21560	34.2495422	-5.1060505	0.81	18.76	1	11.2	2.38E+09	1.78E+10	-99	4.83E+23	0	-1	1
UDS_21602	34.3309555	-5.0983777	0.66	20.44	3	10.07	7.04E+08	1.16E+11	-99	-99	1	-1	-1
UDS_21607	34.2988777	-5.1105523	1.34	21.77	3	10.41	1.51E+09	2.42E+10	-99	-99	1	-1	-1
UDS_21742	34.2731819	-5.1081228	1.38	20.63	2	10.39	2.58E+10	2.20E+11	2.16E+45	-99	1	1	-1

**Table A.2** Column 1: source ID number. Columns 2 and 3: J2000 RA and declination of the  $Ks$ -band selected hosts, respectively. Column 4: photometric redshift. Column 5:  $Ks$ -band magnitude (AB). Column 6:  $UVJ$  criteria, where quiescent = 1, star-forming = 2 and dusty star-forming = 3. Column 7: host stellar mass ( $M_{\odot}$ ). Column 8: integrated 1216–3000Å rest-frame UV luminosity ( $L_{\odot}$ ). Column 9: integrated 8 – 1000μm rest-frame IR luminosity ( $L_{\odot}$ ). Column 10: 0.5–8 keV rest-frame luminosity (erg s<sup>-1</sup>). Column 11: 1.4GHz rest-frame luminosity (W Hz<sup>-1</sup>). Columns 12–14: IR, X-ray and radio AGN flags, respectively, where AGN = 1, else = 0.